

Intermittent Complexity Fluctuations
during
Ventricular Fibrillation

Dissertation

zur Erlangung des mathematisch-naturwissenschaftlichen Doktorgrades

“Doctor rerum naturalium”

der Georg-August-Universität Göttingen

im Promotionsprogramm ProPhys

der Georg-August University School of Science (GAUSS)

vorgelegt von

Alexander Schlemmer

aus Marburg

Göttingen, 2017

Betreuungsausschuss

Prof. Dr. Florentin Wörgötter, Drittes Physikalisches Institut,
Georg-August-Universität Göttingen

Prof. Dr. Ulrich Parlitz, Institut für Nichtlineare Dynamik,
Georg-August-Universität Göttingen

Prof. Dr. Stefan Luther, Institut für Nichtlineare Dynamik,
Georg-August-Universität Göttingen

Mitglieder der Prüfungskommission

Referent: Prof. Dr. Ulrich Parlitz, Institut für Nichtlineare Dynamik,
Georg-August-Universität Göttingen

Korreferent: Prof. Dr. Florentin Wörgötter, Drittes Physikalisches
Institut, Georg-August-Universität Göttingen

Weitere Mitglieder der Prüfungskommission:

Prof. Dr. Jens Frahm, Biomedizinische NMR Forschungs GmbH,
Max-Planck-Institut für Biophysikalische Chemie

Prof. Dr. Stefan Klumpp, Institut für Nichtlineare Dynamik,
Georg-August-Universität Göttingen

Prof. Dr. Stefan Luther, Institut für Nichtlineare Dynamik,
Georg-August-Universität Göttingen

Prof. Dr. Martin Uecker, Institut für Diagnostische und Interventionelle
Radiologie, Universitätsmedizin Göttingen

Tag der mündlichen Prüfung: 16.03.2017

Contents

1. Introduction	7
1.1. The Heart	8
1.1.1. Electrical Conduction System	9
1.1.2. Blood Transport	10
1.2. Electrocardiogram	10
1.3. Cardiac Arrhythmia	12
1.3.1. Treatment	14
1.4. Excitable Media	16
1.4.1. Models for Excitable Media	16
1.4.2. Fenton-Karma Model	17
1.5. Fluctuations in VF	17
1.6. Research Questions of the Thesis	19
1.7. Structure of the Thesis	19
2. Methods	21
2.1. Methods for Quantifying Complexity Fluctuations in the ECG	21
2.1.1. Permutation Entropy	21
2.1.2. PCA Entropy	23
2.1.3. Windowed Standard Deviation	25
2.1.4. Power Spectral Entropy	25
2.1.5. Wavelet Entropy and Wavelet Energy	26
2.2. Methods for Quantifying the Spatiotemporal Complexity	29
2.2.1. Phase Synchronisation Index	29
2.2.2. Analysis of Phase Singularities	30
2.2.3. Multi-Dimensional Permutation Entropy	31
2.3. ECG Definitions for Numerical Simulations	35
2.4. Statistical Definitions	36
2.4.1. Correlation Coefficient	36
2.4.2. Weighted Mean and Standard Deviation	36
2.4.3. Cohen's h	37
2.5. Data Preprocessing	37
2.6. Machine Learning Methods	38
2.6.1. Decision Trees and Random Forests	39
2.6.2. Cross Validation	41
2.6.3. Quantification of Classification Results	41

2.6.4.	Feature Importances	42
3.	Results	43
3.1.	Complexity Fluctuations in the ECG	43
3.1.1.	Summary and Conclusions	48
3.2.	Experimental Investigation of Complexity-Triggered Interventions	50
3.2.1.	Experimental Results	54
3.2.2.	Energy Reductions	61
3.2.3.	Summary and Conclusions	63
3.3.	Quantification of Complexity Fluctuations in the ECG	65
3.3.1.	Permutation Entropy	65
3.3.2.	PCA Entropy	68
3.3.3.	Wavelets	69
3.3.4.	Comparison of Complexity Measures for the ECG	71
3.3.5.	Machine Learning Analysis	75
3.3.6.	Descriptive Statistics for Complexity Fluctuations	78
3.3.7.	Algorithm for Detection of Laminar Phases	79
3.3.8.	Summary and Conclusions	85
3.4.	Quantification of Spatiotemporal Complexity	88
3.4.1.	Entropy Camera Experiments	88
3.4.2.	Results	90
3.4.3.	Analysis of Surface Camera Data	93
3.4.4.	Summary and Conclusions	100
3.5.	Angular Dependency of Complexity Fluctuations	103
3.5.1.	Results from 3D Simulations	104
3.5.2.	Surrogate Analysis of Correlations	110
3.5.3.	Analysis of Surface Camera Data	111
3.5.4.	Estimation of ECG channels needed for reliable ECG complexity detection	117
3.5.5.	Multielectrode Recordings obtained in Inverse ECG experiments .	121
3.5.6.	Summary and Conclusion	127
4.	Discussion and Outlook	129
4.1.	Summary	129
4.2.	Discussion and Outlook	131
5.	Bibliography	133
6.	List of Figures	143
7.	List of Tables	147
A.	Appendix	149
A.1.	Energy Reductions in Rabbit Ex Vivo Experiments	149
A.2.	Distribution of PE Values in Experimental Data	150

A.3. Complexity for Artificial Signals	150
A.4. Window Length	154
A.5. Development of Analysis Software	156
A.5.1. List of contributions	160
A.6. Preparation of the Animal Hearts	161
A.7. List of Experimenters	161
A.8. Data from Physionet	161
A.9. Simulation Data	164
A.10. Software	167
A.11. Acknowledgement	168

1. Introduction

The heart is a muscular organ driving the cardiovascular system of humans and many other species. Although it is known to restlessly maintain its functionality for long time spans, arrhythmias can result in severe problems for the organism and are one of the main causes of death for humans in Europe¹ and many other parts of the world.

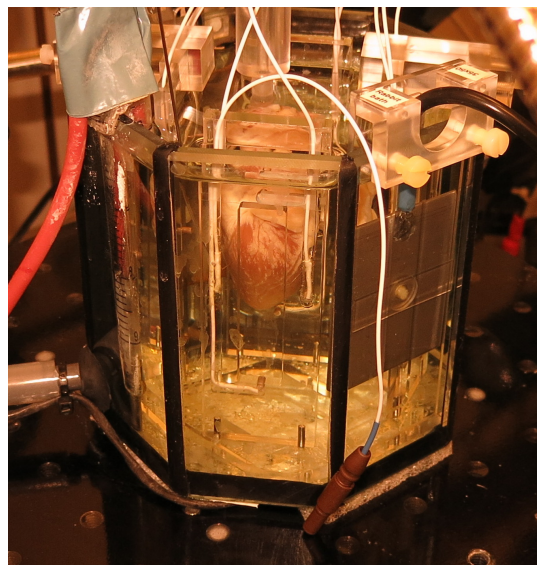


Figure 1.1.: Photo of the bath which is used in the perfusion experiments described in this thesis with a rabbit heart. See Sec. 3.2 and App. A.6 for detailed descriptions.

One important life-threatening arrhythmia is ventricular fibrillation (VF). This disease leads to a highly inefficient circulation of blood and therefore to a lack of oxygen supply for all organs. Without treatment, VF leads to death after minutes [32]. From the perspective of spatiotemporal dynamics many arrhythmias are associated with the emergence of reentrant electrical activity [32]. The normal pumping function is driven by periodic electrical activity on the heart muscle which is synchronized by special pacemakers. Reentrant activity results in a self-sustained excitation of the heart at a much

¹According to eurostat 12.6% of the total causes of death in 2014 belonged to the category of ischemic heart diseases (ICD-10 I20-I25), <http://ec.europa.eu>.

1. Introduction

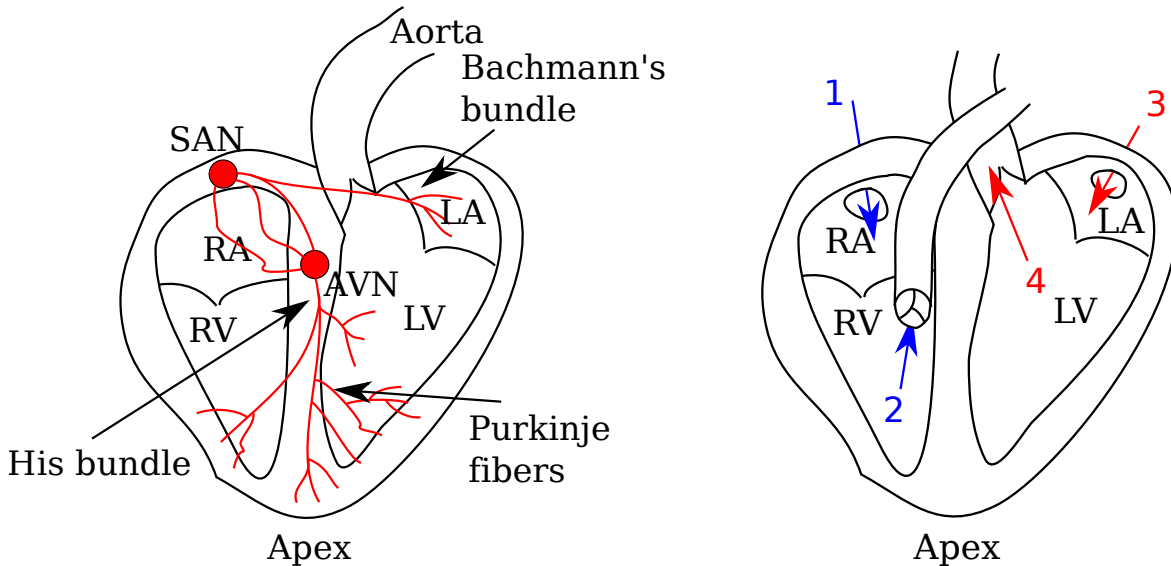
higher frequency than in the healthy state and the synchronization due to the pacemaker is no longer possible. In the theory of excitable media this reentrant electrical activity is described by rotating excitation waves. Although a single rotor, which can also be described as a scroll-wave [51, 101], causes a relatively simple type of periodic activity, its possible movement and interaction with boundaries, heterogeneities, and other rotors can cause many dynamical scenarios of varying complexity.

The starting point of this thesis is the observation that during VF different levels of complexity can be seen in the electrocardiogram (ECG) time series. As these variations in complexity originate from the spatiotemporal dynamics on the heart muscle itself, it can be hypothesised that information about the electrical state of the heart is still contained in this low-dimensional representation given by the ECG. The ECG is widely used for diagnostics and therapy and also part of many implantable defibrillation devices. If enough information about the underlying dynamical state of heart is contained in the ECG it can possibly be used for optimizing the process of recovering a heart during VF. This would also require the existence of dynamical states of different complexities that show differences during treatment regarding success probability and side effects. This assumption seems very reasonable as differences in success probabilities have been reported for a long time [52] for different patterns in the ECG.

The following Sec. 1.1 describes the heart and its functionality, before the ECG as one of the main signals to monitor its state is discussed in Sec. 1.2. Cardiac arrhythmias and especially ventricular fibrillation will be discussed thereafter including methods for their treatment in Sec. 1.3. Afterwards in Sec. 1.4 the problem is described from the physical perspective using the theory of excitable media. Sec. 1.5 discusses literature on the topic of fluctuations during VF and their previous applications in treatment and diagnosis before the main research questions for this thesis are formulated in Sec. 1.6. An overview over the whole thesis can be found in the final Sec. 1.7 of the introduction.

1.1. The Heart

The heart is composed of four chambers. Two of them, which are called atria, collect the blood in a preliminary stage before pumping it into the two main chambers which are called ventricles (see Fig. 1.2). The whole human blood circuit can be divided into two branches: One is connecting the outflow of the right ventricle to the lungs and the output of the lungs to the left atrium. This part of the circuit is responsible for oxygenating the blood in the lungs. The left ventricle pumps the oxygenated blood via the aorta into the body. The deoxygenated blood from the organs is transported back into the heart via the right atrium.



(a) Sketch of the electrical conduction system of the heart described in Sec. 1.1.1. SAN: Sinoatrial Node, AVN: Atrioventricular Node

(b) Sketch of the blood transport. See text in Sec. 1.1.2 for description of labels 1-4.

Figure 1.2.: Sketches of the heart illustrating important elements of the pacemaking, conduction and blood transport processes. RV: Right Ventricle, LV: Left Ventricle, RA: Right Atrium, LA: Left Atrium

1.1.1. Electrical Conduction System

In order to execute the pumping process efficiently the heart has to contract in a synchronized fashion. It undergoes multiple stages of contraction during each cardiac cycle. This is enabled by a special sequence of propagation of the electrical signals which trigger the contraction of the heart. Initially the electrical signal of the healthy heart is generated in the main pacemaker that is called the sinoatrial node (SA node) and located in the wall of the right atrium (SAN in Fig. 1.2a). The SA node generates a periodic signal between approximately 60 to 100 beats per minute (bpm). The heart is innervated by parasympathetic and sympathetic nerves which can influence the heart rate to enable the organism to react to environmental influences. The electrical activity propagates over the atria and makes them contract leading to a pumping of blood into the ventricles. The signal is not passed on directly to the ventricles afterwards, but is delayed in the atrioventricular node (AV node, AVN in Fig. 1.2a). The AV node itself can act as an independent pacemaker at a lower frequency than the SA node. Therefore, it can temporarily take over in case of an impaired SA node or uncontrolled activity on the atria.

From the AV node the signal is transmitted via the His-bundle and the Purkinje fibers

1. Introduction

to the ventricles where the contraction begins at the apex. This sequence of activations of different parts of the heart produces a very distinct type of electrical pattern which can be made visible using an ECG which is explained in Sec. 1.2. Deviations from this sequence of patterns can lead to cardiac arrhythmias which are discussed in Sec. 1.3.

1.1.2. Blood Transport

The deoxygenated blood enters the heart through the superior vena cava (denoted by 1 in Fig. 1.2b) and the inferior vena cava and is collected in the right atrium. During the atrial systole the atria contract which pumps the blood from the right atrium through the tricuspid valve into the right ventricle. During the ventricular systole which follows shortly afterwards the blood is pumped through the pulmonary valve into the pulmonary artery (sketched by 2 in Fig. 1.2b) which leads to the lungs.

Simultaneously during the same cardiac cycle oxygenated blood coming from the lung enters the left atrium through the pulmonary vein (3 in Fig. 1.2b) and is pumped during the atrial systole and through the mitral valve into the left ventricle. During the ventricular systole this blood is pumped through the aortic valve into the aorta which conducts the blood into the whole body.

While the contractions of atria and ventricles are called systoles, the respective relaxations are called atrial diastole and ventricular diastole.

1.2. Electrocardiogram

The ECG is one of the most prevalent measurement techniques for monitoring the condition of the human heart. As the mechanical contraction is triggered by electrical signals in the heart tissue, it can be directly related to specific phases during a cardiac cycle. By using electrodes that are usually attached to the surface of the human body potential differences can be measured. The methodology has been discovered at the end of the nineteenth century by Augustus Waller who recorded the first human ECG in 1887 [14]. His work and measurement techniques were improved significantly by Willem Einthoven at the beginning of the twentieth century who also developed the first clinical applications [14].

The ECG measures the potential difference between the ECG electrodes which are placed to cover the parts of the heart which are under investigation. Several standard electrode configurations exist, for example the three-lead configuration and the twelve-lead setup. The latter is very prevalent in the clinical context as it allows for a fine-grained detection

of specific heart-diseases while the former already provides a way to measure the normal shape of the sinus rhythm and important features, like frequency or heart-rate variability [61] reliably.

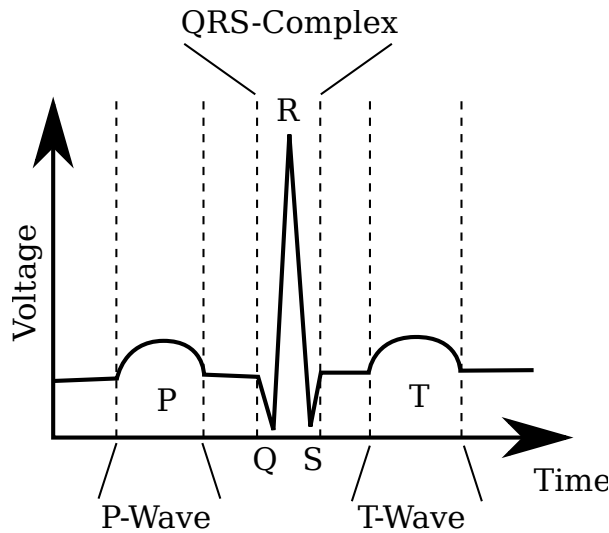


Figure 1.3.: Sketch of the shape of a healthy QRS complex.

The well-known shape of the healthy ECG signal is sketched in Fig. 1.3. The three most important features of the healthy ECG are the P-wave, the QRS-complex and the T-wave which are directly related to specific phases during the process of contraction of the heart [32]. The contraction of the tissue is initiated by cell depolarization which can be recorded by the ECG. The P-wave is the result of the depolarization of the atria which leads to a small bump in the ECG. The QRS-complex corresponds to the contraction of the ventricles. The first negative peak (Q) is the result of the electrical signal travelling from the apex to the base. Afterwards the full depolarization of the ventricles leads to the very high peak marked with the letter R. The T-wave which follows the QRS-complex belongs to the repolarization phase of the cycle. Another pattern which sometimes can be seen is the U-wave which would follow the T-wave and is the result of the repolarization of the His-Purkinje system. There is, however, still a discussion about its origin, especially in the case of larger U-wave amplitudes [40]. The two time intervals separating the P-wave from the QRS-complex and the QRS-complex from the T-wave are called PQ-segment and ST-segment. The specific properties of the waves and segments described here are clinically very important, because they can reveal many details about the proper or improper functioning of the heart. These properties and their possible implications are therefore well described in the medical literature ([40] for example) and constitute an important part of medical diagnoses.

The ECG can be modelled using dipole moments [45] which affect the potential differences measured by the ECG electrodes on the surface of the body (or in the bath, as it is the case in *ex vivo* experiments).

1. Introduction

A single electrical dipole with charge q and distance \vec{d} has the electrical dipole moment

$$\vec{p} = q \cdot \vec{d} \quad (1.1)$$

which causes a dipole potential at location \vec{r} (long distances from the center of the dipole and $|\vec{r}| \gg |\vec{d}|$)

$$u(\vec{r}) = \frac{1}{4\pi\epsilon_0} \cdot \frac{\vec{p} \cdot \vec{r}}{|\vec{r}|^3} \quad (1.2)$$

with the dielectric constant ϵ_0 .

When measuring potential differences between points \vec{r}_1 and \vec{r}_2 this leads to

$$U(\vec{r}_1, \vec{r}_2) = u(\vec{r}_2) - u(\vec{r}_1) \quad (1.3)$$

$$= \frac{1}{4\pi\epsilon_0} \cdot \frac{\vec{p} \cdot (\vec{r}_2 - \vec{r}_1)}{r^3} \quad (1.4)$$

if $r = |\vec{r}_1| = |\vec{r}_2|$ (both electrodes have the same distance to the dipole).

The complete ECG which is composed of many dipole moments is usually modelled by calculating sums or integrals over many dipole moments [73]. This formalism is used to calculate realistic ECGs in simulations which is described in Sec. 2.3.

Although the the twelve-lead ECG setup is used prevalently for clinical diagnosis, many experimental setups make use of single electrode pairs for measuring the ECG. Implantable cardioverter defibrillators (ICD) usually also only comprise a single ECG channel.

1.3. Cardiac Arrhythmia

There are many reasons which can cause the normal and healthy sinus rhythm to degenerate into lethal cardiac arrhythmias [32]. One type of arrhythmia which is called tachycardia manifests itself in a much higher frequency than the healthy sinus rhythm: While the healthy resting heart rate of an adult human is usually between 60 and 90 beats per minute (bpm) the resting heart rate during ventricular tachycardia (VT) is

defined² to be larger than 100 bpm. It is usually associated with a single scroll wave (see Sec. 1.4) or stable periodic reentrant electrical activity on the heart muscle [86].

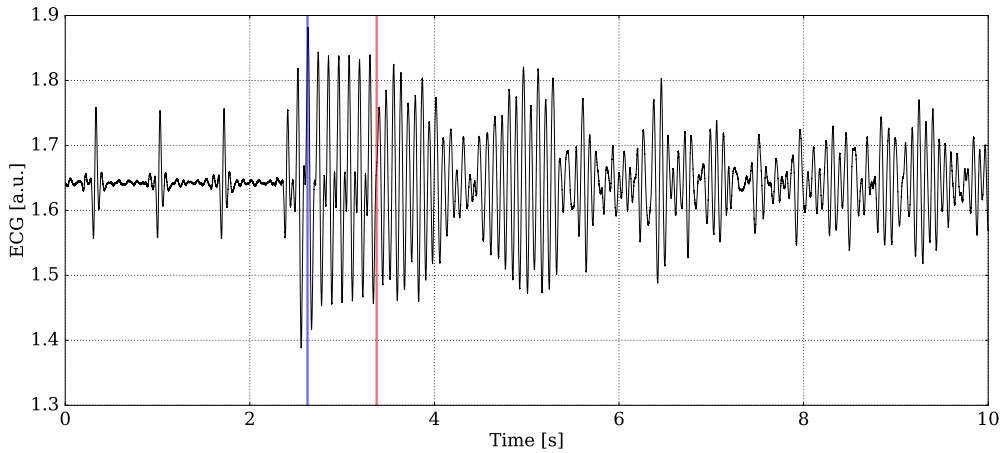


Figure 1.4.: ECG time series from an ex vivo experiment with a rabbit heart showing the transition of a sinus rhythm to VT and VF. The blue line marks the onset of ventricular tachycardia (VT) with an approximate frequency of 8.75 Hz. The red line marks the begin of the deterioration into ventricular fibrillation (VF) at a dominant frequency of 12.5 Hz. This ECG has been recorded on 2017-02-01 by Sebastian Berg and Edda Boccia.

An even more dangerous form of arrhythmia is called fibrillation. This type of arrhythmia is associated with very high frequencies² of 300 to 800 bpm. As the electrical signal transmission has to pass and is delayed at the AV node, a fibrillation can be sustained in the atria or the ventricles only. The former type is called atrial fibrillation (AF) while the latter type is called ventricular fibrillation (VF). Fibrillation is associated with highly unsynchronized activity on the heart muscle and is in many cases initiated by a VT. An example ECG time series for such a transition is shown in Fig. 1.4. The onset of VF is usually associated with wave-breakup of a single rotor [32] which leads to many coexisting rotors following complex behaviour (see Sec. 1.3.1 and Sec. 2.2.2). During AF it is in many cases still possible to maintain the sinus rhythm, because the AV node is able to act as a backup pacemaker, however in a less efficient way. VF is immediately life-threatening as the heart contracts in a completely desynchronized fashion and is not able to keep up its pump functionality. When untreated this form of arrhythmia leads to death within minutes [32].

²The frequency definitions given in this section are valid for humans. They are dependent on the species.

1.3.1. Treatment

The conventional treatment of VF is the application of a high energy shock of around 120 to 300 Joules³ [38] to the heart which is known as defibrillation. This shock leads to an immediate electrical activation of the whole tissue. After repolarization of the muscle cells the normal pacemaker (the SA node under normal conditions) can reenact the sinus rhythm. The high amount of energy used in the conventional defibrillation involves several issues:

- The application of the shock can be extremely painful for the patient. This is even more serious in the case of implantable cardioverter-defibrillators (ICD). While external defibrillators are used in case of emergency on a person that probably already has become unconscious due to the arrhythmia, ICDs are implanted into risk patients and apply high energy shocks upon the detection of a life-threatening arrhythmia. The automatic detection of the latter by the device does not have a false positive rate of zero and therefore misdetections and the application of shocks to conscious persons are possible.
- The current delivered to the organ during the shock can destroy or injure tissue [6, 99]. This might potentially increase the risk of future arrhythmias.
- The energy required for the shock influences the form of implantable devices, because batteries of the appropriate size are required. Smaller devices are easier to implant, more convenient for the wearer and can operate for longer periods.

The need for defibrillation techniques requiring less energy has motivated several alternative protocols including [59] and [29].

The main idea behind the low energy defibrillation approach (called LEAP, low-energy antifibrillation pacing) described in [59] uses the concept of virtual electrodes [36] which are recruited during the application of a series of low energy pulses. The virtual electrodes themselves are regions inside the heart muscle which are not excitable or heterogeneous in conductivity. Examples include blood vessels or defect muscle tissue. Upon the exposure to an electric field, these virtual electrodes are depolarized and lead to the emission of excitation waves. This local emission of excitation waves at many locations within the heart leads to a synchronization of the electrical activity of the whole tissue. As the electric field strength required to recruit a virtual electrode is inversely related⁴ to its radius [59, 76], a higher number of virtual electrodes is activated for higher energies (details about these relations are given in [59] and [47]).

³These values refer to external defibrillators, for implantable cardioverter-defibrillators it is around 30 Joules.

⁴It is approximately antiproportional for small heterogeneities.

The dynamics during ventricular fibrillation is known to be driven by rotating and interacting scroll waves [68, 101]. The usual understanding is that ventricular tachycardia (VT) is driven by a single rotor causing regular contraction at a higher frequency than sinus rhythm. This rotor can be very stable and lead to ventricular tachycardias that last for longer time spans. Breakup of this rotor, however, causes the simultaneous existence of multiple interacting rotors. The phase filaments which form the rotation centers of the scroll waves can move along complex trajectories and their interaction can cause changes in size, shape and number [26]. Measuring and visualizing scroll waves in real hearts is still very difficult, although a lot of progress has been made recently [25].

The mechanisms of termination of the unordered activity during fibrillation are not completely understood. However, multiple possible mechanisms regarding the interaction of control strategies with spiral waves and scroll waves have been studied in detail. In addition to the investigation of real cardiac dynamics often simulation results or other experimental systems for excitable media (see Sec. 1.4) were used.

One important control mechanism for spiral waves in excitable media is to periodically excite the system close to the spiral wave in order to produce excitation waves. If this pacing has a frequency f_p higher than the frequency of the spiral f_s , a drift is induced and the spiral wave is pushed away [78, 55]. Making the spiral drift into a boundary leads to its termination. A frequency ratio $\frac{f_p}{f_s} > 1$ is usually called overdrive pacing. The technique of terminating arrhythmias, called antitachycardia pacing (ATP), with pulse trains using overdrive pacing is integrated in implantable cardioverter defibrillators (ICDs) and can terminate some VTs without causing pain to the patient [100].

Many studies address the problem of pinned spirals. This type of reentrant activity denotes spiral waves which are rotating around a heterogeneity and has to be unpinned from the heterogeneity before it can be terminated using a far-field electric shock [77, 17].

Some evidence exists that in the case of pinned spiral waves a pacing-strategy with a frequency ratio of $\frac{f_p}{f_s} < 1$ (underdrive pacing) works better than overdrive pacing [15, 47]. For VT it has also been shown that pinned spirals can be unpinned and terminated more efficiently when the shocks are given into specific phase intervals of the VT cycle [86, 57].

In addition to the frequency, the shape of the pulses applied during the pacing strategy can also play a major role. One of the important recent development in commercial cardiac defibrillators was the change from monophasic to biphasic pulses [66, 93] which resulted in approximately 30% reduction of required energy [11]. A biphasic pulse is a combination of two monophasic pulses with opposite polarity.

1.4. Excitable Media

The abstract formalism for analysing propagation and pattern formation of electrical activity on cardiac tissue is the theory of excitable media [105, 64]. An excitable medium is defined by the following properties which can either be expressed in a continuous fashion or by discrete elements which form the medium:

- **Excitability:** The system point or cell can be in a resting state or excited above an excitation threshold which separates the resting state from the excited state.
- **After excitation** the system point or cell is in the refractory state in which it is not excitable. The period until the system is excitable again is called refractory period.
- **Propagation:** Excitation in one system point or cell leads to an excitation of neighbouring elements which allows propagation of excitation waves.

These principles can be found in many different systems [95], for example chemical reactions [103, 22, 64], or colonies of amoeba called *Dictyostelium* [79]. One very typical pattern for excitable media is the emergence of spiral waves in two-dimensional systems or three-dimensional scroll waves [22] in three-dimensional systems. Phase singularities and phase filaments, which are mathematical descriptions of the centers of rotation, are discussed in Sec. 2.2.2. Similar properties hold for the cardiac action potential.

1.4.1. Models for Excitable Media

For numerical investigations of excitable media many different mathematical models exist. Different types of models include:

- **Cellular automata:** This type of model provides a straight forward and computationally simple approach for simulating a system of connected cells having a quiescent, an excited and at least one refractory state. Excitation and propagation is modelled by rules that specify how many excited neighbouring cells are needed for the excitation of a specific cell. Although this computationally very inexpensive type of model is able to produce some important features of excitable media like spiral waves, it is usually not able to show realistic patterns. One example is the Greenberg-Hastings model [37].
- **Ionic models:** This type of model tries to completely model cardiac cells on an ionic level by providing differential equations for each single type of ionic channel responsible for generating the action potential. This type of model is extremely

computationally expensive and usually the fixation of realistic parameter sets is a challenge. Prominent examples are the Beeler-Reuter model [34] and the Luo-Rudy model [58].

Many low dimensional simplifications of ionic models exist which can be seen as a compromise between these two extremes. This will always include a tradeoff between more realistic and more generic behaviour, so a model which is suitable for the investigated problem has to be selected. A notable model which is simple and not computationally demanding is the Barkley model [13, 12] which has been used in many simulations for cardiac dynamics. An overview over many models for cardiac cells can be found in [34].

1.4.2. Fenton-Karma Model

For investigating phenomena related to electrical wave propagation on the ventricle, the Fenton-Karma model [33] is a reasonable choice. It is a three-variable model of reaction-diffusion type:

$$\dot{V}_m = \nabla \cdot \mathbf{D} \nabla V_m - I_{\text{ion}}(V_m, v, w) / C_m \quad (1.5)$$

with the diffusion tensor \mathbf{D} , the local membrane voltage V_m , a local ion current I_{ion} and membrane capacitance C_m . The total local ion current I_{ion} depends on the membrane voltage and two gating variables v and w . It is the negative sum of a fast inward current (J_{fi}), a slow outward current (J_{so}) and a slow inward current (J_{si}) [34]. These model the total contributions from the sodium, potassium and calcium channels which generate the cardiac action potential.

$$I_{\text{ion}}(V_m, v, w) = -(J_{\text{fi}}(V_m, v) + J_{\text{so}}(V_m) + J_{\text{si}}(V_m, w))$$

The equations of the Fenton-Karma model and details about the simulations are given in the Appendix in Sec. A.9.

1.5. Fluctuations in VF

The observation of qualitatively different types of VF has already been described in early medical literature about VF morphology in the ECG. The most prevalent and earliest classification of VF types is into ‘‘coarse VF’’ and ‘‘fine VF’’. In Ref. [98] from 1969 it is already described that there seems to be an inverse relation between coarseness of the VF waveform and the required defibrillation energy. Coarse VF itself is defined as ECGs having an amplitude larger than 0.2 mV [84].

1. Introduction

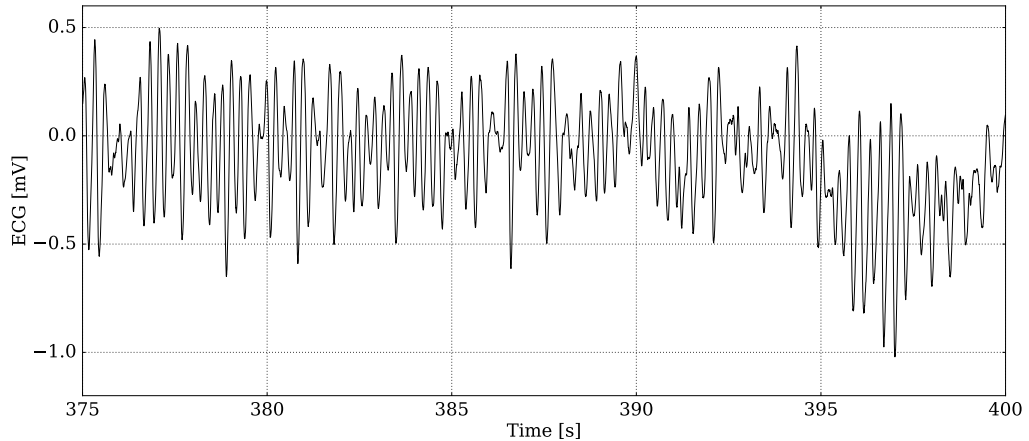


Figure 1.5.: Example for a VF time series from a human heart taken from Physionet Sudden Cardiac Death Holter Database [41, 39]. The ECG starts approximately 375 s after the onset of the VF and is the first ECG channel in the data file of subject no. 31.

These observations led to experimental investigation of the cause of coarse and fine VF by Jones et. al. [52] who studied synchronisation of the tissue by measuring standard deviations of activation times. In this aspect they found no difference between coarse and fine VF and concluded that coarseness is the sole effect on limb lead orientation at the beginning of a VF, while in a later time period the deterioration of the cell excitabilities leads to fine VF. However, a patent from 2000 [53] describes a device for specifically defibrillating into the up-slope of a coarse VF.

Another study suggesting that coarse VF is easier to defibrillate was published by Kuelz et. al. in 1994 [56] who used the absolute VF voltage integrated over different window lengths as a measure for coarseness and found that higher values thereof lead to a higher defibrillation success rate.

Many works cover the analysis of the VF waveform using different measures [84, 62, 3] and their utilisation in predictions. Recent approaches include wavelet analysis [3], delay reconstruction based methods [94] and approximate entropy [65, 46, 42, 102]. In [24] a recent overview over entropy based measures and their predictive capabilities is given and many other complexity measures are compared in [65].

Although the analysis of ECG time series provides promising techniques for classification and prediction of defibrillation success and required energy, it is desirable to investigate the mechanisms leading to complexity fluctuations during VF. This is especially important in the context of novel low energy defibrillation techniques which rely on specific mechanisms, such as unpinning of and the interaction with spiral waves. As it can generally be assumed that more complex spatiotemporal dynamics on the heart hin-

der an efficient termination of VF [72] it is conjectured that LEAP and possibly other low energy VF termination strategies would strongly benefit from an identification of intermittent states of simpler spatiotemporal structure.

Fig. 1.5 shows an example for a human ECG which contains complexity fluctuations.

1.6. Research Questions of the Thesis

The focus of this thesis is the optimization of LEAP by exploiting complexity fluctuations during VF.

This implies the following research questions:

- How can intermittent complexity fluctuations be quantified in a fast and reliable way?
- How do these complexity fluctuations relate to the underlying spatiotemporal dynamics of the heart during VF?
- Does triggering the defibrillation pulses during periods of intermittent regularity (laminar phases) improve the defibrillation success?

For convenience the term “laminar phase” will be used synonymous with “less complex phase in the ECG”. This term has been borrowed from the theory of turbulent flows and is not meant as an accurate description of the underlying process, but intended to describe the regular nature of these periods.

1.7. Structure of the Thesis

The main part of the thesis is split into two chapters. The methods Chapter 2 will present the theoretical background and mathematical descriptions of the methods used. The result Chapter 3 consists of five sections which analyse different aspects of the phenomenon of complexity fluctuations in the ECG:

- Sec. 3.1 treats the detection and description of complexity fluctuations in VF in the ECG using permutation entropy.
- Sec. 3.2 discusses a series of ex vivo experiments for investigating complexity trig-

1. Introduction

gered defibrillation.

- Sec. 3.3 provides comprehensive investigation of properties of the ECG time series during VF:
 - Sec. 3.3.1, Sec. 3.3.2 and Sec. 3.3.4 discuss multiple measures from time series analysis and nonlinear dynamics for quantifying the complexity fluctuations and their interrelation.
 - Sec. 3.3.5 applies random forests to features extracted from time series excerpts before the shock in order to predict the shock outcome.
 - In Sec. 3.3.6 statistical properties of low complexity phases are analysed.
 - Sec. 3.3.7 presents an algorithm for the efficient detection of low complexity phases.
- Sec. 3.4 analyses spatiotemporal dynamics underlying complexity fluctuations in ex vivo experiments.
- Using data from numerical simulations the dependency between ECG signals and the spatiotemporal dynamics is analysed in Sec. 3.5.

The main results and conclusions are summarized at the end of each section.

2. Methods

2.1. Methods for Quantifying Complexity Fluctuations in the ECG

This section introduces different types of complexity measures which will be used for quantifying the time-dependent variations in the ECG.

2.1.1. Permutation Entropy

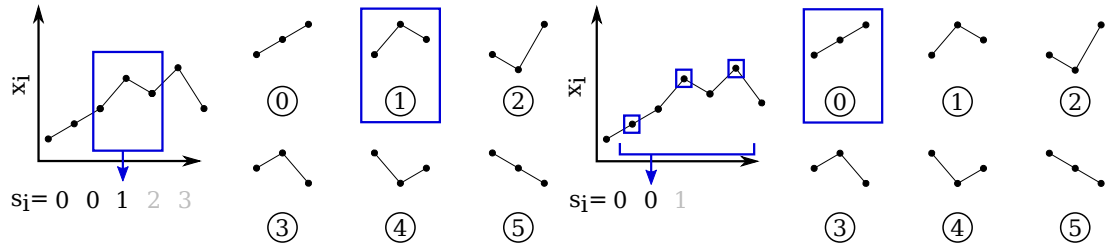
The permutation entropy (PE) is a quantity that characterizes the distribution of order patterns. Order patterns, sometimes also called ordinal patterns emerge as the result of transforming subsequent values of a time series into symbols which solely depend on the relative ordering of its elements. This process is sketched in Fig. 2.1 and described in detail below. One of the first publications describing order patterns is [10]. A more detailed description is provided by [5]. An application to cardiac time series is published in [69].

Starting from a time series x_1, x_2, \dots, x_N of length N , words w_i of length D are extracted to make up a new series. To be able to cope with different time scales, instead of just taking successive values, the components of each word can be separated by a time delay L :

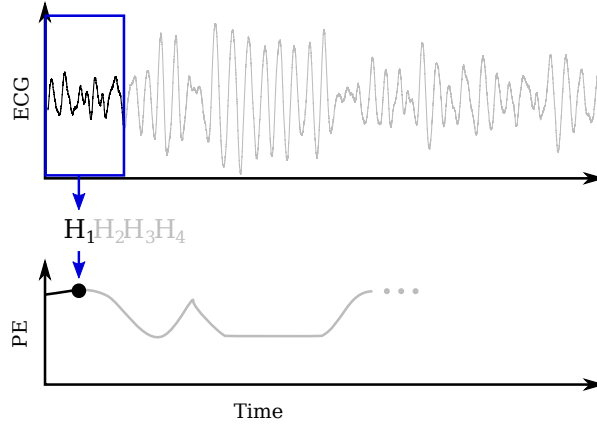
$$\tilde{w}_i = x_i, x_{i+L}, x_{i+2L}, \dots, x_{i+(D-1)L} = w_{i,1}, w_{i,2}, \dots, w_{i,D} \quad (2.1)$$

To quantify the ordinal pattern, each word is assigned the permutation index, which uniquely specifies the relative ordering of the $w_{i,j}$ within each \tilde{w}_i . The permutation

2. Methods



(a) Calculation of the permutation index with length $D = 3$ and time delay $L = 1$. (b) Calculation of the permutation index with length $D = 3$ and time delay $L = 2$.



(c) Sketch visualizing the computation of the windowed PE from of a VF time series. The blue rectangle marks the time window from which the corresponding value of the PE is computed.

Figure 2.1.: Visualization of the process of computing the windowed PE out of a time series.

index s_i is calculated according to

$$s_i = \sum_{j=1}^{D-1} (D-j)! \lambda_j \quad (2.2)$$

$$\lambda_j = \sum_{k=j+1}^D \begin{cases} 1 & \text{if } w_{i,j} < w_{i,k} \\ 0 & \text{else} \end{cases} \quad (2.3)$$

Fig. 2.1a visualizes the extraction of words with $D = 3$ and $L = 1$ and the assignment of the permutation index. The effect of introducing a time delay $L > 1$ is visible in Fig. 2.1b. An overview over all possible patterns of length $D = 4$ is displayed in Fig. 2.2.

To quantify the distribution of symbols s_i within a time series the permutation entropy can be used. Each s_i can take values between zero and $D! - 1$. Let k_j be the number of symbols with value j where $0 \leq j \leq D! - 1$ and $p_j = k_j / (N - K + 1)$ their relative

frequencies where K is the extent of each word in the original time series $K = (D - 1)L + 1$. The permutation entropy is then computed using the formula for the Shannon entropy:

$$H = - \sum_{j=0}^{D!-1} p_j \cdot \log_2 p_j \quad (2.4)$$

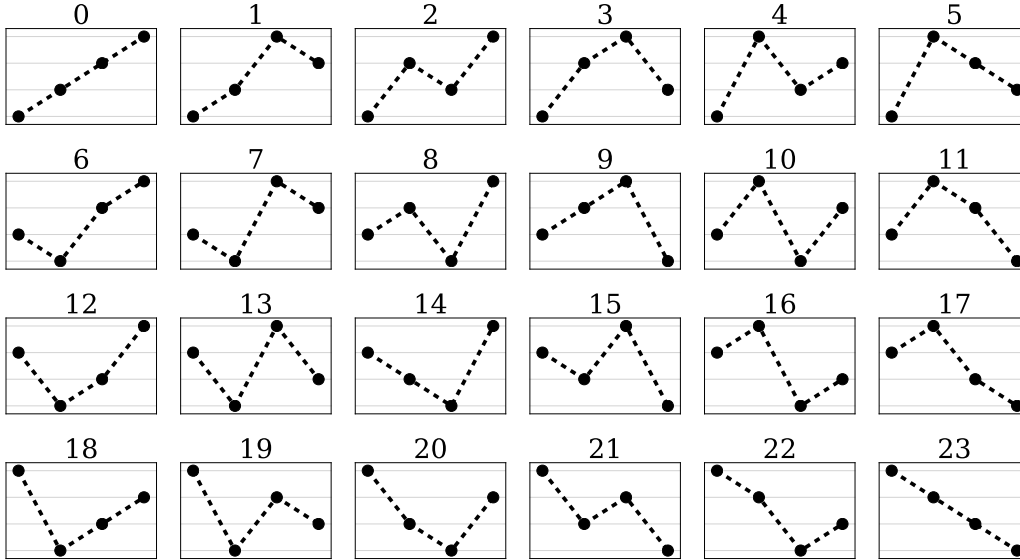


Figure 2.2.: An overview over all possible patterns for word length $D = 4$

This quantity will be used as a measure for the complexity of the ECG. In order to characterize its fluctuations over time a windowed version is used, which is computed from overlapping windows $N < \tilde{N}$ of the original ECG time series with length \tilde{N} . The windowed permutation entropy has three main parameters: The word length D , the time delay L and the window length N . The range of values for the word length D is quite restricted as with growing D the number of possible symbols grows with the factorial which soon leads to a bad estimation of relative frequencies p_j . The word length will therefore be fixed to $D = 4$ which seems to be a good compromise between the word length and the number of possible symbols.

2.1.2. PCA Entropy

Although the theory of permutation entropy [10] establishes the relation between this quantity and the delay embedding space of the time series, there are much more direct

2. Methods

ways to quantify the complexity of the time series in the delay embedding space. One method presented here is based on the Broomhead-King Coordinates [20] which is basically a principal component analysis (PCA) applied to delay coordinates. The BKC and H_{PCA} which are discussed in this section do not seem to be described in the literature yet.

The first step of this method consists of generating the trajectory matrix containing the delay embedded vectors from the original time series x_1, x_2, \dots, x_N of length N :

$$X = \frac{1}{\sqrt{N}} \begin{pmatrix} x_1 & x_2 & \cdots & x_D \\ x_2 & x_3 & \ddots & x_{D+1} \\ \vdots & & & \vdots \\ x_{N-D+1} & \cdots & & x_N \end{pmatrix} \quad (2.5)$$

with D being the embedding dimension.

This trajectory matrix can now be decomposed using the singular value decomposition (SVD) [75] into:

$$X = U \cdot S \cdot V^{\text{tr}} \quad (2.6)$$

with U being a unitary matrix, V being a unitary matrix and S being a diagonal matrix with (diagonal) elements $\sigma_1 \geq \sigma_2 \cdots \geq \sigma_r > 0$ which are called singular values.

The singular values computed from the trajectory matrix X represent the extent of the set of reconstructed states in the eigendirections of the reconstructed attractor. A complexity measure can therefore be calculated for the sum of the normalized singular values:

$$\text{BKC} = \sum_{i=1}^r \frac{\sigma_i}{\sigma_1} \quad (2.7)$$

In this thesis this quantity will be referred to as Broomhead-King-Complexity (BKC). The effect of the normalization is that in the case of equal extent of the set of reconstructed states into all eigendirections the BKC will equal the delay embedding dimension D . Otherwise it will be lower.

In Eq. 2.8 the trajectory matrix is written with time delay $L = 1$. Similar to the PE it can be desirable to be able to capture different time scales and therefore to introduce a time delay (sometimes also called lag) $L > 1$ which leads to the lagged trajectory matrix:

$$X = \frac{1}{\sqrt{N}} \begin{pmatrix} x_1 & x_{1+L} & \cdots & x_{1+(D-1)L} \\ x_2 & x_{2+L} & \ddots & x_{2+(D-1)L} \\ \vdots & & & \vdots \\ x_{N-(D-1)L} & \cdots & & x_N \end{pmatrix} \quad (2.8)$$

This procedure deviates from the standard Broomhead-King coordinates which simply uses $L = 1$ and is probably only relevant in cases where the embedding dimension can not be chosen large enough, because of computation time considerations.

While BKC measures the relative deviation from the maximum possible extent in all directions, another similar quantity can be introduced for Broomhead-King coordinates:

$$H_{\text{PCA}} = - \sum_{j=1}^r p_j \cdot \log_2 p_j \quad (2.9)$$

$$p_j = \frac{\sigma_j}{\sum_{i=1}^r \sigma_i} \quad (2.10)$$

H_{PCA} is the entropy over the normalized singular values and measures the deviation from all singular values being constant which would result in its maximum value $H_{\text{PCA}} = -\frac{1}{r} \cdot r \cdot \log_2 \left(\frac{1}{r}\right) = \log_2(r)$. In the H_{PCA} and BKC are highly correlated in practice. Therefore only H_{PCA} is used in the results chapter.

2.1.3. Windowed Standard Deviation

A very straight-forward method to quantify the amplitude fluctuations in the ECG is the windowed standard deviation. Starting from a time series x_1, x_2, \dots, x_N of length N successive segments of window length L are extracted. The sequence of windowed standard deviations is then computed as:

$$\text{STD}_i = \text{SD} (\{x_i, x_{i+1}, x_{i+2}, \dots, x_{i+L-1}\}) \quad (2.11)$$

$$= \sqrt{\frac{1}{L-1} \sum_{j=0}^{L-1} (x_{i+j} - \bar{x}_i)^2} \quad (2.12)$$

where \bar{x}_i is the average over the window with index i : $\bar{x}_i = \frac{1}{L} \sum_{j=0}^{L-1} x_{i+j}$

2.1.4. Power Spectral Entropy

The power spectral entropy (PSE) is a straight-forward method to quantify the distribution of different frequency components in a signal. Using the power spectrum

2. Methods

P which can be computed from the discrete Fourier transform $Y(f)$ of the signal as $P(f) \propto |Y(f)|^2$.

By normalizing the discrete components of $P(f)$ with the sum over all $P(f)$ relative frequencies p_i can be computed and inserted into the formula for the power spectral entropy:

$$\text{PSE} = - \sum_i^N p_i \cdot \log_2 p_i \quad (2.13)$$

when N is the number of frequency bins. The PSE is computed for a restricted frequency range from 0.5 Hz to 35 Hz in this thesis.

2.1.5. Wavelet Entropy and Wavelet Energy

The discrete wavelet transform (DWT) [75] is a method to very efficiently decompose a signal into its wavelet spectrum. Its implementation as a linear filter makes it suitable for real-time implementations into soft- or hardware. The decomposition procedure involves the repeated convolution of the wavelet filter matrix with the signal and intermediately filtered versions thereof. For a Daubechies wavelet of order four the general form of the filter matrix¹ is:

$$M_{\text{Wavelet}} = \begin{pmatrix} c_0 & c_1 & c_2 & c_3 & 0 & \dots & 0 \\ c_3 & -c_2 & c_1 & -c_0 & 0 & \dots & 0 \\ 0 & c_0 & c_1 & c_2 & c_3 & \dots & 0 \\ 0 & c_3 & -c_2 & c_1 & -c_0 & \dots & 0 \\ \vdots & \ddots & & & & \ddots & \vdots \\ 0 & \dots & 0 & c_0 & c_1 & c_2 & c_3 \\ 0 & \dots & 0 & c_3 & -c_2 & c_1 & -c_0 \\ c_2 & c_3 & & \dots & 0 & c_0 & c_1 \\ c_1 & -c_0 & & \dots & 0 & c_3 & -c_2 \end{pmatrix} \quad (2.14)$$

Each odd row of the matrix produces a smoothed version of the signal when applied to data. In contrast the even rows yield small values only for input data that is smooth. So one application of M_{Wavelet} to a data vector with length $N = 2^n, n \in \mathbb{N}, n \geq 2$ leads to a new data vector having smoothed components s_i of the original data in the odd rows and even components ϕ_i that reflect the fine contents of the input vector:

$$M_{\text{Wavelet}} \cdot (x_1, x_2, \dots, x_N)^T = (s_1, \phi_1, s_2, \phi_2, \dots, s_{N/2}, \phi_{N/2},)^T \quad (2.15)$$

¹Initially of size $N \times N$.

By reordering the output vector² into its smoothed components and fine components and successively applying M_{Wavelet} only to the smoothed components of the output vector, one arrives at the wavelet decomposition of the signal:

$$(w_1, w_2, \dots, w_N)^T = (s_1^k, s_2^k, \phi_1^k, \phi_2^k, \phi_1^{k-1}, \phi_2^{k-1}, \dots, \phi_1^1, \dots, \phi_{N/2}^1)^T \quad (2.16)$$

where s_i^j and ϕ_i^j are the smooth and fine components after decomposition step j and $k = (\log_2 N) - 1$ being the maximum number of possible decompositions. Decomposition steps will be referred to as scales here with the first decomposition step being the finest scale and the last decomposition step being the largest scale. Input signals with $N \neq 2^n \forall n \in \mathbb{N}$ are usually padded³ to the next power of 2.

The wavelet coefficients c_i are determined by requiring the matrix to be orthogonal and by setting additional constraints. For the Daubechies 4 wavelet these constraints consist in forcing the zeroth and first moments to be zero⁴ and can be calculated analytically. This leads to:

$$c_0 = f(1, 1) \qquad c_1 = f(3, 1) \quad (2.17)$$

$$c_2 = f(3, -1) \qquad c_3 = f(1, -1) \quad (2.18)$$

$$f(a, b) = \frac{a + b\sqrt{3}}{4\sqrt{2}} \quad (2.19)$$

More details about the discrete wavelet transform can be found in [75].

A Daubechies wavelet of order 12 (see Fig. 2.3) is used for all computations in this thesis, as the shape of this specific wavelet is very similar to the investigated intermittent low complexity patterns.

Wavelet Entropy

Two different methods based on the DWT are used in this thesis for quantifying complexity. The first one which will be called wavelet entropy measures simply the deviation of the wavelet coefficients w_i from a uniform distribution. This is quantified using the formula for the Shannon entropy:

$$H_{\text{Wavelet}} = - \sum_{i=1}^N \hat{w}_i \cdot \log_2 \hat{w}_i \quad (2.20)$$

²So that smooth and fine components are in separate sections of the vector: $(s_1, s_2, \dots, s_{N/2}, \phi_1, \phi_2, \dots, \phi_{N/2})^T$

³Several possibilities for padding exist, e.g. padding with zeros or periodic boundaries. In this implementation the reflection method is used. This padding is done using mirrored values of the time series at the boundaries.

⁴A wavelet function $\varphi(t)$ has p vanishing moments if $\int_{-\infty}^{\infty} t^k \cdot \varphi(t) dt = 0, 0 \leq k < p$.

2. Methods

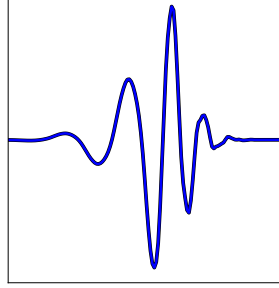


Figure 2.3.: Illustration of a Daubechies wavelet of order 12

where $\hat{w}_i = \frac{|w_i|}{\sum_{i=1}^N |w_i|}$ are the normalized absolute values of the wavelet coefficients w_i calculated in Eq. 2.16.

This quantity will show high values for decompositions having a similar magnitude in all scales which corresponds to signals showing similar patterns on many scales. If the wavelet patterns occur only on specific scales the distribution of w_i will contain several peaks leading to a lower entropy. This quantity weighs single peaks in different scales differently, as a periodic pattern on finer scales will lead to more peaks than a periodic pattern on coarser scales. This can be considered an advantage or a disadvantage depending on the type of patterns under investigation.

Wavelet Energy

The wavelet energy for scale p is computed by directly summing the squares of the wavelet coefficients w_i which belong to p :

$$E_{\text{Wavelet},p} = \sum_{j \in J_p} w_j^2 \quad (2.21)$$

The set of indices J_p for a scale p can be computed as:

$$J_p = \begin{cases} \{1, 2\} & \text{if } p = \log_2 N \\ \{\frac{N}{2^p} + 1, \dots, \frac{N}{2^{p-1}}\} & \text{else} \end{cases} \quad (2.22)$$

By summing over several $E_{\text{Wavelet},p}$ for multiple scales, a fine grained detection of the strength of patterns on specific scales is possible.

2.2. Methods for Quantifying the Spatiotemporal Complexity

In this section methods will be introduced which can be used to quantify the spatial or spatiotemporal complexity. These methods can be applied to simulated data in order to investigate general phenomena of these excitable media in idealized noise-free scenarios. For the application to experimental data, recordings from fluorescence imaging experiments can be used. These data consist of high-frequency camera videos which have recorded the activity of the voltage-sensitive dye during the experiment. The excitation dynamics of these data in general show properties of excitable media which have been discussed in Sec. 1.4.

2.2.1. Phase Synchronisation Index

Synchronisation is a very straight forward property for cardiac tissue as the healthy functioning of the heart heavily relies on synchronized contraction of many heart cells. In the case of arrhythmias reentrant activity like spiral waves leads to a desynchronized contraction of different areas of the heart muscle. Synchronisation can be quantified with the phase synchronisation index.

The phase synchronisation index (PSI) [54] quantifies the strength of phase synchronisation [71] with an arbitrary phase difference. For two oscillators j and k with phases $\Phi_{j,t}$ and $\Phi_{k,t}$ at times t it is defined as

$$\text{PSI}_{j,k} = \left| \frac{1}{N} \sum_{t=1}^N e^{i(\Phi_{j,t} - \Phi_{k,t})} \right| \quad (2.23)$$

For no deviations from phase synchrony in the time range $t \in [1, N]$ it takes the value 1 and for no phase synchronisation it becomes 0.

This quantity can be used to measure the strength of phase synchronisation for an extended excitable system if each element of the excitable medium is considered as an oscillator with a defined phase. The PSI can then be computed individually for each pair of oscillators and then averaged to an overall PSI. As it is desirable to know the strength of phase synchronisation at a specific time, it can be restricted to time windows, similar to the ECG complexity quantities. As the total number of oscillators K for one excitable medium can be very high and the number of PSI pairs grows quadratically with

2. Methods

K , it makes sense to use a subsample of all available oscillators as an approximation of the whole medium. In the case of excitable media this can be considered a good approximation, since the local coupling between neighbouring elements is expected to be very strong and neighbouring elements therefore share a lot of information. In this thesis the phase signals from optical imaging data needed to calculate the PSI are computed by interpolation between zero-crossings of the signal in the same direction.

2.2.2. Analysis of Phase Singularities

The analysis of phase singularities is a well-established method for the quantification of complexity in excitable media [44]. It is particularly useful for the analysis of cardiac dynamics [33, 59, 28, 26, 97, 86, 35]. As it was pointed out in Sec. 1.3 of the introduction, arrhythmias are related to the emergence of spiral wave dynamics on the heart. Phase singularities quantify the number of spiral tips and are therefore able to detect the onset of single spirals and their breakup, leading to fibrillation. Several algorithms exist for computing phases and detecting phase singularities in data obtained in optical mapping experiments or simulation data [48, 67, 87]. One snapshot of the phase at a time t will be called phase map here. A straight forward approach to calculate phase maps for experimental data is the Hilbert transform [67], for simulations a phase can usually be derived directly from the simulation variables.

Despite of the big advantage of providing an intuitive and well-understood interpretation, phase singularity statistics have some major disadvantage for the analysis of fluorescence data of ex vivo experiments:

- Noise can lead to a high rate of misidentifications in some situations which is aggravated by the discrete nature of phase singularities.
- Even when perfectly identified, phase singularities might not be able to completely characterize the spatiotemporal dynamics of a three-dimensional medium, as rotors below the surface can lead to activity on the surface which is not reflected by the number of phase singularities.

Phase singularities are defined as points on the phase map where the phase is undefined. These points are found by computing the curve integral

$$n = \oint_C \nabla \varphi ds \quad (2.24)$$

over a closed loop C with phase φ . If the loop contains one phase singularity $n = \pm 2\pi$. The sign in this equation determines the charge of the phase singularity which differentiates the direction of rotation of the spiral.

Phase singularities can be detected by directly computing the integral in Eq. 2.24 [48], but other algorithms exist [87] that can be faster or more reliable in case of noise. In this thesis a custom algorithm from caostk (See Sec. A.10) which was programmed by Sebastian Berg is used which is based on the detection of isolines in maps of activation times.

Three-Dimensional Phase Filaments

In three-dimensional excitable media the spiral waves gain an additional degree of freedom and therefore form scroll-waves [23]. These patterns rotate around phase filaments which are the three-dimensional generalization of phase singularities. Examples of a visualization of scroll waves and their corresponding phase filaments can be found in Fig. 3.36.

2.2.3. Multi-Dimensional Permutation Entropy

The permutation entropy introduced in Section 2.1.1 can be extended to a multidimensional version. The approach presented here is similar to the one described in [85]. An application of this algorithm to data from embryonic chicken cell culture has been presented in [88].

Two-Dimensional Permutation Entropy

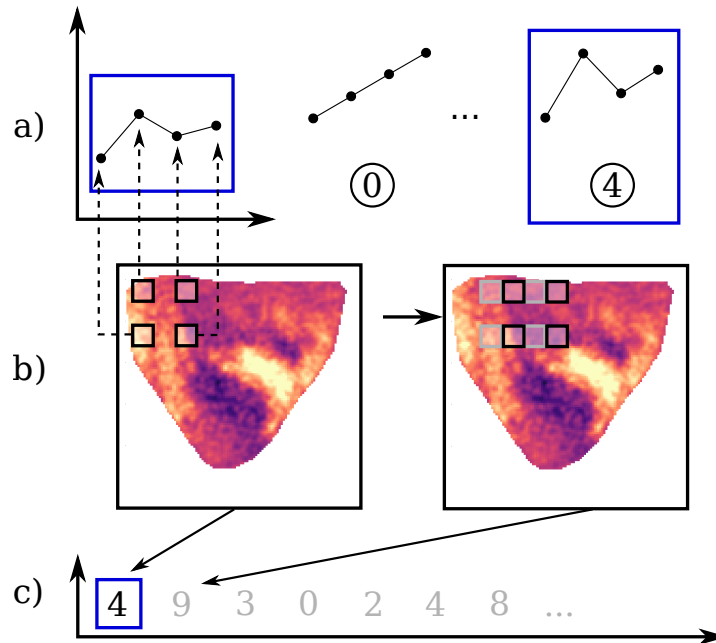


Figure 2.4.: Construction of the series of permutation indices from two-dimensional images. Row b) shows the sampling of the values from the image. These values are treated as a symbol and converted to a permutation index, as is shown in row a). The order in which the values are put into the single symbol does not affect the permutation entropy computed from it. The second image in b) displays the second sampling step which would lead to another permutation index. All the permutation indices for the image (illustrated in c)) will be used to compute the two-dimensional PE.

Fig. 2.4 demonstrates the construction of the two-dimensional PE which is used here. It consists of the following steps:

- Choose a sampling pattern. A simple version which is used here is a $n \times n$ grid where the elements of the grid are apart by a spatial separation L . The quadratic dependency between n and the number of possible symbols⁵ motivates a small value for n , not much bigger than 3. Therefore $n = 2$ has been consistently used for computing the results.
- For each possible position of the sampling matrix on the image, pick up the corresponding values and align them in a specific order. The order itself does not affect

⁵ $n = 3$ will already lead to words of length 9 which will lead to $(n \cdot n)! = 362880$ possible permutation indices

the final permutation entropy, but of course has to be fixed for each image. From these values compute the permutation index using Eq. 2.2.

- From the distribution of permutation indices computed in the second step, calculate the order pattern entropy

$$H = - \sum_{j=0}^{(n \cdot n)!-1} p_j \cdot \log p_j \quad (2.25)$$

The two-dimensional PE which will be abbreviated in the following with PE2D can be interpreted as a quantification of the variety of different spatial patterns. A high value for PE2D indicates a high number of different patterns which occur with similar frequency. A small value for PE2D is achieved for images where very few patterns occur very frequently.

Three-Dimensional Permutation Entropy

A straight-forward continuation of the approach described in the previous section is the construction of a three-dimensional version of permutation entropy (PE3D). A lot of variety exists in the possibilities to extract three-dimensional order patterns, especially in the geometry of the points from which the constituents of each symbol are taken. Here a tripod is chosen for simplicity which is displayed in Fig. 2.5d which leads to four values being selected from a spatiotemporal slice, three from one reference frame at time step t and one from a frame at time step $t + L_t$. L_t will be called temporal lag and should be adapted to the time-scale of the dynamical processes which are seen in the video. The three spatial points of the tripod are separated by a spatial lag L_x ⁶ in x - and y -direction.

The symbol which is extracted by this procedure is lined up as shown in Fig. 2.5a and a permutation index is computed and stored in a series as shown in Fig. 2.5c. Afterwards the tripod is not only shifted in y - and x -direction as it is shown in Fig. 2.6b and Fig. 2.6c, but also shifted in t -direction as it is demonstrated in Fig. 2.6a. This shifting procedure is then repeated for the extents of the image and in t -direction up to a window length. This temporal window length is an important parameter which quantifies how much temporal data will be taken into account for the permutation entropy.

⁶Of course the usage of two different spatial lags would be possible, but a single one is used here. Different spatial lags would make sense if patterns are expected to show different length-scales in different directions of the video data, as it might be the case for systems with very anisotropic wave propagation.

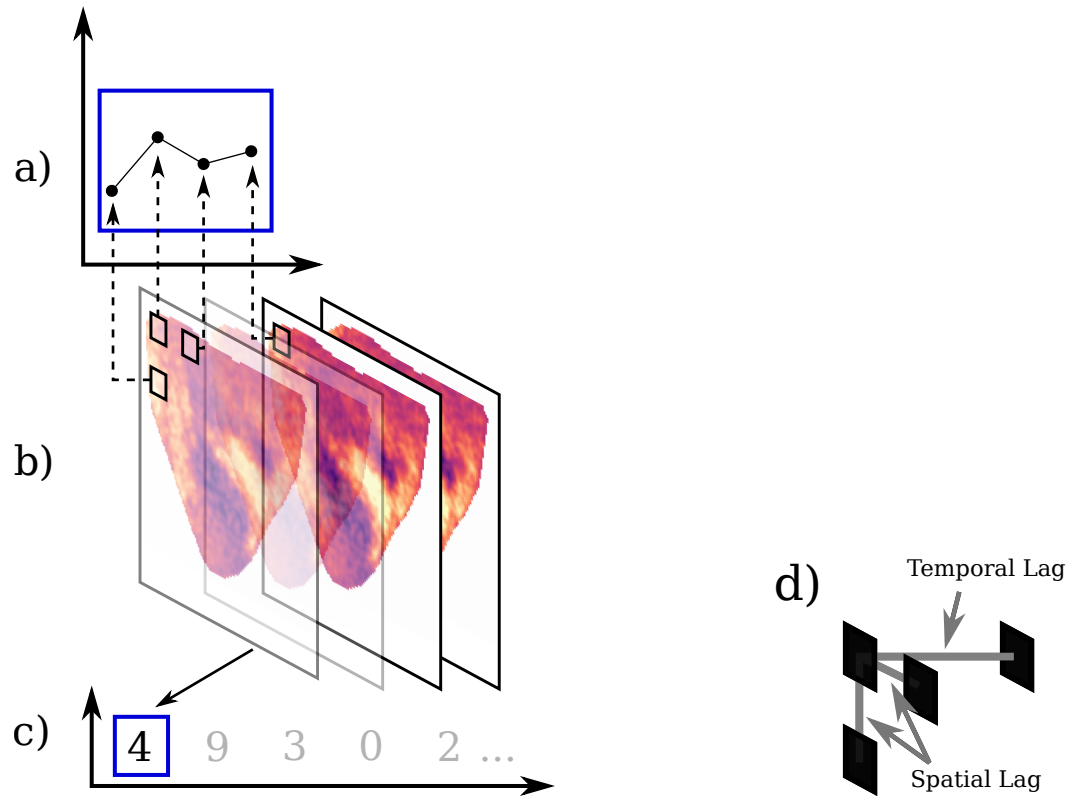


Figure 2.5.: Visualization of the process of computing three-dimensional permutation entropies. a) shows one symbol extracted from the three-dimensional tripod shown in d). In b) one possible position of the tripod is sketched and it is illustrated that values are taken from points in space and time simultaneously. Each slice visible in different levels of transparency refers to one single frame in a video. c) shows the series of permutation indices extracted for the computation of one value for the three-dimensional permutation entropy. d) visualizes the tripod which is one very simple possibility to extract spatiotemporal permutation indices. The temporal lag should be chosen independently from the spatial lag in order to adapt the analysis to the time-scale of the investigated system.

The permutation entropy itself is computed again according to Eq. 2.25 by using all permutation indices obtained during the sliding procedure. Afterwards the procedure is repeated for another reference frame at time step $t + 1$ so that a time series of PE3D values can be calculated.

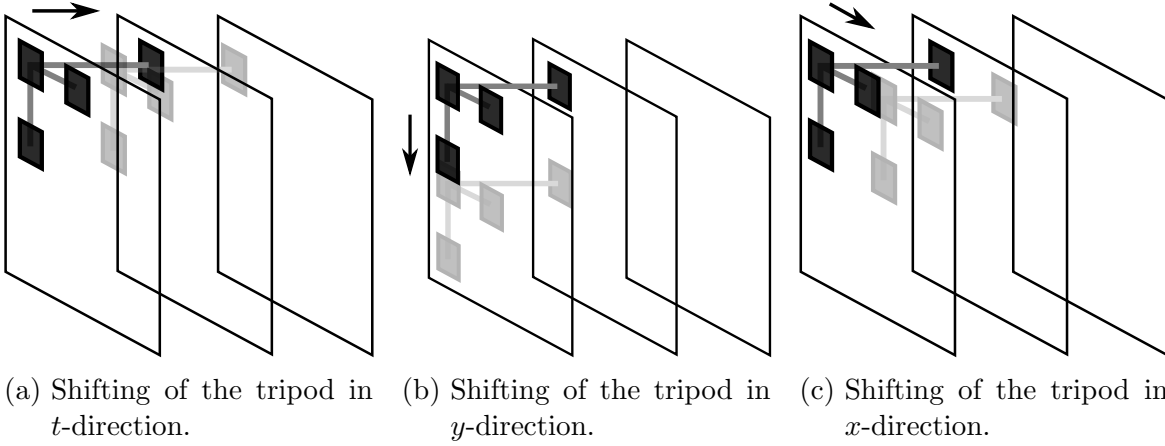


Figure 2.6.: Illustration of the process of sliding the tripod over the video data for the computation of the three-dimensional permutation entropy as it is described in Sec. 2.2.3. The shifting-procedure is repeated spatially for all possible spatial locations and temporally up to a window length.

2.3. ECG Definitions for Numerical Simulations

A commonly used approach for defining an ECG for data from numerical simulations or optical recordings is the pseudo ECG (PECG) which is just the (time-dependent) average over the images or three dimensional volumes:

$$\text{PECG}(t) = \frac{1}{V} \int_V s(\vec{r}', t) d^3\vec{r}' \quad (2.26)$$

In this notation V denotes the total volume or area and $s(\vec{r}', t)$ is the signal at point \vec{r}' of the image or three-dimensional object at time t .

This perspective has the major disadvantage of equally weighting all its constituting signals, while in a realistic ECG the positions of the electrodes and their distance to the heart tissue have a major impact on the measured signal. A more realistic ECG which takes position and distance into account can be defined by [73]:

$$\text{RECG}(\vec{r}, t) = \int_V \frac{D}{|\vec{r} - \vec{r}'|^3} \nabla s(\vec{r}', t) \cdot (\vec{r} - \vec{r}') d^3\vec{r}' \quad (2.27)$$

In this definition D is the diffusion constant, $\nabla s(\vec{r}', t)$ is the gradient of the membrane potential at time t and position \vec{r}' . The integral is taken over the whole volume containing the electrical activity. \vec{r} is the position of the ECG measurement electrode.

2. Methods

As it was described in Sec. 1.2 the ECG originates from dipole moments which are projected parallelly onto the direction of the measurement electrodes. This is directly modeled by Eq. 2.27.

2.4. Statistical Definitions

2.4.1. Correlation Coefficient

In order to quantify the interdependence between the different measures, the correlation coefficient, which is also known as Pearson product-moment correlation, will be used. It measures the strength of linear dependence between two series of observations and takes values in the interval $[-1, 1]$. A value of 1 indicates complete linear dependence, a value of zero corresponds to no linear dependence and a value of -1 can be called perfectly anticorrelated meaning that the variables are completely linearly dependent when one of the variables is multiplied by -1.

The correlation coefficient can be defined in terms of the covariance:

$$C_{x,y} = \frac{\text{cov}(x, y)}{\sqrt{\text{cov}(x, x) \cdot \text{cov}(y, y)}} \quad (2.28)$$

The sample covariance between x and y is defined as:

$$\text{cov}(x, y) = \frac{1}{N-1} \sum_{i=1}^N (x_i - \bar{x}) \cdot (y_i - \bar{y}) \quad (2.29)$$

when x and y have N observations each specified by x_i and y_i and \bar{x} and \bar{y} are their arithmetic mean values.

2.4.2. Weighted Mean and Standard Deviation

In Sec. 3.3.4 the weighted mean and standard deviation are used. These are defined as follows:

$$\text{WMEAN} = \frac{\sum_{i=1}^N w_i \cdot x_i}{\sum_{i=1}^N w_i} \quad (2.30)$$

$$\text{WSTD} = \sqrt{\frac{\sum_{i=1}^N w_i \cdot (x_i - \text{WMEAN})^2}{\sum_{i=1}^N w_i}} \quad (2.31)$$

Eq. 2.31 is the biased weighted standard deviation.

2.4.3. Cohen's h

Cohen's h [27] is a simple quantity to measure the difference between two probabilities, based on the arc sine transformation. It is computed using the arc sine transformation of probability p

$$\phi(p) = 2 \arcsin \sqrt{p} \quad (2.32)$$

and applying it to the two probabilities p_1, p_2 in the comparison:

$$h = \phi(p_1) - \phi(p_2) \quad (2.33)$$

It takes values between $-\pi$ and π . Its absolute value $|h|$ is called undirectional Cohen's h as opposed to the directional version which also shows which of the probabilities is greater.

In Sec. 3.2 this quantity is used to have a simple measure for comparing two relative frequencies.

2.5. Data Preprocessing

This section describes the methods which have been used for preprocessing the data. Preprocessing is necessary especially for the data from fluorescence imaging. The video data acquired there contains several sources of noise:

- Camera specific jitter at a specific frequency
- Noise from the CCD chips

2. Methods

- Long term temporal fluctuations because of photo bleaching and variation in the overall lightness
- High frequency temporal fluctuations due to properties of the light source (e.g. 50 Hz noise)
- Artifacts, like bubbles in the bath, especially due to heating of the electrodes

The data preprocessing of the camera data consists of the following steps:

- Loading and rotation of the data
- Special routine to remove camera jitter
- Bandpass filtering, using a Butterworth filter [21] of order 2 with a lower cutoff frequency at 0.5 Hz and an upper cutoff frequency at 30 Hz.
- Spatial smoothing using a Gaussian kernel with a standard deviation of $\sigma = 1.5$ (pixels)
- Manual masking of the individual video data and cropping to the remaining area

The masking procedure is necessary for removing parts of the camera image which do not belong to the ventricles or which solely contain noise or artifacts.

The ECGs which were in most cases recorded at 10 kHz were sampled to 500 Hz which is sufficient for all analyses applied here and simplifies the synchronization with video data.

2.6. Machine Learning Methods

Machine learning [43] refers to the general task of using algorithms to infer the structure of a specific kind of data which can then be used to identify patterns and statistical dependencies or to predict properties of unseen data. There are two main branches of machine learning. In supervised learning the algorithm which is instructed to fit its model to training data is also taught the result of a target quantity or dependent variable. The fitted models will usually be applied to new datasets where the dependent variable is unknown, in order to obtain a model based classification. In unsupervised learning the structure of the data is inferred without knowing any target variable or class membership of the investigated data points.

Machine learning is already widely used in medical applications, for example in the detection of arrhythmia patterns [104]. A machine learning analysis for predicting the shock outcome of LEAP defibrillation with order pattern statistics derived from simulated pseudo ECGs has been carried out in [50].

In this thesis supervised machine learning is used in order to quantify whether it is possible to predict the shock outcome from complexity parameters which are extracted before the shock. This is analysed in Sec. 3.3.5 for ECGs obtained for rabbit and pig heart ex vivo experiments. Previously, machine learning methods were benchmarked for the application to long-term prediction of cardiac diseases [90].

2.6.1. Decision Trees and Random Forests

There are many different methods for machine learning available, each with different advantages and disadvantages [43, 49]. For biomedical data decision trees have some distinct advantages over other methods:

- They perform a feature selection method by design (see below). This is very helpful in case of heterogenous feature sets.
- The output is very intuitively interpretable by humans.

Decision trees (DT) are hierarchical sets of binary decision rules which form the tree. Each node of the tree contains one rule that can lead to either a specialization of the case to the left branch or the right branch. The leaf nodes of the tree contain the final classification of the case. Rules can test single features for equality in case of categorical features. For numerical data with an order usually a threshold is used which splits the data into two branches. These rules can be combined in a tree in an arbitrary way, also allowing multiple usages of a single feature. In this sense, DTs can combine features in a highly nonlinear way, but usually do not allow for combinations of features within a single splitting-criterion. Analogous to decision trees that generate a categorical classification⁷ regression trees exist which lead to numerical quantities at the leaves.

Many different algorithms exist for generating DTs, very prominently CART [19], ID3 [81] and C4.5 [82]. A very simple strategy to “grow” a tree is recursive binary splitting. This procedure repeatedly selects the best possible split for one feature according to a splitting-criterion. This means that one feature and one threshold for that feature is selected such that the splitting-criterion is optimized.

⁷Therefore, they are also called classification trees.

2. Methods

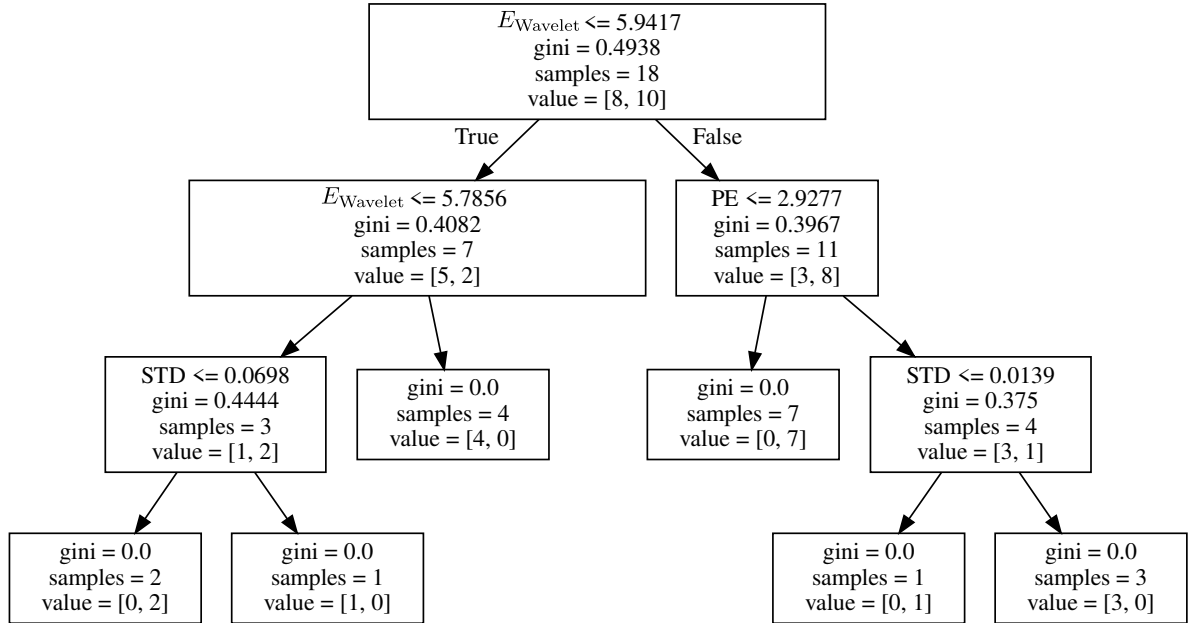


Figure 2.7.: Example of a decision tree using features from the machine learning analysis of the complexity features in Sec. 3.3.5. Each leaf shows the condition for the split including the name of the feature used. The other values give the value of the gini impurity (Eq. 2.34), the samples covered by the split and the distribution of the samples to the classes.

The splitting-criterion that is used in this thesis is the Gini impurity:

$$G = \sum_{i=1}^N p_{ij} \cdot (1 - p_{ij}) \quad (2.34)$$

where p_{ij} is the fraction of cases which belong to class i and are in the j th interval defined by the rule.

DTs can split the data into very fine-grained intervals which can lead to heavy overfitting. There are two common ways to handle this issue:

- Tree pruning [63, 80]: Strategies to simplify the final tree such that it keeps only the most important features.
- Random forests [18]: Use bootstrapping and a restriction of the number of visible features to reduce variance.

In this thesis random forests are used as classification algorithm in Sec. 3.3.5. This classification method uses, as the name already suggests, many trees to build an ensemble classifier. The different trees are grown using datasets generated from the original data using a strategy called bootstrapping [30, 31]: From the real dataset with N samples,

samples are drawn randomly with replacement to create a new dataset with N samples. This step is repeated to generate K artificial datasets derived from the real dataset. For each of these datasets a tree model is grown. Using a majority voting among all these models reduces the variance of the whole model [49]. The feature selection step of the tree growing method causes another problem for the ensemble classifier: There can be a tendency to reuse the same features for all tree models which leads to a high correlation among all trees in the forest. This problem is solved by allowing only a small number of randomly chosen features to be used when selecting each split which reduces the correlation between the tree models.

2.6.2. Cross Validation

For measuring the performance of a classification procedure in cases where not much data is available, cross validation can be used [43]. For this technique the dataset containing n cases is split into k datasets of equal size. In one cross validation step dataset i is used as the validation dataset. The other $k - 1$ datasets are used as the training dataset. This is repeated for all possible values of i and the results are averaged.

The whole procedure is called k -fold cross validation. The special case of $k = n$ is referred to as a leave one out test.

2.6.3. Quantification of Classification Results

For quantification of the classification results the Matthews Correlation Coefficient (MCC) is used [9]. For each series of classifications the number of true positive (TP), true negative (TN), false positive (FP) and false negative (FN) classifications can be determined. A true positive classification would be a correct classification of the class labeled “positive” while a false negative classification would be an incorrect assignment of the label “negative” to a case which has the label “positive” in reality. These four quantities are often presented in the confusion matrix:

$$M = \begin{pmatrix} \text{TP} & \text{FN} \\ \text{FP} & \text{TN} \end{pmatrix} \quad (2.35)$$

A lot of different quantities exist [9, 74] to summarize some or all of these numbers, many of them providing similar information.

Very commonly the fractions sensitivity (SENS), specificity (SPEC), positive predictive value (PPV) and negative predictive value (NPV) are used with the following definitions:

2. Methods

$$\text{SENS} = \frac{\text{TP}}{\text{TP} + \text{FN}} \quad (2.36)$$

$$\text{SPEC} = \frac{\text{TN}}{\text{TN} + \text{FP}} \quad (2.37)$$

$$\text{PPV} = \frac{\text{TP}}{\text{TP} + \text{FP}} \quad (2.38)$$

$$\text{NPV} = \frac{\text{TN}}{\text{TN} + \text{FN}} \quad (2.39)$$

One of the quantities which combines all four numbers of the confusion matrix is the MCC which is defined as follows:

$$\text{MCC} = \frac{\text{TP} \cdot \text{TN} - \text{FP} \cdot \text{FN}}{\sqrt{(\text{TN} + \text{FP}) \cdot (\text{TN} + \text{FN}) \cdot (\text{TP} + \text{FP}) \cdot (\text{TP} + \text{FN})}} \quad (2.40)$$

The MCC takes values between -1 and 1. The maximum value is achieved in the case of a perfect classification while an MCC of zero indicates a classification performance not better than random guessing. Negative values occur when the classification model leads to predictions with swapped classes. For the machine learning analyses in this thesis the MCC has been selected, because it has an intuitive interpretation and combines the results for all four numbers from the confusion matrix [9] without favouring a specific one.

2.6.4. Feature Importances

The feature importance of a decision tree quantifies the contribution of each feature to the classification result. This is usually defined as the cumulative reduction in the criterion that is achieved by splits using that feature. Here the total normalized reduction in the Gini impurity is used. For a random forest the importance of a feature is the average over the single tree feature importances.

3. Results

This chapter starts with an introductory analysis of the phenomenon of complexity fluctuations in the ECG in Sec. 3.1. Each section ends with a summary of the most important findings (Sec. 3.1.1, Sec. 3.2.3, Sec. 3.3.8, Sec. 3.4.4, and Sec. 3.5.6). In Chapter 4 the most important results from this thesis will be summarized and discussed to future research and applications.

The results from Sec. 3.1, Sec. 3.3 and Sec. 3.5 are partially included in [91] and another publication which is currently in preparation. The pacing-strategy presented in Sec. 3.2 has been included in a patent application [89].

3.1. Complexity Fluctuations in the ECG

An example of a VF time series for a human heart from Physionet [41, 39] can be seen in Fig. 3.1. The ECG is taken from subject no. 31 in the database and shows a 50 s excerpt of the first ECG channel starting 200 s after the onset of the VF period. The amplitude of the signal ranges from below 0.1 mV to 0.67 mV. As was described in Sec. 1.5 the prevalently used categorization into coarse and fine VF is based on an amplitude threshold of 0.2 mV. The signal, however, features several patterns which do not simply correspond to a variation in amplitude, but to signal characteristics which might be referred to as “complexity”. A very prominent pattern in the time series is similar to a sine with a variation in amplitude. This type of pattern occurs several times, most obviously starting from 240 s and just before 210 s. These regular patterns are intermittently interrupted by periods of higher complexity showing more frequent turning points and decreases in amplitude. The exact transitions between the different types of these patterns are difficult to differentiate. This observation in combination with previous hints from experiments and literature [56, 52, 72] indicate that it is likely that there are significant differences in the effectiveness of medical treatment depending on fluctuations in patterns of VF, motivated the studies and analyses presented in this thesis.

As it became clear in the previous paragraph, the exact definition of the different patterns observed and the characteristic features should be understood and quantified in

3. Results

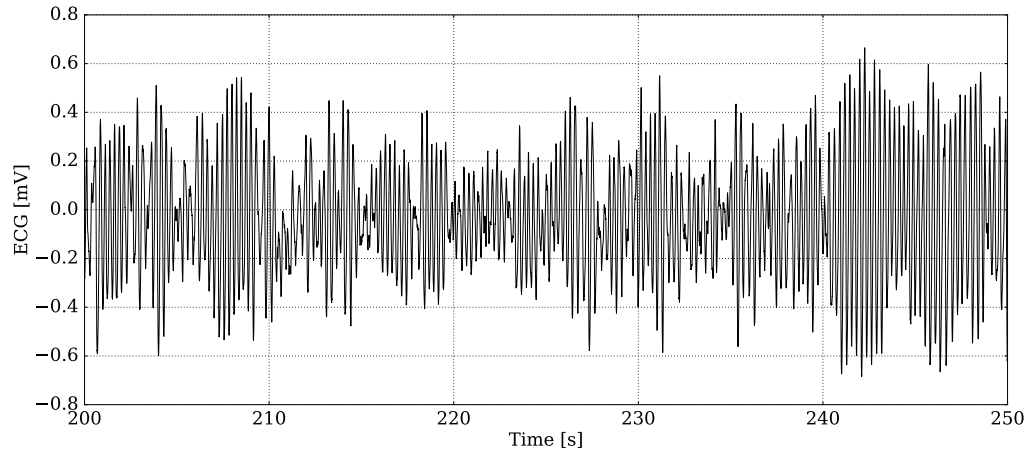


Figure 3.1.: Example for a VF time series from a human heart taken from Physionet Sudden Cardiac Death Holter Database [41, 39]. This diagram shows a 50 s excerpt which starts approximately 200 s after the onset of the VF. The time series is the first ECG channel in the data file and belongs to subject no. 31.

a more detailed way. In this section the permutation entropy (PE) will be used for demonstrating one approach to quantify this complexity. Sec. 3.3.4 will also discuss and compare other approaches from time series analysis and nonlinear dynamics.

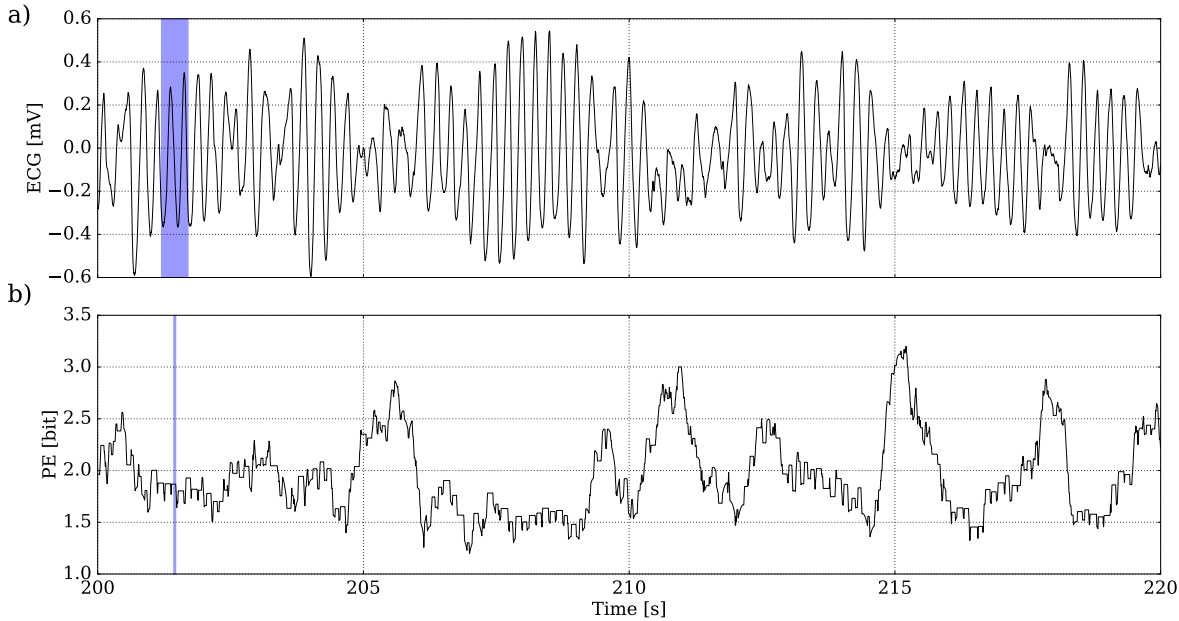


Figure 3.2.: A shorter excerpt of the time series shown in Fig. 3.1 which demonstrates the application of permutation entropy (PE). This excerpt shows a period of 20s which starts approximately 200s after the onset of VF. The time series in a) is the first ECG channel in the data file and belongs to subject no. 31 of the Physionet Sudden Cardiac Death Holter Database [41, 39]. b) shows the PE computed from a) for a window length of 0.5s (denoted by the shaded blue rectangle) and $L = 1$ (4ms). Each point in b) is computed for a centered window which is illustrated by the vertical blue line which belongs to the shaded blue rectangle in a).

The permutation entropy (PE) described in Sec. 2.1.1 and computed using Eq. 2.4 allows for an intuitively interpretable approach for quantifying the distribution of order patterns. In order to demonstrate how this quantity is able to highlight the previously described patterns a shorter excerpt of the time series displayed in Fig. 3.1 is shown in Fig. 3.2.

The PE time series displayed in Fig. 3.2b) takes values between 1.2 bit and 3.2 bit. Low values of the PE can be confirmed to match periods in the signal which are visually less complex. As previously described this complexity can be associated with more turning points in the signal which lead to a higher variety of order patterns. Sec. 3.3.7 discusses the exact nature of the fluctuations in PE more intensively and motivates an algorithm that directly makes use of the specific patterns responsible for it.

The appearance of fluctuations during VF can be observed in different species. In the following paragraphs results from ex vivo experiments with pigs and rabbits are

3. Results

discussed. Fig. 3.3 and Fig. 3.4 show two examples of VF time series acquired during those experiments and the corresponding results for permutation entropy (PE). In both examples PE has been computed for $L = 2$ (4 ms).

Fig. 3.3 shows the time series for a rabbit heart¹. The excerpt starts 35 s after onset of the VF and shows several very distinct phases of low complexity, especially around $t = 38$ s and between $t = 40.6$ s and $t = 42.6$ s. These phases are interrupted by periods of high complexity showing more turning points and local maxima. PE ranges from 1.9 bit to 3.9 bit with the maximum possible PE being $PE_{\max} = \log_2 4! \approx 4.58$ bit. The window length of 250 frames (0.5 s) leads to a blurring of steep transitions between periods of high and low complexity as the overlapping regions contain the symbol distributions of both regimes.

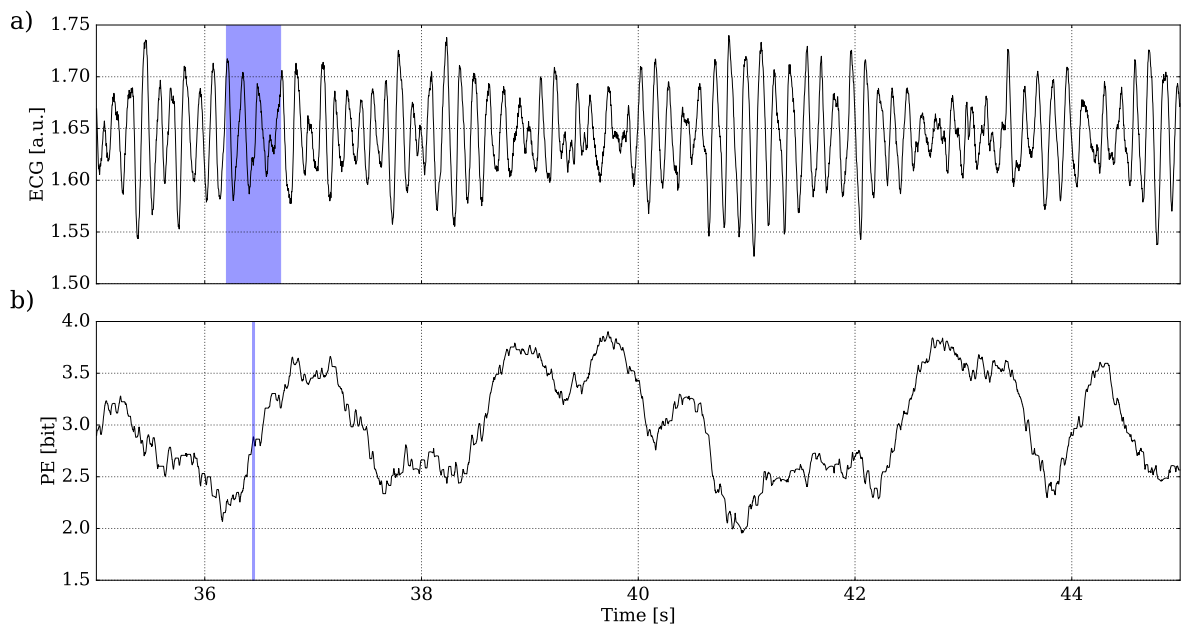


Figure 3.3.: Example for fluctuations in the ECG signal during VF observed in an ex vivo experiment with a rabbit heart. Diagram a) shows the ECG time series and b) shows the PE time series for this excerpt. The starting time of this excerpt is measured after the onset of the VF. The blue rectangle and the blue line indicate the window from which the PE was computed (explained in more detail in Fig. 3.2).

Fig. 3.4 shows a similar example taken from an ex vivo experiment with a pig heart². This excerpt starts 1 s after the onset of the VF and shows several short periods of low complexity. A very distinct one with varying amplitude can be found starting from approximately 2.8 s. This specific excerpt contains PE values between 1.68 bit and

¹Experiment: ID 6, 2016-02-19, pulsar recordings 143342

²Experiment: ID 38, 2016-02-26, pulsar recordings 150312

3.37 bit. Offsets in PE can be explained by different levels of noise in the ECG signal, because noise leads to a higher variation in the symbols observed in addition to the symbols of interest. The exact contribution of specific symbols to the PE in case of VF signals is discussed in Sec. 3.3.7. The reaction of the quantity to noise is discussed in the appendix in Sec. A.3.

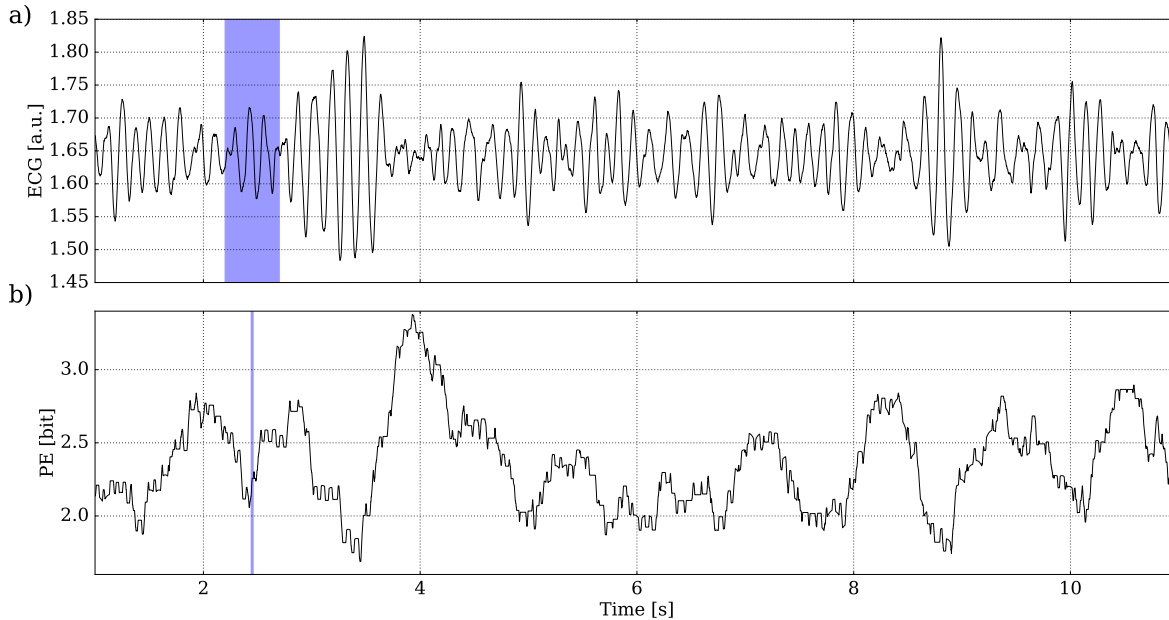


Figure 3.4.: Example for fluctuations in the ECG signal during VF observed in an ex vivo experiment with a pig heart. a) Shows the ECG excerpts which starts 1 s after onset of the VF. b) Displays the corresponding PE time series. The blue rectangle and the blue line indicate the window from which the PE was computed (explained in more detail in Fig. 3.2).

The fourth example shown here makes use of three-dimensional Fenton-Karma simulations which were done by Thomas Lilienkamp (See Sec. 3.5.1 and Sec. A.9). The fluctuations of the artificial ECG which has been calculated according to Eq. 2.27 is displayed in Fig. 3.5 together with the PE time series. As there is no real time-scale defined for this type of cardiac model the time is given in simulation frames here. The PE has been computed using $L = 2$ and a window length of 250 frames. Complexity fluctuations in the ECG are clearly visible and highlighted by the PE. Especially the very prominent period of low complexity between approximately 2630 and 3430 frames is visible very clearly by a drop in PE to 2.4 bit.

3. Results

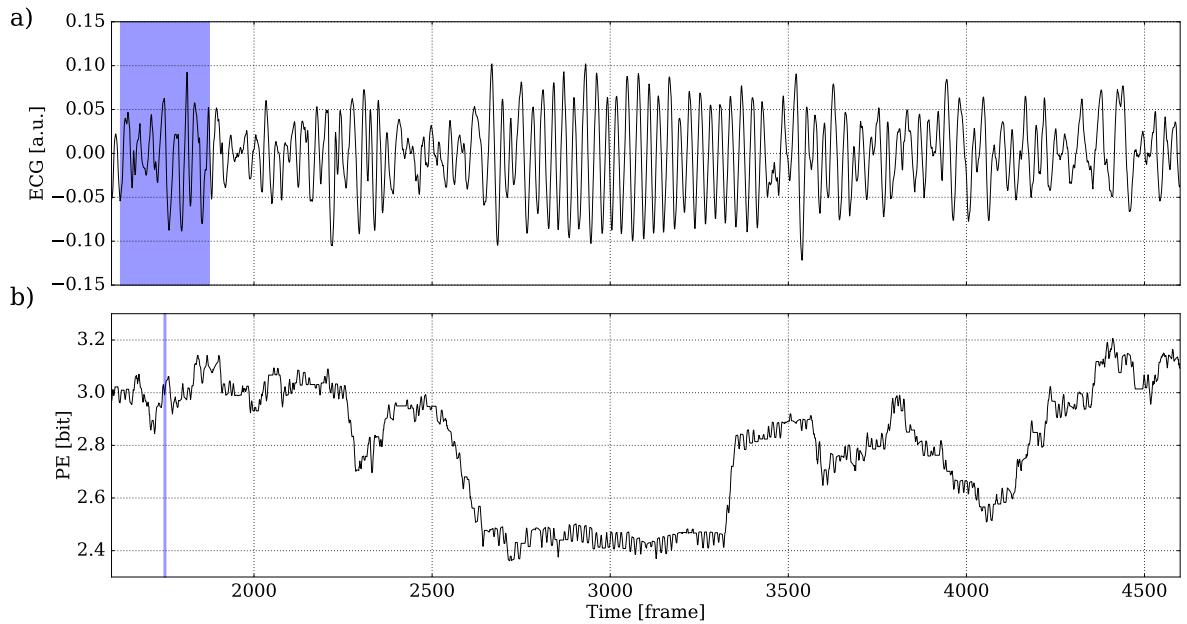


Figure 3.5.: Example for fluctuations in the ECG signal during VF observed in a simulated heart using the Fenton-Karma model. The ECG is computed from the simulated activity according to Eq. 2.27. The time window from which the PE has been computed is indicated by a blue rectangle. The angle of the ECG electrode is 225 degrees (see Fig. 3.42).

3.1.1. Summary and Conclusions

This section can be summarized as follows:

- Complexity fluctuations are visible in the ECG time series of humans, rabbits, pigs and also numerical simulations of excitable media.
- A quantification of these fluctuations is possible using permutation entropy. This quantification allows for an automatic detection of periods of low complexity.

The concepts of coarseness of VF and complexity of VF seem to share a lot of properties which is mainly due to the fact that the low complexity periods have a higher amplitude than the high complexity periods in many cases. Nevertheless, a definition using an amplitude threshold is probably mostly historically motivated and causes difficulties for unconventional ECG setups and simulation studies. Additionally fluctuations in amplitude can appear that hinder an accurate detection of coarse VF. An additional uncertainty of the concept of coarse VF is the timescale of its definition. From the literature it seems that there is no common understanding for which periods of time

changes between coarse and fine VF have to be defined. The complexity fluctuations investigated in this thesis explicitly refer to short timescale complexity fluctuations on the order of fractions of seconds to seconds. The quantification of ECG time series using sliding windows with a fixed length provides a convenient tool for gaining a better understanding of the behaviour of intermittent complexity fluctuations during ventricular fibrillation.

The results from this section were used to design an experiment for testing the hypothesis that defibrillation shocks into periods of different complexities lead to differences in success probabilities. This hypothesis is partly motivated by the observation that “coarse VF” is easier to defibrillate in terms of success probability and defibrillation energy [52, 56, 98]. This experimental series is described in detail in Sec. 3.2.

Another source of motivation for this experiment is the idea that a lower complexity in the ECG also corresponds to a lower complexity in spatiotemporal dynamics which might also be easier to terminate [72]. The correspondence between complexity in the ECG and spatiotemporal dynamics is investigated numerically in Sec. 3.5.1 and using data from fluorescence imaging in Sec. 3.4.3.

In Sec. 3.3.4 the analysis of complexity will be extended to other measures described in the methods section (see Sec. 2.1). Parameters of the complexity measures will be discussed.

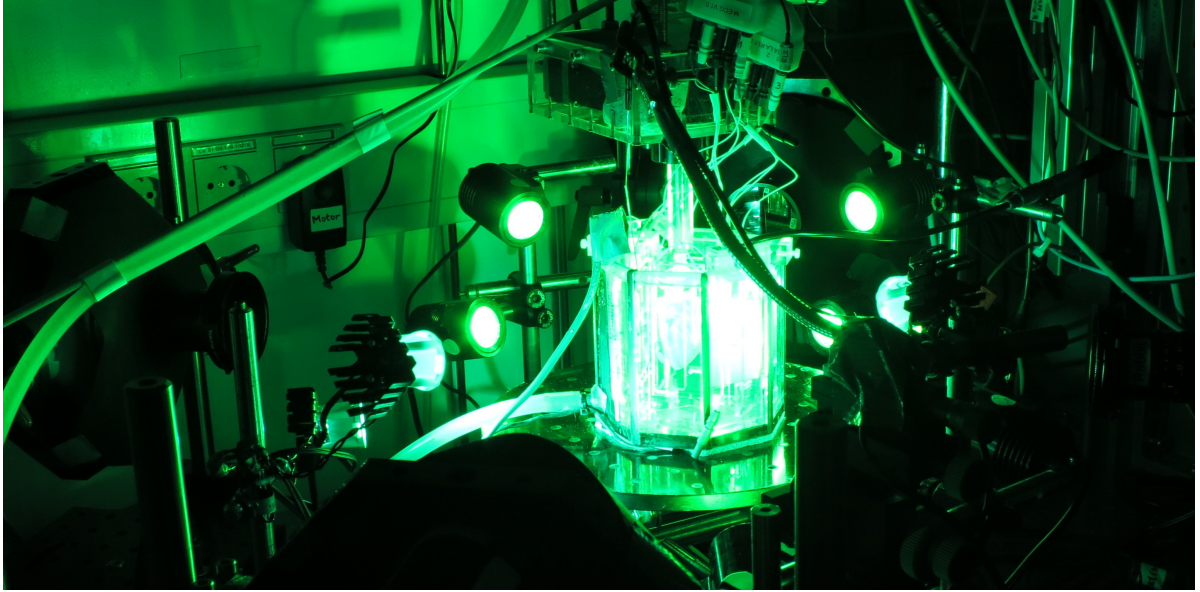


Figure 3.6.: Perfusion setup with rabbit heart in the bath and activated LED lights.

3.2. Experimental Investigation of Complexity-Triggered Interventions

This section discusses the results obtained for a series of experiments which was designed to evaluate the effect of an antifibrillatory pacing-strategy that uses the permutation entropy as a measure for the pulse timing. The pacing-strategy presented here, using defibrillation pulses that are given into periods of a specific complexity regime, has been included into a patent application [89].

This experimental protocol is motivated by the observation that coarse VF seems to be easier to defibrillate than fine VF [52, 56].

As laminar phases are associated³ with a small number of electrical rotors on the cardiac tissue the pacing protocol itself can be optimized for this purpose. Important parameters are the number and the frequency of pulses applied. In the following series of experiments overdrive pacing at a frequency of 1.25 times the dominant frequency has been used and 10 pulses were delivered. The pacing strategy tested here optimises the timing of the first shock depending on the permutation entropy calculated on the fly from the ECG.

The experimental protocol has been established together with the main experimenters Daniel Hornung and Tariq Baig according to the findings in Sec. 3.3 of this thesis. The protocol and the setup are based on previous experimenting techniques as described for

³See Sec. 3.5 which analyses this effect numerically.

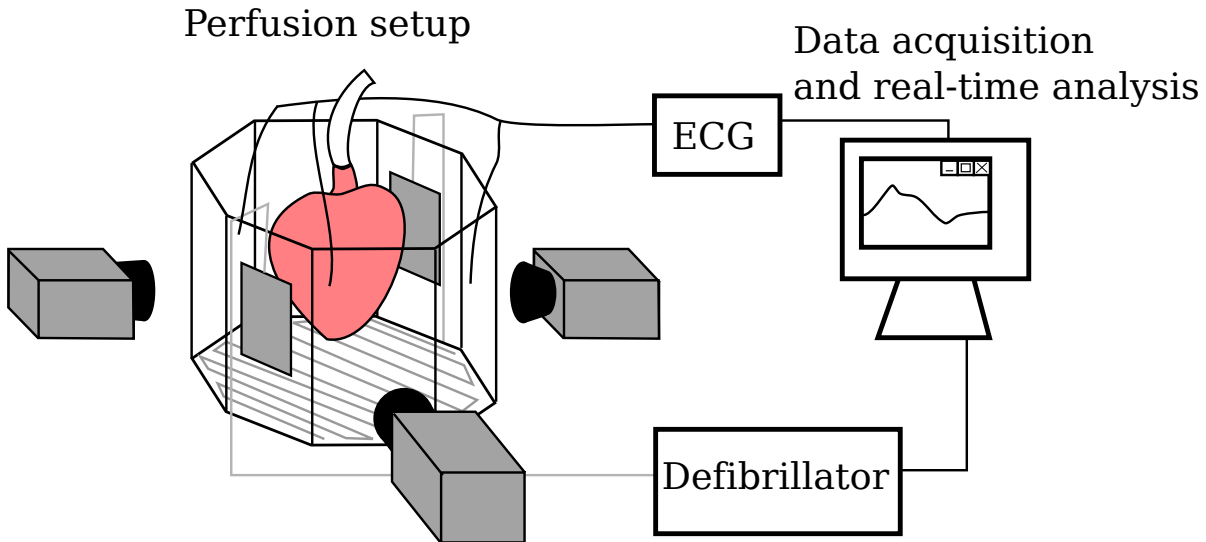


Figure 3.7.: Sketch of the experimental setup for the ex vivo experiments showing the bath with the perfused heart on the left and the data acquisition, real-time data analysis system and shock device on the right. One camera which is located behind the bath is not shown here. Experiment and setup are described in more detail in Ref. [47].

example in Ref. [47].

Fig. 3.7 shows a sketch of the perfusion experiment. The heart is attached to a Langendorff perfusion system in a bath. The Langendorff perfusion [16] is a method to supply the heart with nutrients by pumping Tyrode's solution through the aorta into the heart. The pedal electrodes which are used to apply electric far field shocks to the heart are attached to the defibrillator which is controlled by a computer system. The custom Pulsar⁴ software is capable of performing a real-time analysis of the ECG signals measured from the sketched electrodes inside the bath and applying defibrillation shocks depending on the ECG complexity. More details about the setup and preparation of the animal model are given in the Sec. A.6.

Three goals were set initially:

1. Determine the difference in success rates for defibrillation with the 10 pulse monophasic pacing strategy between pacing into a laminar phase of VF and pacing into a complex phase of VF. These measurements should be taken at a constant defibrillation energy which is calibrated to yield approximately 50% success rate when pacing into VF regardless of the complexity.
2. Measure the difference of required energy when comparing to the monophasic single

⁴Pulsar, see appendix, Sec. A.10

3. Results

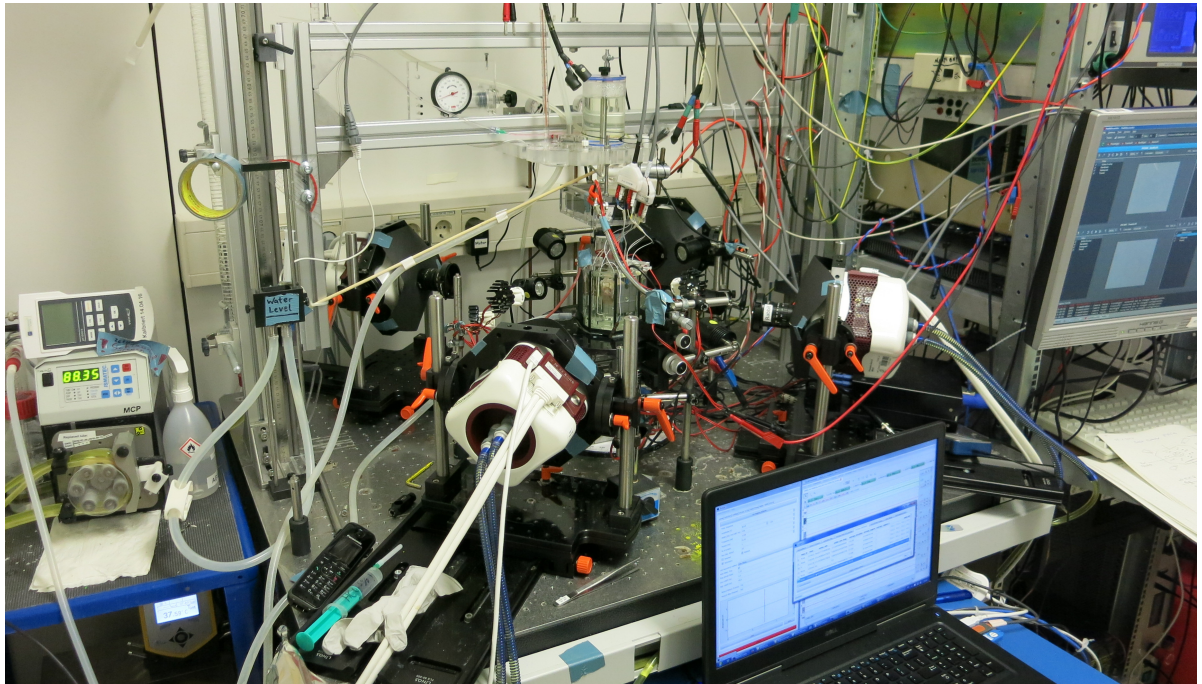


Figure 3.8.: Photo of the experimental setup during an ex vivo experiment. The rabbit heart can be seen in the bath. The four high speed cameras are placed to record the fluorescent activity from four orthogonal sides. The small device on the left side is the perfusion pump. The computer in the front runs the Pulsar experiment software.

3.2. Experimental Investigation of Complexity-Triggered Interventions

shock pacing strategy.

3. Estimate the lowest energy which gives a nonzero defibrillation success probability when using the 10 pulse monophasic pacing strategy.

The main protocol consists of multiple phases:

1. Calibration:

- a) Choose a reasonable starting energy E_0 (based on previous experience)
- b) Determine (monophasic) single shock initial energy $E_{1,M}$ starting from E_0 using a pace-up protocol⁵
- c) Measure 10 pulse monophasic initial energy $E_{10,M}$ starting from $0.5 \cdot E_{1,M}$ into the low PE regime

2. Measurements:

- a) Measurement for estimating the difference in success rates (goal no. 1)
- b) Estimation of the lowest possible energy for defibrillation (goal no. 3)
- c) Interleaved in between phase 2a and phase 2b: Estimate single shock energy (goal no. 2)

Local⁶ burst pacing at 50 Hz or far field shocks have been used for the induction of VF.

Measurement 2a started at $E_{10,M}$. The general proceeding was to attempt defibrillation into a regime which was randomly determined. In case of failure a second shock was attempted into another randomly determined regime. In case of failure of the second shock, the VF was terminated using a backup shock which was either a biphasic single shock or a biphasic five pulse underdrive shock at a higher energy. Waiting time between VF episodes had to be at least 5 min to allow for a recovery of the heart. After the next induction of VF the PE regime was chosen to be the opposite of the first shock of the preceding VF episode. A general guideline was to change the energy in case of approximately three pairs having the same shock outcome. Additionally a direct change was considered if the first pair at a new energy level had the same outcome. This was considered necessary, because the expected number of shock trials per experiment is quite low and it is desirable to sample multiple energy levels. The change in energy

⁵This is done here by increasing the energy in steps of 20% until the first successful defibrillation is reached. This energy is then confirmed by decreasing and increasing the energy again at least one time.

⁶Using a stimulation electrode.

3. Results

was 20% upwards in case of too few successes and 20% downwards in case of too many successes. It was not always possible to completely stick to this measurement protocol, especially in the case of many self-terminations or high energy requirements.

3.2.1. Experimental Results

The results are presented in two different representations. Figures 3.10 to 3.15 show overviews over the series of shocks given during the experiment. The time axis is not linear, but event-based, because it would not be possible to display a full experiment without a lot of overlap of events. Only four relevant types of different shock events are included⁷:

- Filled square: monophasic single shock
- Circle: 5 pulse biphasic shock⁸
- ▽ Triangle pointing downwards: 10 pulse monophasic shock into a low PE phase
- △ Triangle pointing upwards: 10 pulse monophasic shock into a high PE phase

The second display is Tab. 3.1 containing the counts of successes and misses for laminar and complex phases respectively for constant amplitude levels. This is an overview over the whole experimental day, so the relationship between pairs of shocks as described in the protocol are not taken into account here. Single pacing events are not included, as they were exclusively needed to scan for an appropriate energy as described in the protocol. For comparing the results more easily Cohen's h (see Sec. 2.4.3) is given in the last column for the relative frequencies:

$$P(\text{Laminar}) = \frac{N_{\text{Success}}^{\text{Laminar}}}{N_{\text{No Success}}^{\text{Laminar}} + N_{\text{Success}}^{\text{Laminar}}} \quad (3.1)$$

$$P(\text{Complex}) = \frac{N_{\text{Success}}^{\text{Complex}}}{N_{\text{No Success}}^{\text{Complex}} + N_{\text{Success}}^{\text{Complex}}} \quad (3.2)$$

As described in the methods section, Cohen's h will be larger than 0 for rows favoring the success probability of laminar phases and less than zero for rows favoring the

⁷On some experimental days additionally to the experimental protocol described here, other protocols were used for investigating other termination strategies. This includes measurements on ventricular tachycardia (VT) in cases where such an arrhythmia was present.

⁸The majority of 5 pulse shocks was given as biphasic underdrive shocks with some exceptions. These pulses were mostly used as backups shocks to terminate the arrhythmia.

3.2. Experimental Investigation of Complexity-Triggered Interventions

corresponding probability for complex phases with $-\pi$ and π being the respective extreme points. This quantity is solely employed for facilitating the overview over the experiments and does not make any statement about significance.

Shock Amplitude	Laminar		Complex		Cohen's h
	$N_{\text{Success}}^{\text{Laminar}}$	$N_{\text{No Success}}^{\text{Laminar}}$	$N_{\text{Success}}^{\text{Complex}}$	$N_{\text{No Success}}^{\text{Complex}}$	
2016-02-18 / Rabbit Ex Vivo					
No VF induction possible					
2016-02-19 / Rabbit Ex Vivo					
68 V	5	2	1	6	1.24
74 V	2	0	2	0	0.0
2016-02-29 / Rabbit Ex Vivo					
Note that the data for this experiment includes three shocks into VT.					
16 V	0	2	0	1	0.0
62 V	4	4	4	3	-0.14
2016-03-09 / Rabbit Ex Vivo					
28 V	1	1	0	2	1.57
29 V	1	2	0	3	1.23
35 V	1	2	1	2	0.0
38 V	0	2	0	2	0.0
46 V	1	1	2	0	-1.57
62 V	2	1	1	0	-1.23
2016-03-10 / Rabbit Ex Vivo					
62 V	0	1	1	0	-3.14
68 V	1	0	2	0	0.0
2016-04-12 / Rabbit Ex Vivo					
No usable entropy pacing events.					

Table 3.1.: Descriptive results of the entropy pacing experiment series.

3. Results

Shock Amplitude	Laminar		Complex		Cohen's h
	$N_{\text{Success}}^{\text{Laminar}}$	$N_{\text{No Success}}^{\text{Laminar}}$	$N_{\text{Success}}^{\text{Complex}}$	$N_{\text{No Success}}^{\text{Complex}}$	
2016-04-14 / Rabbit Ex Vivo					
No usable entropy pacing events.					
2016-04-19 / Rabbit Ex Vivo					
20 V	0	3	0	0	NaN
42 V	1	2	1	0	-1.91
2016-02-24 / Pig Ex Vivo					
740 V	0	2	1	1	-1.57
840 V	0	3	0	2	0.0
920 V	0	1	0	3	0.0
1000 V	2	6	3	5	-0.27
2016-02-25 / Pig Ex Vivo					
51 V	0	3	0	5	0.0
220 V	0	1	0	1	0.0
260 V	1	0	1	0	0.0
620 V	1	1	1	2	0.34
680 V	7	3	6	3	0.07
740 V	1	0	1	0	0.0
2016-02-26 / Pig Ex Vivo					
260 V	0	4	0	4	0.0
290 V	0	4	0	4	0.0
450 V	0	3	0	1	0.0
510 V	2	3	1	3	0.32
590 V	3	0	1	1	1.57
620 V	7	0	4	3	1.43
680 V	1	0	1	0	0.0

Table 3.1.: Descriptive results of the entropy pacing experiment series.

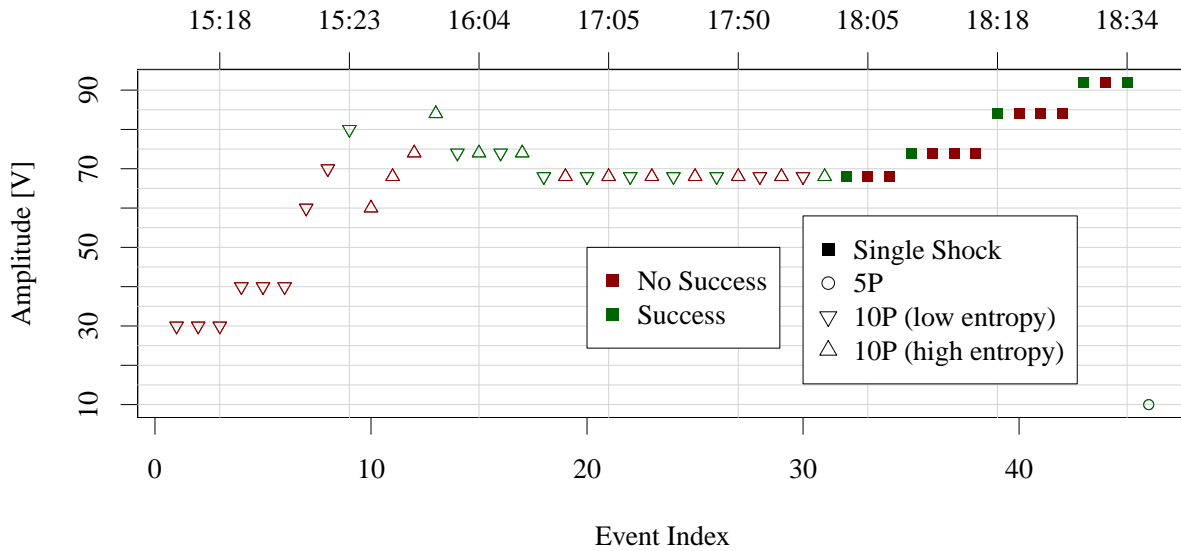


Figure 3.9.: Overview over the ex vivo experiment with a rabbit heart which was done on 2016-02-19 to investigate the effect of the ECG complexity at the shock timing on the shock outcome. Red symbols denote unsuccessful shock trials and green symbols denote successful shock trials.

Fig. 3.9 shows an overview over the experiment with a rabbit heart on 2016-02-19. After one initial experiment on 2016-02-18 where sustained VF induction was not possible, this was the first heart with an application of the entropy pacing protocol described here. On this experiment day a slightly different protocol was used which did not specify the randomization of the entropy regime. Capture voltage⁹ was determined to a value between 6.5 V and 7.9 V. Sustained VF induction was possible, but difficult, showing many self-terminations. The beginning of the figure shows the calibration of the energy for overdrive pacing. At 15:44 the initial amplitude was set to 74 V. As four pulse sequences of entropy pacing into the different regimes were possible the voltage was lowered to 68 V at 16:32. The entropy threshold had been slightly recalibrated shortly afterwards (16:44) from initially 3.4 ± 0.7 to 3.5 ± 0.7 . Until 18:00 a series of shocks was observed which mostly followed the expectation: A successful termination was possible for the low entropy regime five out of seven times whereas no success was achieved for the corresponding high entropy pacing attempts in six out of seven trials. At 18:02 no sinus rhythm was observed anymore. Until 18:34 several single shocks were attempted in order to measure the single shock defibrillation threshold. Two terminations at the same energy were possible at 92 V. A five pulse shock attempt at 10 V at 18:41 confirmed that the defibrillation threshold had decreased drastically and the experiment was ended. This experiment motivated the randomization of the entropy regime successive protocols in order to prevent effects due to the testing order of the different permutation entropy regimes.

⁹The lowest voltage for which excitation waves could be initiated in the tissue.

3. Results

Results for successive experiments with rabbit hearts are shown in Fig. 3.10, Fig. 3.11 and Fig. 3.12. In the experiment on 2016-02-29 it was possible to test a series of shocks at the same voltage level of 62 V. In this case almost equal success probabilities for laminar and complex PE regimes were observed. During this experiment some of the shocks for the low PE regime were accidentally given into a ventricular tachycardia (VT). These shocks are marked with a black rectangle in the figure. The experiment on 2016-03-09 showed some successes at lower voltages around 30 V. In these cases shocks into laminar PE regimes were found to be slightly more successful, but due to the low number of trials this result is far from being significant. The experiment on 2016-04-19 did not yield enough shock trials for interpretation.

Overviews over the three ex vivo experiments done with pig hearts are shown in Fig. 3.13, Fig. 3.14 and Fig. 3.15. In the experiment on 2016-02-24 it was very difficult to defibrillate the heart during VF at reasonable voltages. After a long period of non-successful defibrillation trials at high voltages, defibrillation became possible around 1000 V. One series of pacing into the different PE regimes was recorded between 19:12 and 21:32. During this series shocks into the complex PE regime were slightly more successful. The second experiment with a pig on 2016-02-25 showed a slightly higher success probability for pacing into the low PE regime at voltages between 620 V and 680 V. A series of trials at low voltages (51 V) did not yield to any successful defibrillation attempt regardless of the permutation entropy. During the experiment on 2016-02-26 a long series of defibrillation attempts was tried at medium voltages (260 V to 290 V) without any successful events. Later in the experiment (starting from 18:03) a series of defibrillation attempts was recorded which suggests that defibrillation trials into laminar phases have a higher chance of success than the trials into the other regime. This seemed to be the case at 620 V. At 590 V a similar result, but with less defibrillation attempts, was yielded.

In total, not much evidence was found, that pacing into laminar phases leads to better success probabilities than pacing into complex phases. Two series, one in the rabbit ex vivo experiment on 2016-02-19 and one in the pig ex vivo experiment on 2016-02-26, look promising, but could not be reproduced during the other experiments. The total number of experimental data points is still too low, to give a reliable answer. Pacing at very low energies was tried several times, but did not lead to successful defibrillation attempts. This result is not surprising, as generally a very low success probability for defibrillation can be expected at these voltages.

3.2. Experimental Investigation of Complexity-Triggered Interventions

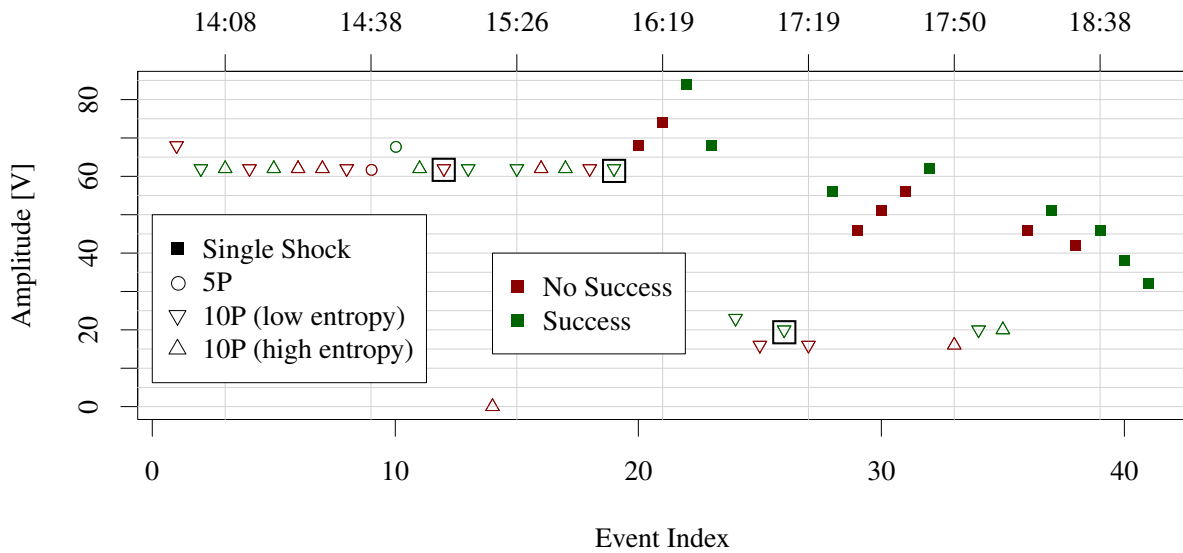


Figure 3.10.: Overview over the ex vivo experiment with a rabbit heart which was done on 2016-02-29. This experiment includes some low PE shocks which were accidentally given into a ventricular tachycardia (VT). These shocks are marked with a black rectangle.

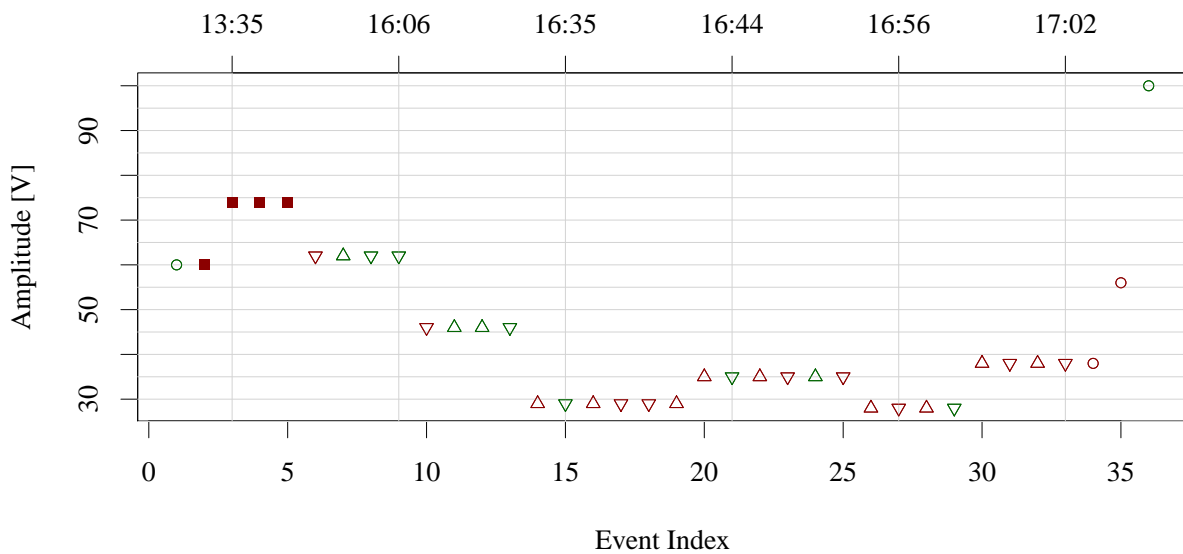


Figure 3.11.: Overview over the ex vivo experiment with a rabbit heart which was done on 2016-03-09. The meaning of the symbols is the same as in Fig. 3.9.

3. Results

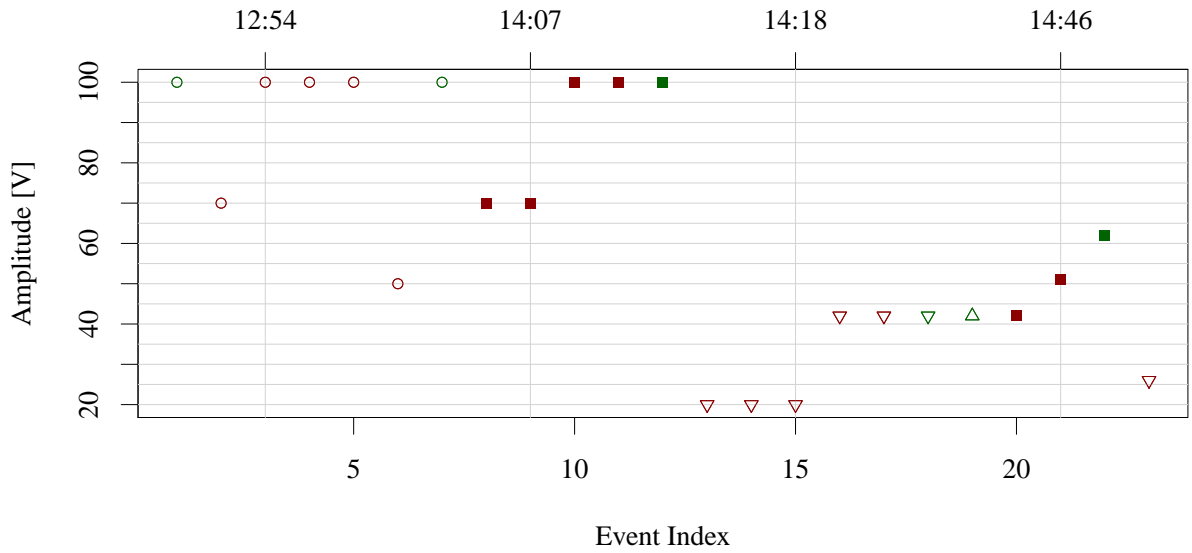


Figure 3.12.: Overview over the ex vivo experiment with a rabbit heart which was done on 2016-04-19. The meaning of the symbols is the same as in Fig. 3.9.

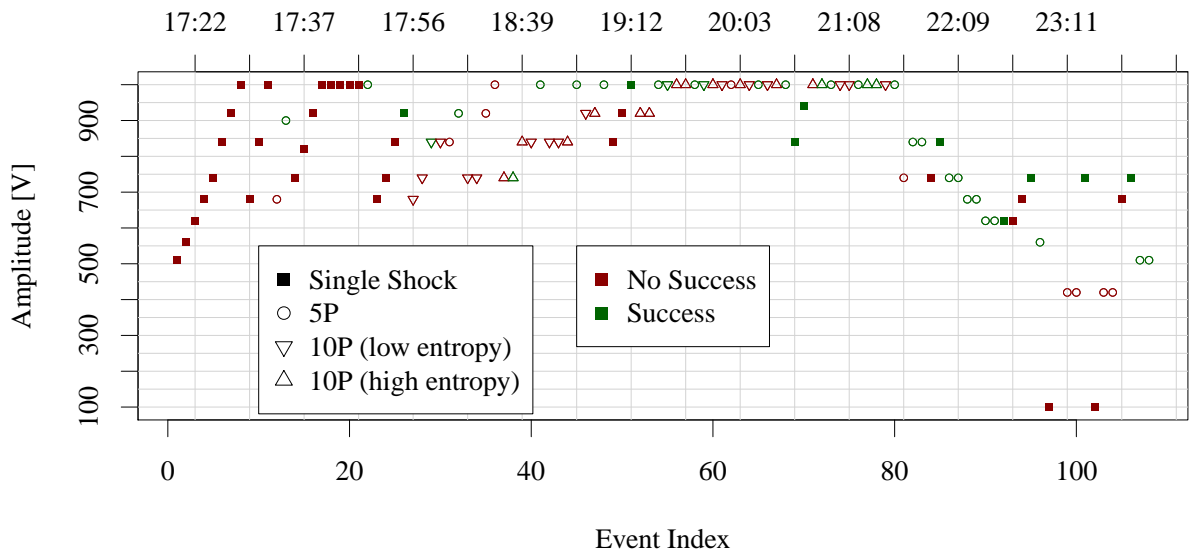


Figure 3.13.: Overview over the ex vivo experiment with a pig heart which was done on 2016-02-24.

3.2. Experimental Investigation of Complexity-Triggered Interventions

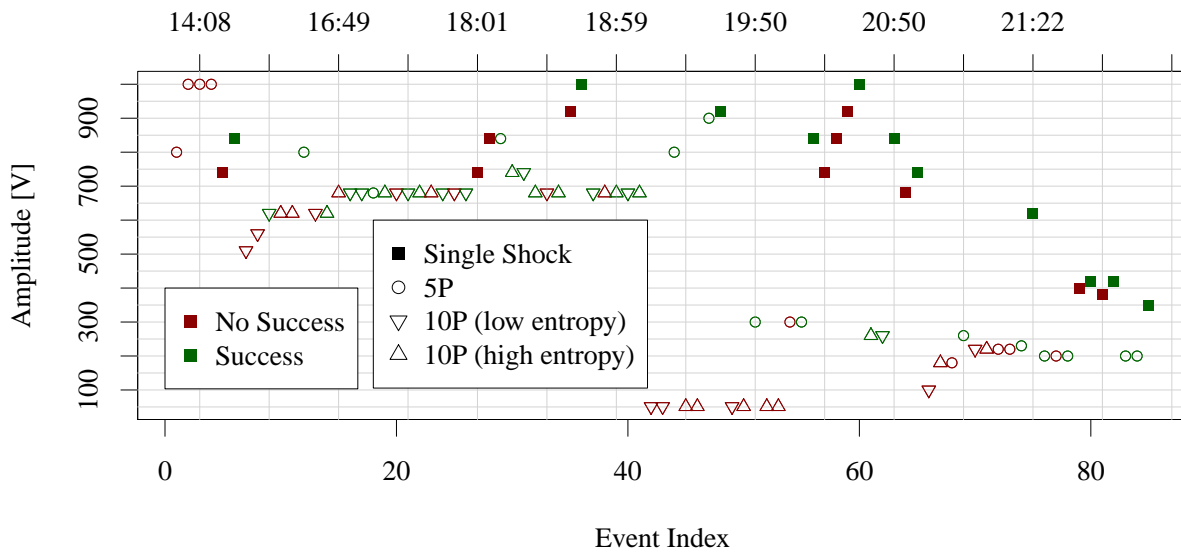


Figure 3.14.: Overview over the ex vivo experiment with a pig heart which was done on 2016-02-25.

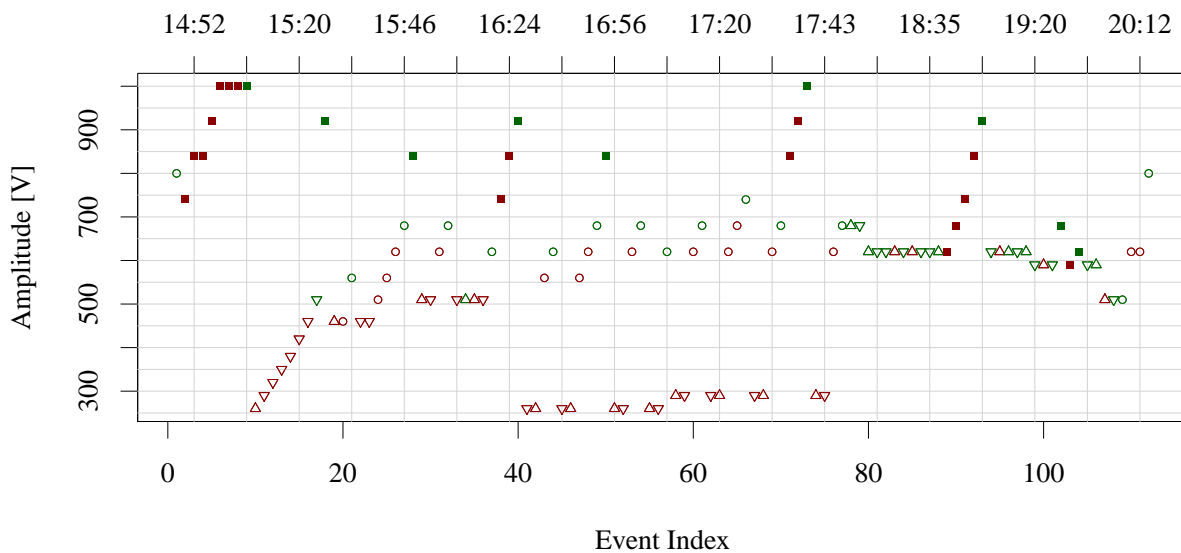


Figure 3.15.: Overview over the ex vivo experiment with a pig heart which was done on 2016-02-26. The meaning of the symbols is the same as in Fig. 3.9.

3.2.2. Energy Reductions

Although the primary goal of the experiment series was to measure differences in success probabilities between the low complexity and the high complexity PE regimes, some very rough estimates of energy reductions can be given for some of the experiment series. It

3. Results

is very important to point out that these values have to be taken with extreme care as there are several shortcomings that spoil their significance:

- In most of the experiments there is a very small amount of measurement points of single shock attempts.
- Each single shock measurement, if present, only consists of a small number of trials and not in the systematic recording of a defibrillation threshold curve.
- There is a considerable amount of variation within the defibrillation threshold over time. Especially there is a significant drop in the single shock defibrillation energy at the end of the experiment and it is often not clear when exactly this drop started.

Rabbit Ex Vivo Experiments

In case of the rabbit ex vivo experiments the energy reductions are calculated directly from the voltages. See Sec. A.1 for details.

On 2016-02-29 a very short series of entropy pacing events was recorded at quite low voltages starting from 16:38 with a preceding and successive measurement of single shock defibrillation attempts. Taking the conservative¹⁰ estimate of the successful single shock defibrillation voltage at 56 V and assuming that the single low PE defibrillation trial at 23 V is realistic, the estimated energy reduction is 83%.

On 2016-04-19 one short series of entropy pacing events was recorded at 42 V with a successive small series of single shock trials with the first successful shock at 62 V. The energy reduction is 54% in this case.

Pig Ex Vivo Experiments

For the experiment on 2016-02-25 several estimates of the energy reduction can be given:

- The first successful single shock at 16:10 with an energy of 35.56 J compared to the average energy of the successive two successful 10 pulse shocks (at 620 V) of 19.12 J result in an energy reduction of 46%.
- The successful single shock at 18:39 with an energy of 53.04 J compared to the series of preceding and successive 10 pulse shocks at 680 V with 6 successful attempts

¹⁰This is the shock with the lower energy here.

3.2. Experimental Investigation of Complexity-Triggered Interventions

and an average energy of 23.73 J lead to an energy reduction of 55%.

- The successful single shock with the lowest energy of the series of single shocks between 20:05 and 20:57 delivered an energy of 30.68 J. Compared to the two successful 10 pulse defibrillation attempts at 260 V which have an average energy of 3.5 J this gives an energy reduction of 89%.

For the experiment on 2016-02-26 three different estimates of the energy reduction are possible:

- The comparison of one successful single shock at 14:55 and an energy of 59.65 J (1000 V) and the preceding 10 pulse shock at 510 V and an average energy of 14.57 J leads to an energy reduction of 76%.
- The successful 10 pulse shock at 16:09 and an average energy of 14.57 J (510 V) compared to the following successful single shock at 16:25 with an energy of 48.85 J (920 V) results in an energy reduction of 70%.
- The average energy of the successful trials of the series of 10 pulse shocks at 620 V of 21.27 J can be compared to the enclosed successful single shock at 47.79 J which results in an energy reduction of 55%.

Shortly after the third estimate of the energy reduction the energy for the single shock dropped heavily and almost no energy reduction was observed anymore. Therefore the last value can be considered very unreliable.

3.2.3. Summary and Conclusions

In general this series of experiments did not show reliable differences between pacing during the more complex periods and pacing during the less complex periods in the ECG. There were two experiments showing a higher success rate for laminar phases on 2016-02-19 and 2016-02-26. Although there were periods in other experiments showing a dependency of the shock outcome on the ECG complexity, these results do not seem to be stable and sometimes slightly favor different complexity regimes.

Similar statements also hold for the energy reductions reported in Sec. 3.2.2 which are based on a very sparse amount of data and should only be taken as very preliminary estimates.

It must be pointed out that the absolute number of shock trials at constant energies and comparable experimental conditions is quite low and more experiments are needed

3. Results

for a reliable statement. However, there are several conceptual issues that might need improvement before being able to make use of this pacing strategy in a reliable manner:

- The information recorded by a single ECG channel could be not sufficient to make a reliable statement about the dynamical state. This problem will be analysed and discussed in detail in Sec. 3.5.
- The shock protocol might not be appropriate for the respective dynamical state. This especially includes the question of underdrive or overdrive pacing and the exact number of shocks. To answer this question, more work is needed to investigate the detailed mechanisms of termination both experimentally and numerically.

One interesting conclusion can be drawn regarding the relation between laminar phases in VF and VT. VT should generally be considered different to laminar phases in several aspects, most prominently frequency and stability. However there might be a similarity in the low number of rotors as it is also supported by the analysis presented in Sec. 3.5¹¹. Pacing into VT was not explicitly tested here, but literature implies that it is definitely easier to defibrillate than VF [100]. That leads to the conjecture from the experimental results presented here that that laminar phases are not as easy to defibrillate as VT. This would confirm the hypothesis that laminar phases belong to a spatiotemporal state that is different to VT.

The experiments from this series produced many high quality ECG time series datasets which were used in most sections of the results chapter in this thesis. The next section analyses and compares several complexity measures for ECG time series using this data.

¹¹Although in laminar phases of VF there currently is no necessity of a single rotor, while that can be considered secured for VT.

3.3. Quantification of Complexity Fluctuations in the ECG

Sec. 3.1 discussed complexity fluctuations in the ECG during VF using permutation entropy (PE). In this section several other methods for quantifying the complexity of time series (Sec. 2.1) are discussed.

The section will start with in-depth discussions of PE (Sec. 3.3.1), PCA entropy (Sec. 3.3.2), wavelet entropy, and wavelet energy (Sec. 3.3.3). All quantities from Sec. 2.1 are compared using correlation matrices in Sec. 3.3.4. An application of machine learning methods using the complexity quantities for predicting the shock outcome of the defibrillation attempts from the ex vivo experiments is discussed in Sec. 3.3.5. Statistical properties such as durations and relative frequencies of laminar phases are discussed in Sec. 3.3.6. Sec. 3.3.7 discusses findings for optimizing the detection of low complexity periods by analysing the exact patterns responsible for generating the fluctuations in PE. Throughout this section all quantities have been computed using the same window length of 250 frames (0.5 s). A discussion of the effect of the window length is found in Sec. A.4.

Parts of the results of Sec. 3.3.1-Sec. 3.3.4 are contained in [91].

3.3.1. Permutation Entropy

The first quantity which is discussed here in detail is the permutation entropy described in Sec. 2.1.1 (Eq. 2.4). One important parameter is the embedding delay L . Fig. 3.16 shows another case of VF recorded during an ex vivo rabbit heart experiment¹². Two overview plots in c) and d) show differences obtained when scanning L from $L = 1$ (2 ms) to $L = 40$ (80 ms): c) Displays the plain results for PE over time in color code. d) Shows a normalized version of c) with each row being normalized by mean and standard deviation. Two important conclusions can be drawn from this figure:

- There is a rise in PE values when going to higher values for L . The maximum PE for $L = 1$ is 3.8 while it achieves a maximum of 4.47 for $L = 17$.
- The approximate location of periods of low complexity does not seem to change much when varying L . This can be quantified with the average correlation of 0.68 between PE time series for different L .

In this range of values for L , laminar phases should be detectable regardless of the exact value. However, there are some considerations which lead to a preference of smaller L :

¹²Experiment: ID 32, 2016-02-19, 161201

3. Results

The difference between maximum and minimum value for the PE values at a constant L have a maximum at $L = 2$ of 1.93 suggesting a larger separation of low complexity and high complexity phases.

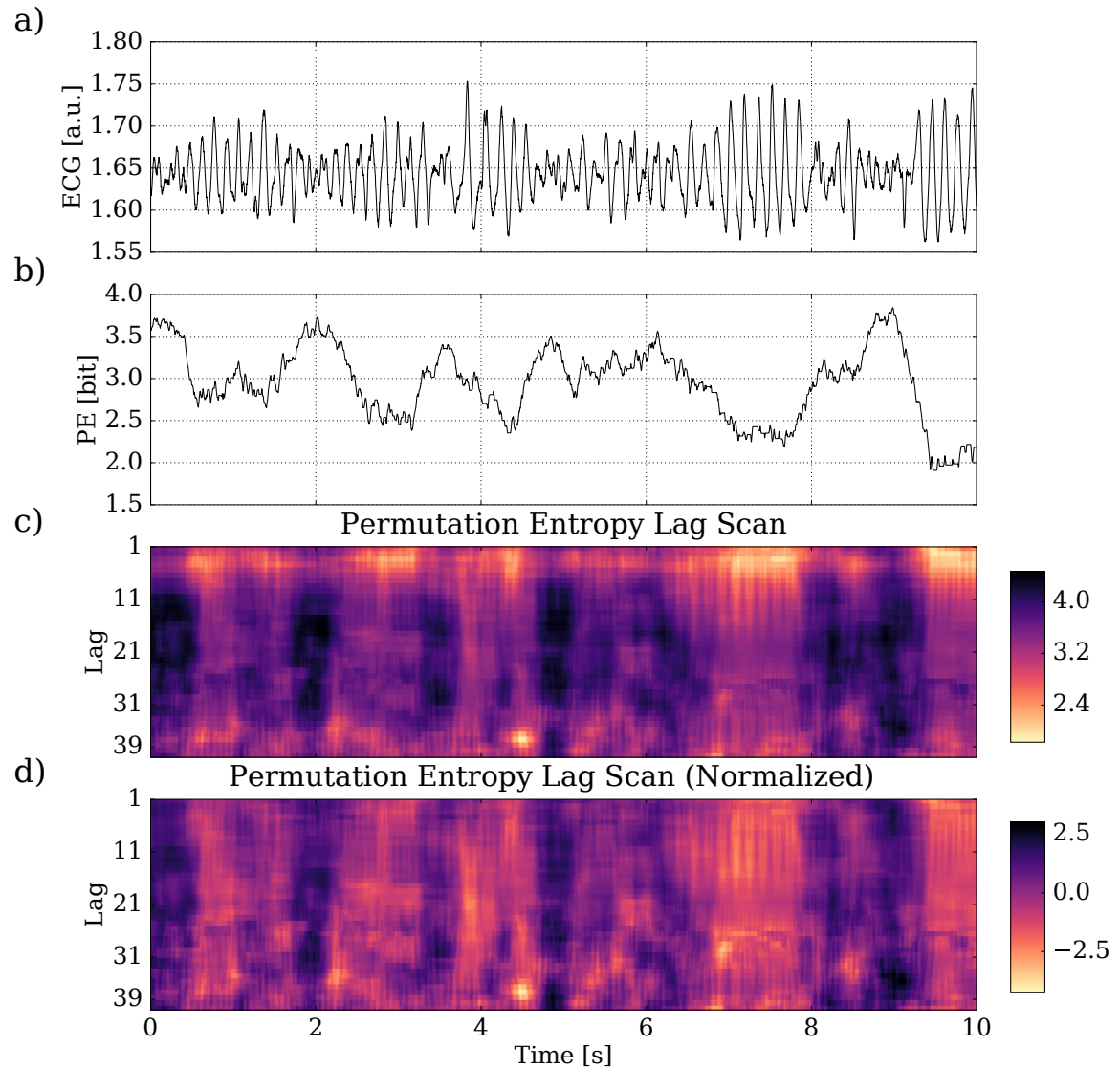


Figure 3.16.: Details of the application of the PE to the VF time series of a rabbit heart. a) shows the ECG time series. b) The time series of the PE for $L = 2$ (4ms). c) The PE lag scan shows the PE time series for different lags L . d) The normalized lag scan shows the same information as c), but with each row being normalized by mean and standard deviation as explained in the text.

3.3. Quantification of Complexity Fluctuations in the ECG

Furthermore, the general increase in complexity values towards the maximum of $PE \approx 4.58$ could imply more sensitivity to noise, because a signal only comprised of noise produces the maximum value for PE (see also the appendix, Sec. A.3).

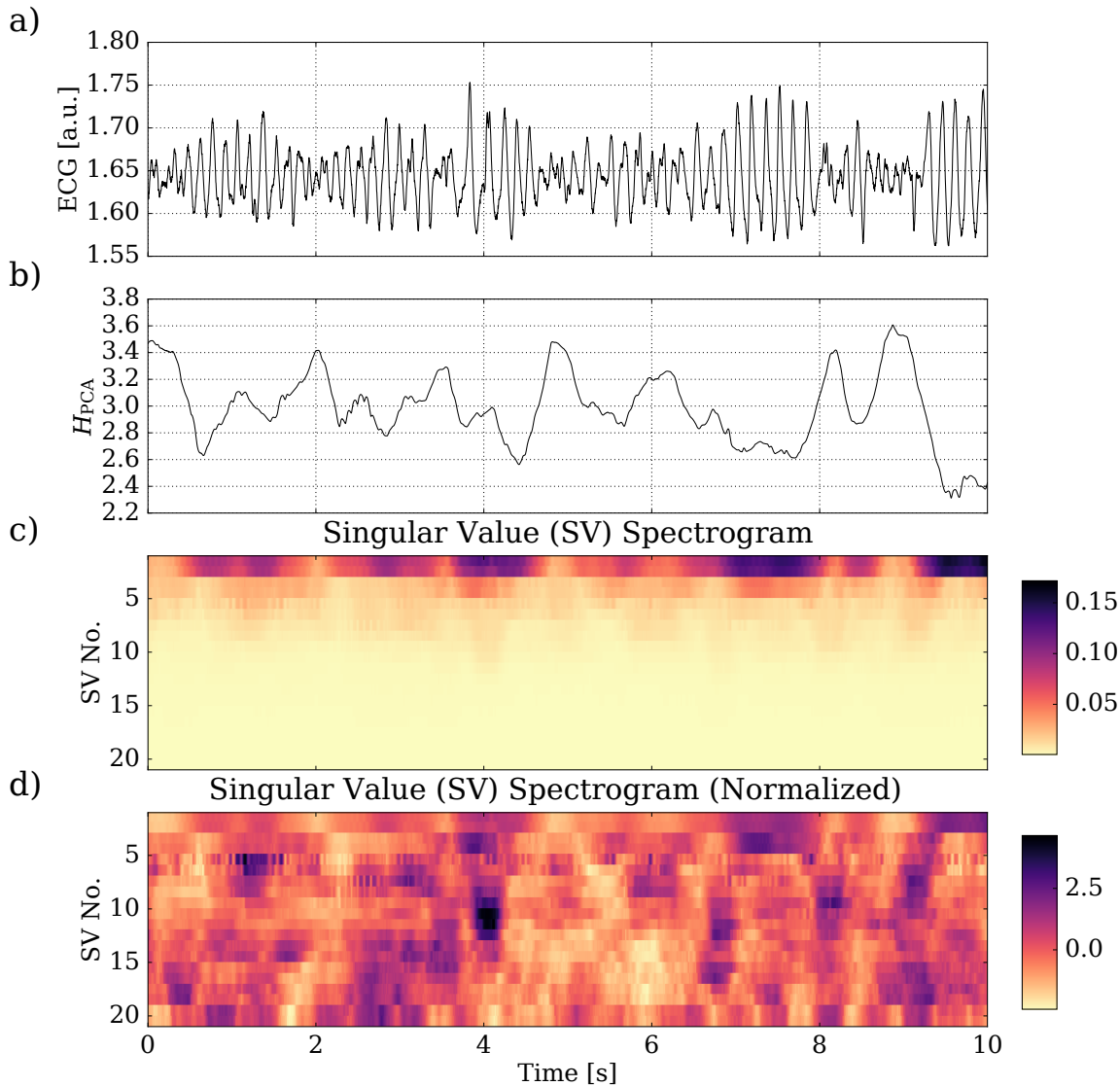


Figure 3.17.: Example of an application of H_{PCA} to the same time series which was used in Fig. 3.16. a) shows the ECG excerpt. b) Shows H_{PCA} , c) displays time series of the singular values of the corresponding SVD and d) shows the same information as c), but with each row being normalized by mean and standard deviation of the respective row.

Therefore a fixation of the PE lag parameter to $L = 2$ is plausible (If not noted otherwise

3. Results

this value for L will be used in all computations for PE here). This is not intuitive when interpreting permutation entropy with the theory of attractor reconstruction in mind, because the order patterns are much shorter than it would be expected for a reasonable attractor reconstruction. In the context of ECG complexity in this thesis, these order patterns are interpreted as a quantification of specific patterns in the ECG time series. These specific patterns will be discussed in more detail in Sec. 3.3.7.

3.3.2. PCA Entropy

Fig. 3.17 shows results computed for another measure described in Sec. 2.1.2 which is called PCA entropy H_{PCA} here (Eq. 2.20). This measure has an intuitive interpretation as variation of the extent of the space spanned by the reconstructed states of the time series: White noise shows the highest PCA entropy, as all directions of the space of reconstructed states have a very similar extent which is directly reflected by the singular values of the SVD. On the other hand, the reconstructed states of simple periodic signals have a significant extent only in a few directions which leads to a low value for H_{PCA} . This effect is demonstrated in the appendix in Sec. A.3.

There are two parameters for the PCA entropy, the embedding dimension D and the embedding delay L . For the application of the method to VF time series it is important to use an embedding dimension $D > 2$, because differences in the attractor dimension of sine-like signals and more chaotic time series have to be resolved. The lag parameter L of H_{PCA} can be simply set to very small values if the embedding dimension is sufficiently high. In fact the original definition of Broomhead-King coordinates does not include this parameter. Reasonable values for L can also be achieved using the auto correlation of the signal. H_{PCA} has been computed here with an embedding dimension of 20 and a time lag of $L = 4$ (8 ms).

This quantity reacts differently to fluctuations in the ECG than PE which is mainly visible in more variation and more peaks in H_{PCA} . It can be seen that the laminar phases at 0.65 s, 4.43 s, 7.0 s and 9.49 s are detected similarly to the PE in Sec. 3.3.1. In contrast to the PE, they do not appear as longer periods of low values of H_{PCA} , but more as simple peaks. An exception is the laminar phase at 7 s which remains at lower values for almost one second. H_{PCA} seems to be able to detect very short periods of low complexity as can be seen at 8.5 s, a low complexity spike in the ECG which is not highlighted by the PE. The general property of H_{PCA} to react quicker to irregularities in the signal is also shown in Sec. A.3 for artificial signals.

3.3.3. Wavelets

The third quantity which will be discussed in detail here is the wavelet energy E_{Wavelet} (Eq. 2.21) which is shown in Fig. 3.18. Fig. 3.18c shows a spectrogram which displays the sums of squared wavelet coefficients from Eq. 2.21 assigned to their scales p . This display is useful for identifying scales of interest as they can be matched to the signals seen in the time series of Fig. 3.18a. Fig. 3.18d is a normalized adaption of Fig. 3.18c which also highlights variations visible in scales which do not have an overall high amplitude.

Fig. 3.18c suggests that the coarse energy scales have a higher correspondence to the complexity of the ECG signal. This is also visible in Fig. 3.18b where two different energy bands are plotted in black and green color. The coarse scales show a very distinct increase for periods of low complexity, especially for the major ones at 7s and 9.49s. But here also the minor periods of lower complexity seem to be detected well. Higher amplitudes of the low complexity periods can be associated with higher energy.

The next section will continue with a more systematic comparison of these and some additional methods among each other for identifying similarities and differences.

3. Results

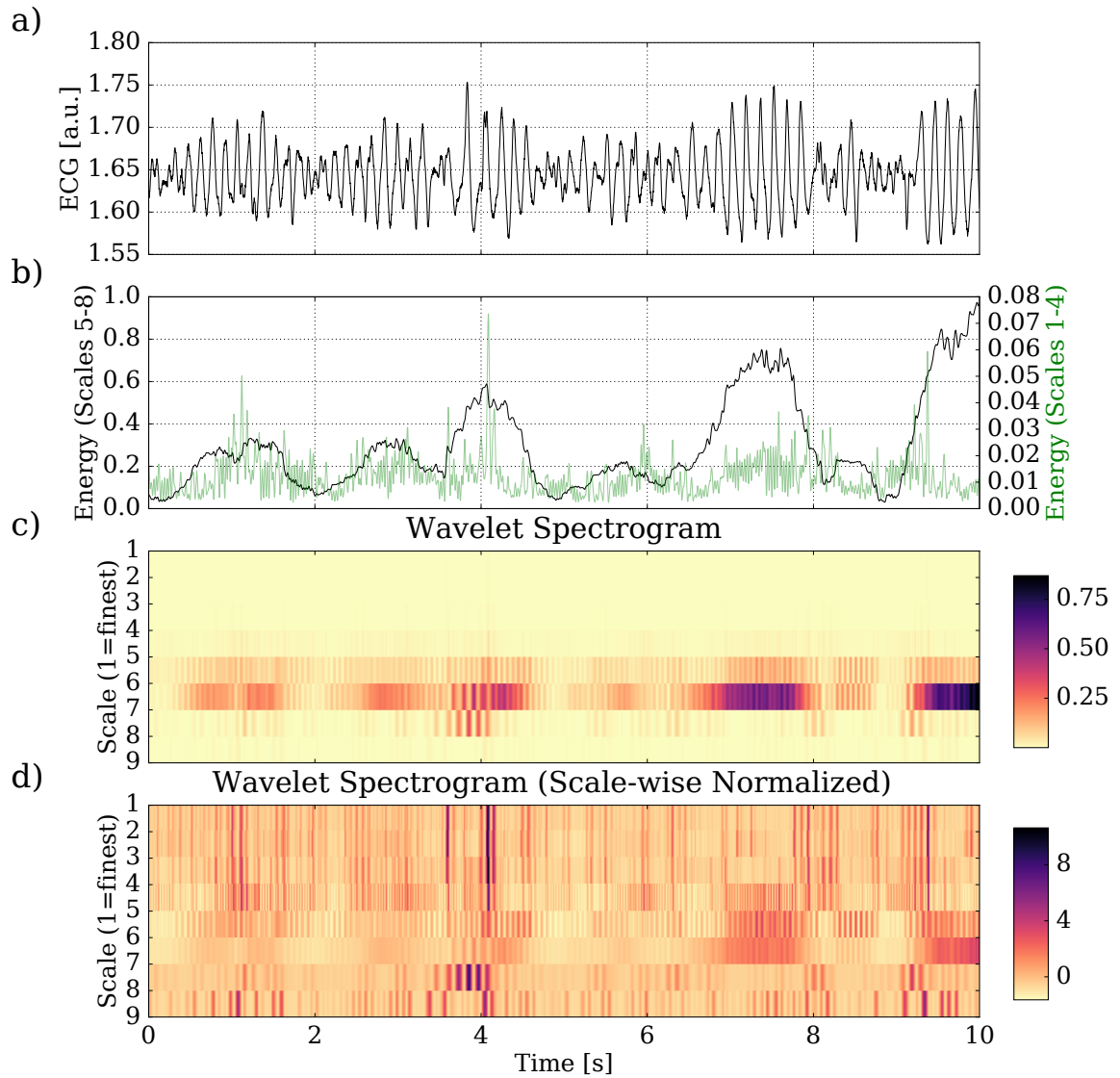


Figure 3.18.: Results for the application of the wavelet energy to ECG time series of a rabbit heart VF. a) The same ECG time series as in Fig. 3.17. b) Wavelet energies for two bands, scales 5 to 8 in black and scales 1 to 4 in light green color. c) The wavelet spectrogram which shows the contributions of the individual energy bands to the total energy. d) A normalized version of c) which allows for an identification of changes within each energy band. Rows are normalized by mean and standard deviation of the respective energy bands.

3.3.4. Comparison of Complexity Measures for the ECG

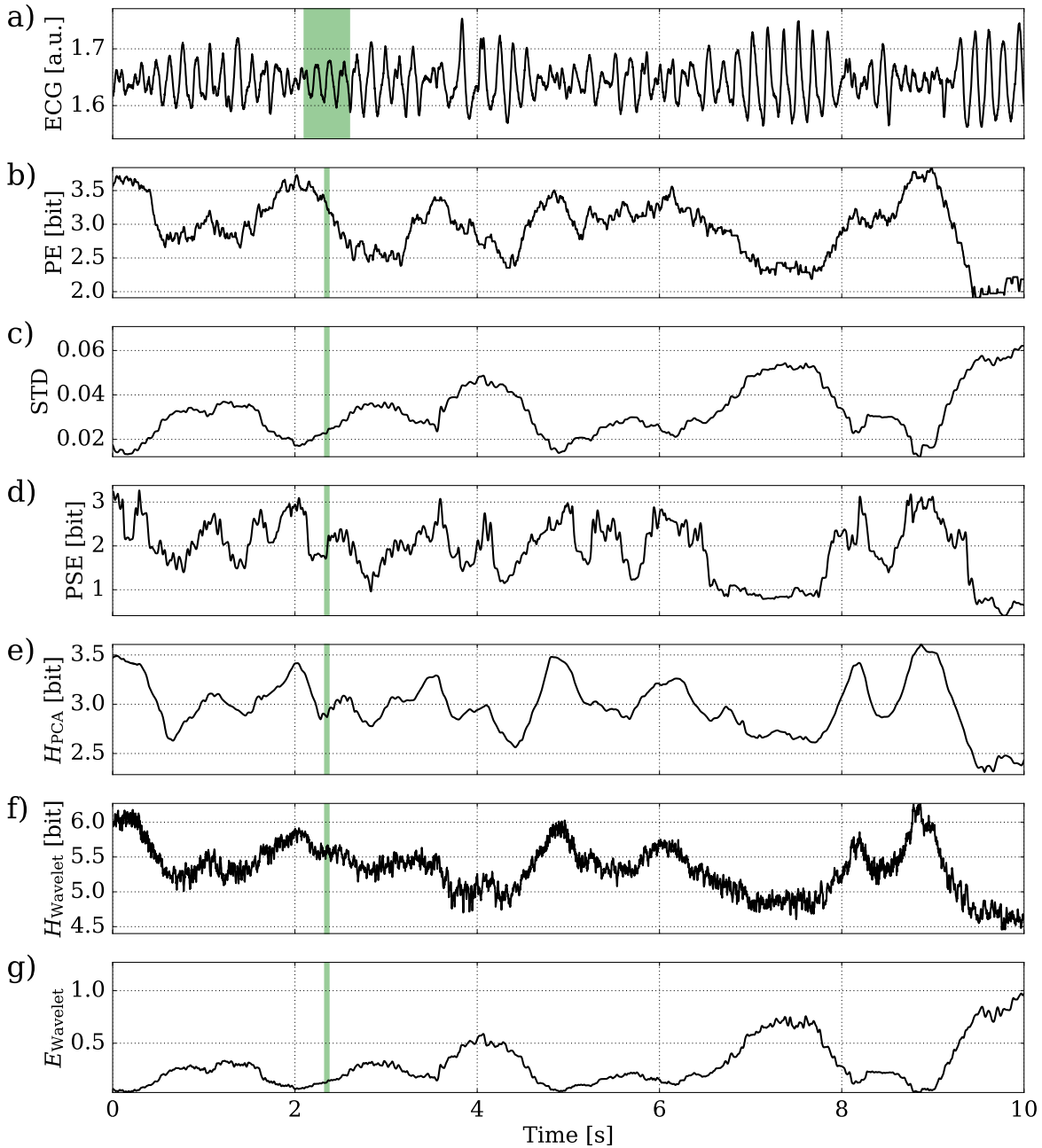


Figure 3.19.: An overview over ECG complexity measures applied to an ECG of a rabbit heart VF: a) The ECG b) Permutation Entropy (PE) c) Windowed Standard Deviation (STD) d) Power Spectral Entropy (PSE) e) PCA Entropy H_{PCA} f) Wavelet Entropy $H_{Wavelet}$ g) Wavelet Energy for the coarse energy scales $p \in [5, 8]$

3. Results

The ECG complexity methods discussed in the previous sections show similarities, so pairwise correlations are discussed in this section. Fig. 3.19 gives an overview over all the ECG complexity methods used here for an excerpt of a VF of a rabbit heart which has been recorded on 2016-02-19¹³. The figure contains all the measures discussed in Sec. 3.3.1-Sec. 3.3.3 and in addition the PSE (see Sec. 2.1.4), the windowed standard deviation (STD, see Sec. 2.1.3) and H_{Wavelet} (see Sec. 2.1.5). The figure suggests that the major laminar phases are associated with a significant increase (decrease in case of STD and E_{Wavelet}) in the respective quantity. The time series of STD and E_{Wavelet} are multiplied by -1 before computing the correlations to allow for an easier comparison. The PSE fluctuates much more than the other quantities and does not seem to be well-suited for the detection of short laminar phases. This is probably due to the very limited frequency resolution of the FFT of only 2 Hz.

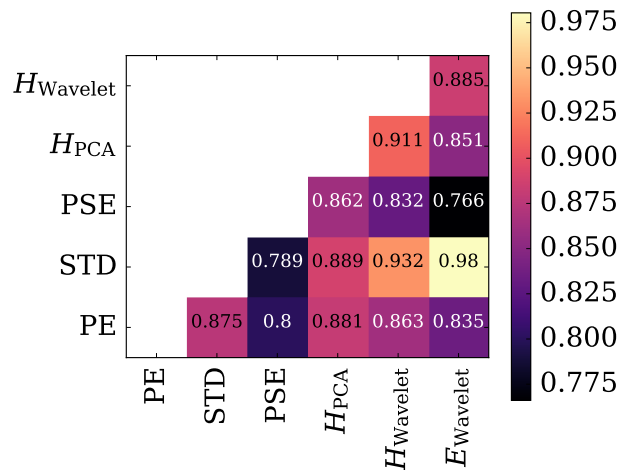


Figure 3.20.: Correlation matrix for the full time series until the shock of the dataset visible in Fig. 3.19. The time series of STD and E_{Wavelet} are multiplied by -1 before computing the correlations.

Fig. 3.20 shows the correlation matrix for all the methods shown in Fig. 3.19. This figure confirms in a quantitative way that the PSE seems to contain different information than most other measures, as its correlations to other measures are the lowest. It can be seen that the wavelet quantities have a very high correlation to the windowed standard deviation (STD). This implies that amplitude information plays a major role for this type of complexity analysis.

¹³Experiment: ID 32, 2016-02-19, pulsar recordings 161201

3.3. Quantification of Complexity Fluctuations in the ECG

It is not a surprise that all of the quantities show a high correlation to STD, because the laminar phases are often accompanied by a strong change in amplitude. However, as it was already pointed out, it is not desirable to rely on that feature for robust detection of complexity fluctuations.

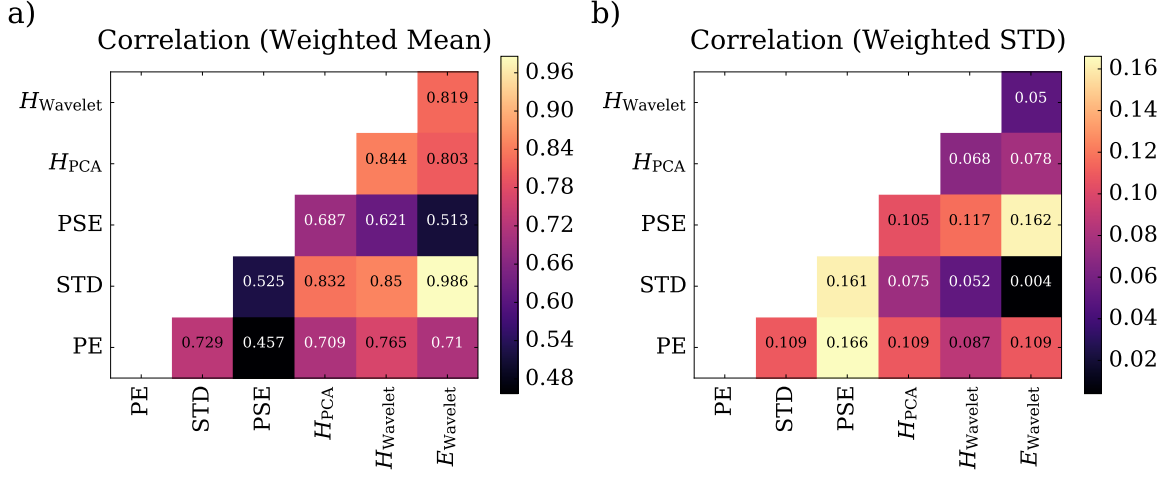


Figure 3.21.: Weighted mean and weighted standard deviation of all correlation matrices computed for all 58 time series of 2016-02-19 using the length of the respective time series as the weight (normalized by the sum of all lengths). The time series of STD and $E_{Wavelet}$ are multiplied by -1 before computing the correlations.

To show that these results are qualitatively stable when generalized to a larger sample, all measures have been applied to two complete datasets of rabbit ex vivo experiments. These datasets belong to the series described in Sec. 3.2 and were acquired on 2016-02-19 and 2016-02-29. All time series belonging to entropy pacing shocks have been used, because they contain time series which are long enough for this analysis. The time series used here start when the shock protocol was initiated and end 0.25s before the first shock. The total length of all time series used is 488 s for 2016-02-19 and 337 s for 2016-02-29.

Weighted mean (Eq. 2.30) and standard deviation (Eq. 2.31) of the correlation matrices calculated for all time series of the dataset from 2016-02-19 are plotted in Fig. 3.22. The relative lengths of the time series are used as weights, such that longer time series contribute more to the mean than shorter time series. It can be seen that the pattern visible in the correlation matrix is very similar to the correlation matrix of the single dataset. The correlations with the PSE have decreased quite heavily to a minimum of 0.46 between PE and PSE. Most pairwise correlations have decreased by approximately 0.1 compared to the correlation matrix of the single dataset. The high correlation between STD and $E_{Wavelet}$ has almost stayed constant which consolidates that most

3. Results

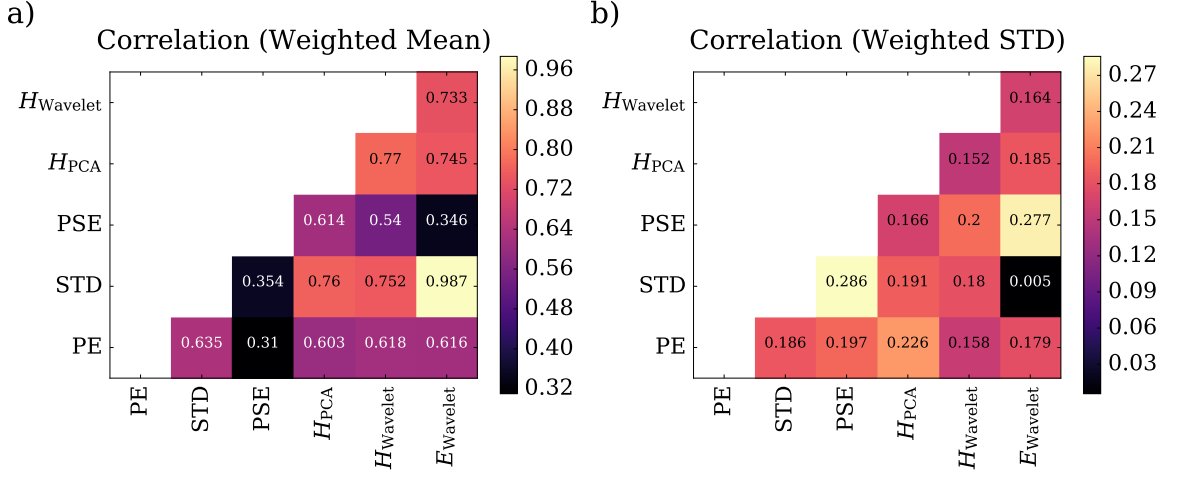


Figure 3.22.: Weighted mean and weighted standard deviation of all correlation matrices computed for all 28 time series of 2016-02-29 using the length of the respective time series as the weight (normalized by the sum of all lengths). The time series of STD and $E_{Wavelet}$ are multiplied by -1 before computing the correlations.

information for the wavelet energy at the coarse energy bands stems from the mere amplitude of the signal.

The analogous results for the second dataset which was measured on 2016-02-29 are shown in Fig. 3.22. In general, the structure of this correlation matrix is very similar to the one from the experiment on 2016-02-19. Two main differences are generally slightly lower correlations and slightly higher standard deviations.

The last dataset analysed in this subsection is the simulation dataset which is also used in Sec. 3.5. The set of 14 simulations which are listed in Tab. 3.7 was used. To not favor any specific ECG direction the pseudo ECG (PECG) explained in Sec. 2.3 was used to compute the complexity quantities.

In case of the simulations the true number of phase filaments (NFIL) is known and included in the analysis. Analogous to Sec. 3.5 it has been smoothed using a window of 250 frames. This is equal to the window length which is used for calculating the complexity measures.

Fig. 3.23 shows mean and standard deviation¹⁴ of the correlations for the simulation dataset. The correlations are in a similar range as in Fig. 3.22. The structure is also qualitatively the same. The correlation between $E_{Wavelet}$ and STD is very high. Most

¹⁴Weighting is not necessary here, because all simulation time series used here have the same length.

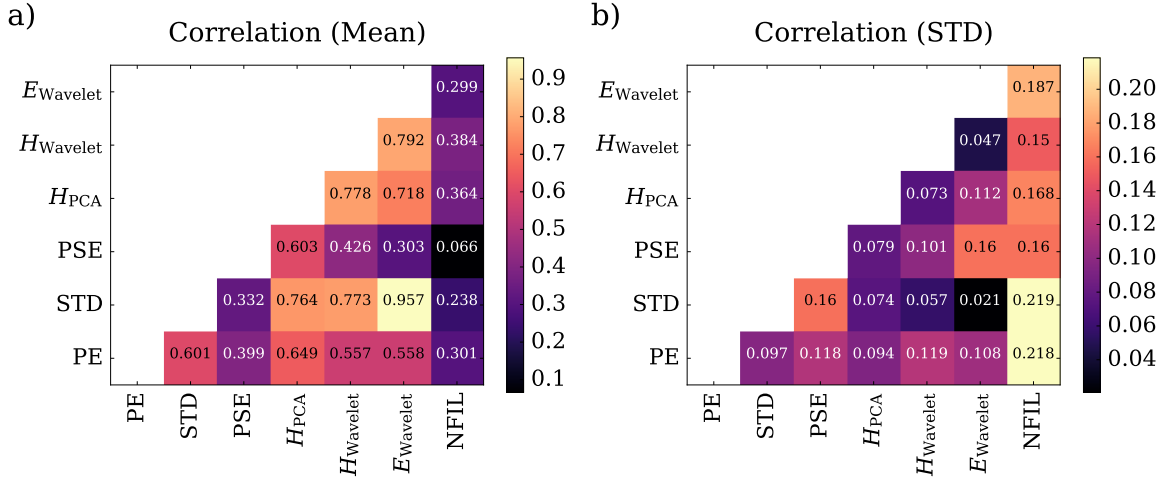


Figure 3.23.: Mean and standard deviation of all correlation matrices computed for all 14 pseudo ECG time series of simulation dataset. The time series of STD and $E_{Wavelet}$ are multiplied by -1 before computing the correlations.

correlations between PSE and other quantities are comparably low.

The correlations between the complexity measures of the ECG and NFIL are not high. This holds also for PE which shows much higher correlations to NFIL when it is calculated for the angle dependent realistic ECG (Eq. 2.27). These results are given in Sec. 3.5. Taking into account that the standard deviation of the correlations to NFIL are of a much higher order of magnitude than the differences among these values, there does not seem to be a favorable choice. The only exception is PSE with a relatively low correlation.

3.3.5. Machine Learning Analysis

Data from the experiments described in Sec. 3.2 can be used to carry out a machine learning analysis which tries to estimate the prediction error for predicting the outcome of a shock by using different complexity measures. The outcome of the shock is the success of the defibrillation. Many different sets of features could be used to try the prediction, but here the analysis will be limited to three different feature sets, as trying many feature sets can lead to serious overfitting effects that will overestimate the quality of prediction [43]. The number of data points per Experiment is extremely low (see Sec. 3.2), so this machine learning task can be considered very difficult and no reasonable performance of the classifier can be expected.

The following features described in Sec. 2.1 will be used. These have been compared in

3. Results

Sec. 3.3.4:

- Permutation entropy (PE) computed from Eq. 2.4
- Windowed standard deviation (STD) computed from Eq. 2.12
- Wavelet entropy computed from Eq. 2.20
- Wavelet energy of the coarse energy band computed from Eq. 2.21
- Power spectral entropy (PSE) computed from Eq. 2.13
- PCA Entropy computed from Eq. 2.10

I will refer to this set of features as F_1 .

Although the experimental procedure was designed in a way that laminar phases and complex phases are tested with equal frequencies, there might be some inequality, because shocks failed in some cases or it was not possible to deliver additional shocks. This might lead to an imbalance in trials per energy per complexity phase which could lead to an influence of the shock energy on the predictive power of specific features. In order to investigate this possible effect, a second feature set F_2 includes all the complexity features mentioned above and additionally the shock amplitude.

As a third possible factor of influence the dominant frequency (DF) of the signal is estimated and integrated additionally to the complexity features and the shock amplitude into F_3 .

The complexity features are computed for half a second before the shock from the ECG. For the classification task a random forest with 200 trees has been used. This random forest is applied using a 10-fold cross validation. This cross validation itself is applied 50 times to the real datasets, so that it is possible to detect unwanted variations from the random subset generation process. Additionally the same cross validation is applied to 200 copies of the original datasets with shuffled class labels in order to estimate the surrogate performance. These surrogates are used to obtain the given p -values. The p -value is the fraction of surrogates which is greater or equal than the real MCC. The quality of the classifications itself is quantified using the MCC (Eq. 2.40).

3.3. Quantification of Complexity Fluctuations in the ECG

MCC (F_1)	p (F_1)	MCC (F_2)	p (F_2)	MCC (F_3)	p (F_3)
2016-02-19 / Rabbit Ex Vivo					
0.26	0.1	0.33	0.08	0.3	0.09
2016-02-29 / Rabbit Ex Vivo					
-0.25	0.68	-0.03	0.41	-0.02	0.42
2016-03-09 / Rabbit Ex Vivo					
-0.28	0.74	0.04	0.3	0.0	0.34
2016-02-24 / Pig Ex Vivo¹⁵					
-0.09	0.45	-0.1	0.47	-0.1	0.48
2016-02-25 / Pig Ex Vivo					
-0.33	0.9	0.11	0.23	0.16	0.2
2016-02-26 / Pig Ex Vivo					
0.25	0.05	0.54	0.0	0.56	0.0

Table 3.2.: Machine learning results. The MCC has been calculated according to Eq. 2.40.

Tab. 3.3 lists the results obtained for the machine learning analysis. It is immediately visible that a classification under cross validation conditions gave $MCC > 0$ only for the ex vivo experiments on 2016-02-19 and 2016-02-26. However, the results are not significant. Including the energy into the feature set increased the classifier performance in both cases. Adding the dominant frequencies did only change the results slightly. For all other datasets a classification using the proposed feature sets did not work well and did not show any significant outcomes.

¹⁵This dataset lead to a significant number of cases in which the MCC became NaN due to models that predicted only one class in the cross validation. The MCCs shown here are the mean of the remaining cases for completeness.

3. Results

As described in the methods section (Sec. 2.6.4) tree classifiers and random forest classifiers have the advantage that feature importances measuring the amount of contribution of individual features from the feature set are directly accessible. Tab. 3.3 displays the feature importance results for the two experiments for which a classification yielded MCCs greater than zero. Overall the importances do not differ very much. There seems to be a slight advantage of using the PE for the results from 2016-02-19. On 2016-02-26, amplitude and dominant frequency seem to be the most important predictors while the complexity features seem to play only a minor role.

Feature set	PE	STD	E_{Wavelet}	H_{Wavelet}	H_{PCA}	PSE	A	DF
2016-02-19 / Rabbit Ex Vivo								
F_1	0.25	0.17	0.13	0.17	0.13	0.16		
F_2	0.2	0.13	0.11	0.13	0.11	0.13	0.18	
F_3	0.18	0.13	0.1	0.13	0.11	0.12	0.17	0.07
2016-02-26 / Pig Ex Vivo								
F_1	0.18	0.19	0.17	0.17	0.13	0.16		
F_2	0.13	0.12	0.12	0.11	0.08	0.1	0.33	
F_3	0.11	0.09	0.09	0.08	0.07	0.08	0.25	0.22

Table 3.3.: Results of the importances for two of the experiments where a positive MCC could be achieved. The feature importances indicate which features were the most useful ones during building of the random forest models. F_1 , F_2 and F_3 refer to the three feature sets explained in Sec. 3.3.5.

3.3.6. Descriptive Statistics for Complexity Fluctuations

In this section statistical properties of the complexity fluctuations are analysed. The statistical properties of laminar phases are very important for the design of experiments. Therefore approximate numbers and durations of laminar phases are given by assuming a threshold based on mean and standard deviation of the PE.

3.3. Quantification of Complexity Fluctuations in the ECG

Tab. 3.4 lists the results for this analysis. PE_{mean} and PE_{std} are the mean and standard deviation of the PE computed from all entropy pacing time series of the respective experiment before the first shock. For the other columns in the table all PE values below $PE_{\text{mean}} - PE_{\text{std}}$ were considered a laminar phase. N is the total number of laminar phases in the dataset and n is the number of laminar phases per second. $n_{>0.5\text{ s}}$ and $n_{>0.25\text{ s}}$ are the numbers of laminar phases per second that are longer than 0.5 s and 0.25 s. t_{mean} and t_{std} give the mean and standard deviation of the durations of all laminar phases in the dataset.

Date	PE_{mean}	PE_{std}	N	n	$n_{>0.5\text{ s}}$	$n_{>0.25\text{ s}}$	t_{mean}	t_{std}
Rabbit								
2016-02-19	3.09	0.47	539	1.11	0.1	0.23	0.16	0.27
2016-02-29	2.61	0.5	312	0.93	0.08	0.14	0.19	0.65
2016-03-09	3.33	0.44	688	1.12	0.08	0.18	0.15	0.28
Fig								
2016-02-24	2.84	0.52	367	1.05	0.1	0.16	0.17	0.47
2016-02-25	3.4	0.52	802	1.0	0.11	0.22	0.18	0.39
2016-02-26	2.57	0.41	1265	1.63	0.08	0.2	0.1	0.19

Table 3.4.: Summary table of the descriptive results for the laminar phases. The quantities listed here are explained in Sec. 3.3.6.

The mean PE seems to vary quite a lot between the datasets. This can stem from differences in the electrode configuration and different levels of noise. The standard deviation of the PE is always around 0.5. This knowledge can facilitate the experimental settings as only one parameter has to be calibrated. Histograms of the PE are given in the appendix in Fig. A.1, Fig. A.2 and Fig. A.3.

Tab. 3.4 shows that there is in most cases approximately one laminar phase per second. About one tenth out of them is longer than half a second.

3.3.7. Algorithm for Detection of Laminar Phases

For technical applications the design of an efficient algorithm for detecting laminar phases is desirable. Two questions drove the analysis presented in this section:

- Can specific order patterns in the ECG be used to identify a laminar phase?
- How can the threshold for a laminar phase be calibrated reliably?

In the previous sections the threshold for separating a laminar phase from a more com-

3. Results

plex phase have been derived from the distribution of complexity quantities. As it was described in the previous sections, several factors can possibly influence the distribution of complexity values. The most prominent ones are:

1. Varying levels of noise
2. Changes in the positions of the ECG electrodes
3. Anatomical differences of the hearts between and among species
4. Drug administration

While factor 1 has mostly been identified to cause an offset in the PE distribution (see Sec. A.3) the effects of the other factors seem to be more subtle. 2 has not been considered a problem for the datasets analysed so far, as laminar phases were visible regardless of slight changes in the ECG characteristics. The effect of changes in the positions of ECG electrodes is discussed in Sec. 3.5 using data from simulations. The effects of 3 and 4 can be associated with major differences in VF frequency and the maximum number of rotors on the heart. The dominant frequency of the VF varies between species and can be influenced by specific drugs. There is less space for spiral waves on small hearts than on larger hearts which usually leads to a higher variety in the dominant frequency and a generally more complex ECG on bigger hearts.

The algorithm presented here is based on the observation that the difference between PE during laminar phases and PE during more complex phases is mainly caused by a major increase in relative frequencies of two specific order patterns. PE allows for an inspection of the specific order patterns involved in the computation.

The problem of calibrating the threshold of the detection algorithm is handled by a comparison with a sine of suitable frequency.

Fig. 3.24 shows a 20s excerpt of an ECG of a rabbit heart during VF¹⁶ along with its PE time series and the order pattern statistics. It clearly indicates that the most important features to consider for fluctuations are related to permutation indices 0 and 23 which belong to symbols with only increasing or only decreasing values (see Fig. 2.2 for visual representations). That suggests that using a simple statistic for these two patterns should be sufficient for the detection of low complexity periods.

Fig. 3.25 confirms that the PE and the negative sum of the relative frequencies of these two permutation indices show an extremely high correlation of $C = 0.99$. Therefore the

¹⁶Experiment: ID 6, 2016-02-19, pulsar recordings 143342

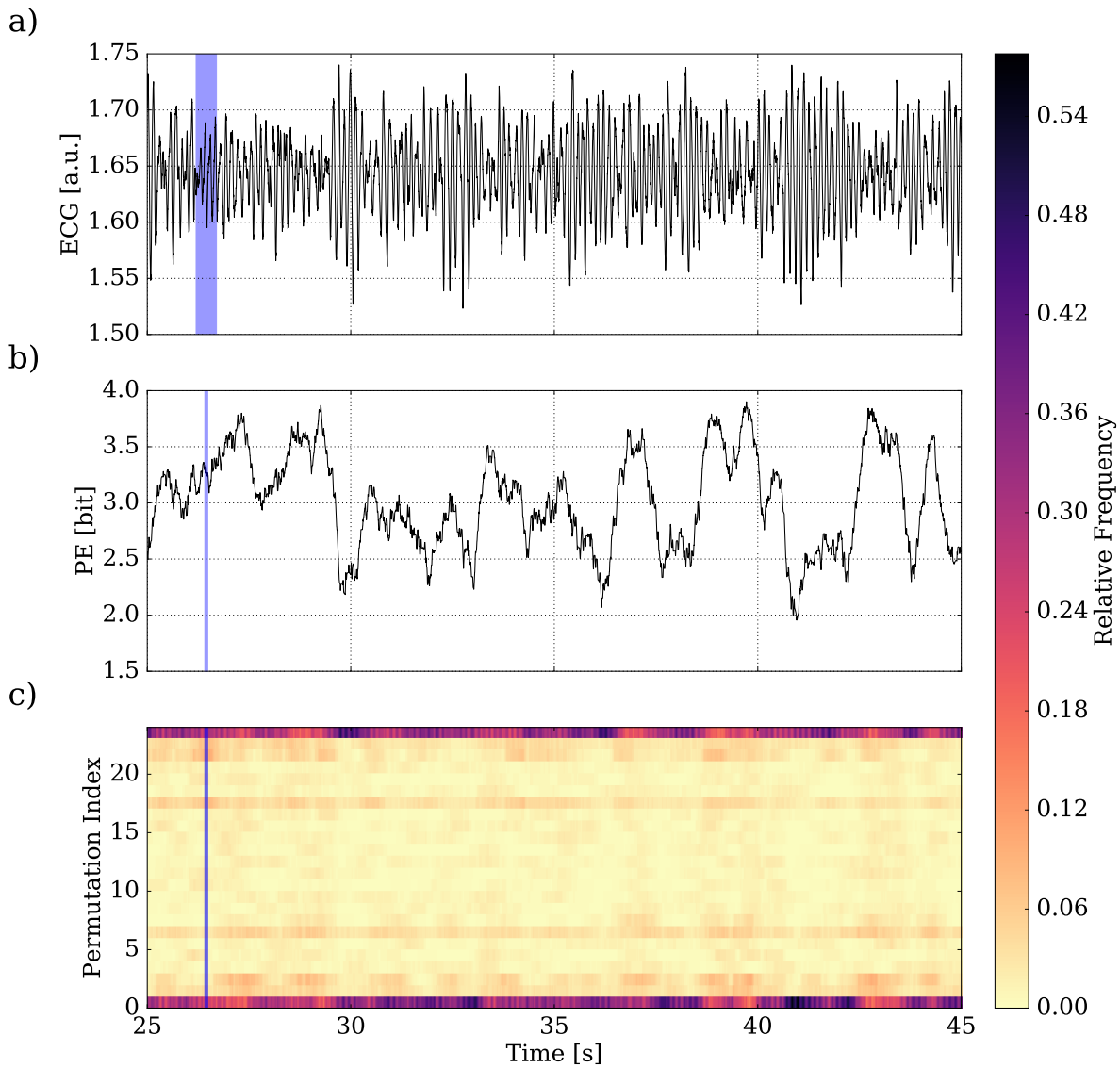


Figure 3.24.: A 20s excerpt of an ECG during the VF of a rabbit heart starting 25s after the onset of VF. In addition to the ECG shown in a) and the PE shown in b) the plain order pattern statistics is shown in c). The vertical axis corresponds to the permutation index. Refer to Fig. 2.2 for visual representations of the respective patterns.

3. Results

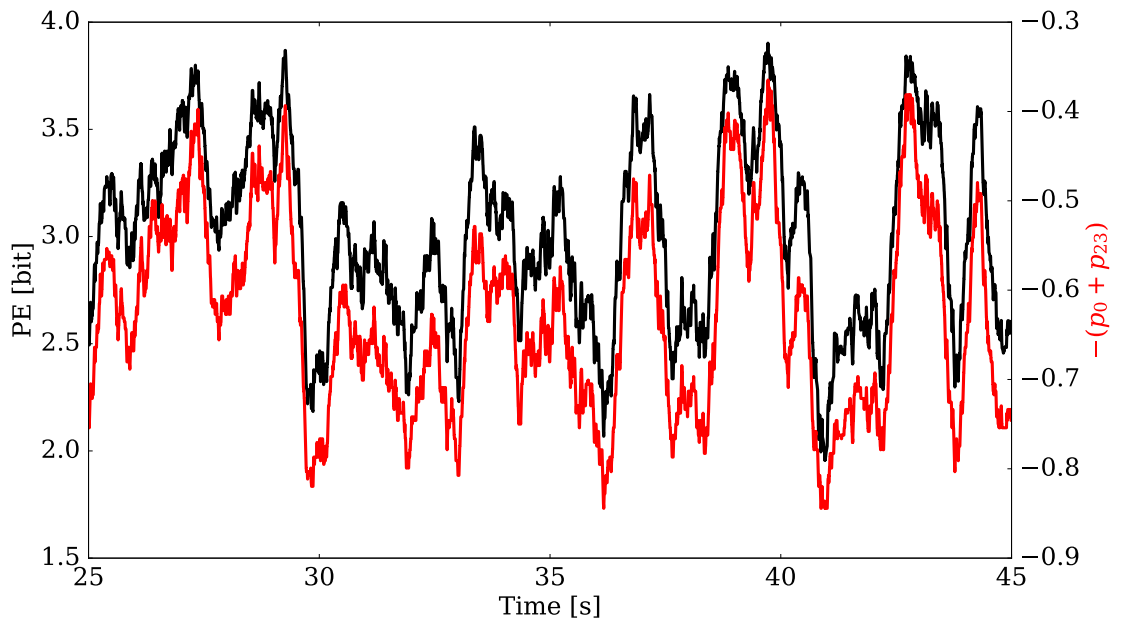


Figure 3.25.: Comparison PE of Fig. 3.24 (black) and the negative sum of the relative frequencies for permutation index 0 (p_0) and permutation index 23 (p_{23}). The correlation coefficient of these quantities is $C = 0.99$.

quantity

$$P(t) := -(p_0(t) + p_{23}(t)) \quad (3.3)$$

with $p_i(t)$ being the relative frequency of permutation index i at time step t will be used for the construction of the algorithm for detecting laminar phases in the ECG.

As mentioned earlier a reasonable approach for determining the threshold for laminar phases is to use a reference sine with the correct frequency. This approach estimates the dominant frequency of the ECG signal and generates a sine signal with the same frequency. Afterwards $P_{\text{ref}}(t)$ as defined in Eq. 3.3 can be computed for this reference signal and compared to $P(t)$ computed for the ECG. One additional prefiltering step is necessary to be able to compare the features derived from the ECG signal to the reference signal: Because there is also noise contained in the laminar phases of the ECG, $P(t)$ will probably never reach the threshold defined by $P_{\text{ref}}(t)$. To handle this issue it would be either possible to add artificial noise to the reference signal or to remove small-timescale fluctuations from the ECG. As it can be considered more difficult to estimate the signal to noise ratio which is essential for the former approach, Butterworth bandpass filtering is applied to the ECG signal before the computation. The frequency range for this procedure is set to 0.5s to 25s which is a sensible range for VF signals.

Fig. 3.27 shows a 5s excerpt of the ECG time series shown in Fig. 3.25. The reference

3.3. Quantification of Complexity Fluctuations in the ECG

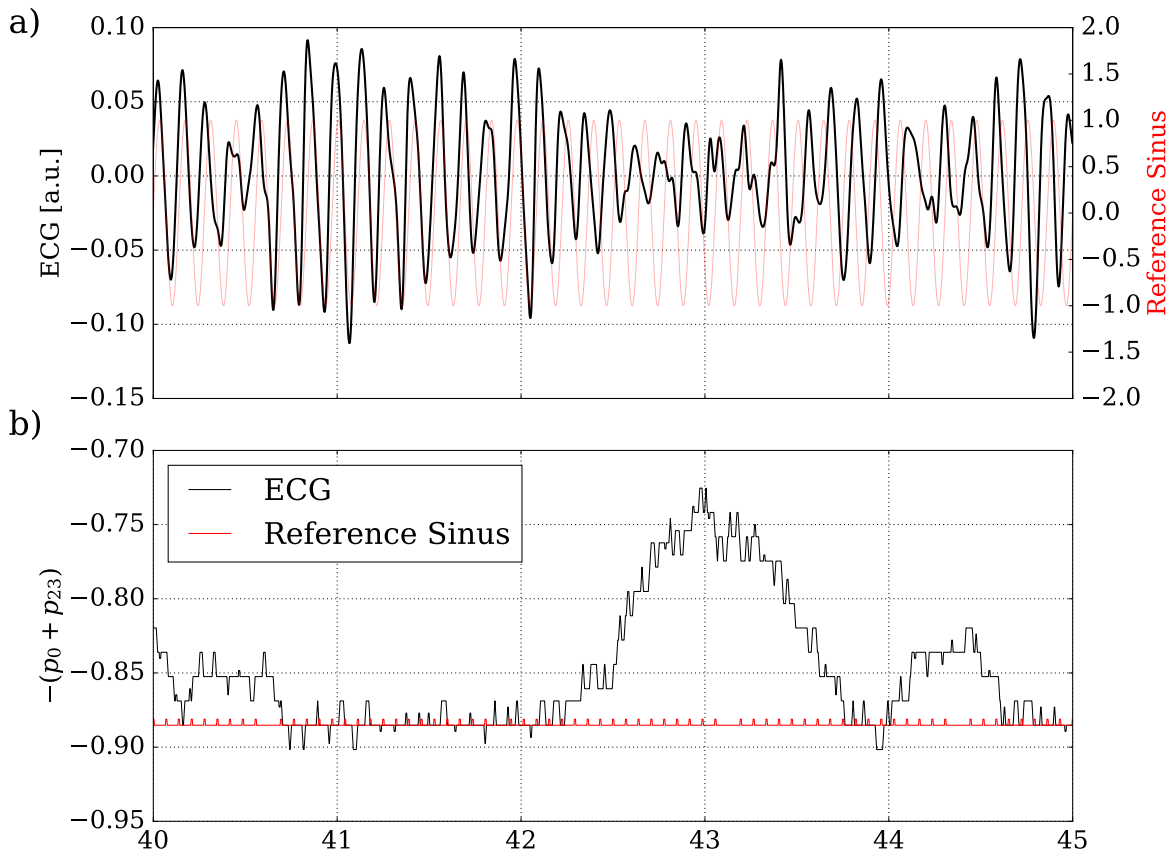


Figure 3.26.: $P(t)$ and $P_{\text{ref}}(t)$ computed for a short excerpt of a rabbit heart VF and the corresponding reference sine signal.

3. Results

sine is shown in Fig. 3.27a in the background. The dominant frequency of the VF signal has been used to estimate the frequency of the reference signal. In Fig. 3.27b the two time series $P(t)$ (black) and the reference $P_{\text{ref}}(t)$ (red) are displayed. The figure clearly indicates that during the laminar phases, for example between 40.6s and 42.6s, $P(t)$ attains values very close to $P_{\text{ref}}(t)$.

Detection of Laminar Phases

The considerations made here lead to the following algorithm. The term “monotonous order pattern” will be used for order patterns of length four with permutation index 0 or 23.

1. Apply bandpass filtering to the ECG signal.
2. Determine the laminarity threshold:
 - a) Estimate the dominant frequency from the ECG signal.
 - b) Generate the reference sine signal using the dominant frequency.
 - c) Count the number of monotonous order patterns divide it by the total number of order patterns in the reference signal. This quotient defines the threshold h .
3. For each time t in the ECG time series detect whether it is the beginning of a monotonous order pattern. Generate a binary time series displaying a 1 when this is the case and a 0 otherwise.
4. Convolve this binary time series with a boxcar kernel with the desired window length. This creates a time series which gives the fraction of monotonous order patterns per window length.
5. The times when the ECG is detected as laminar (called laminar points here) can be identified as the points where the convolution from the previous step is larger or equal to the threshold h .

It makes sense to smooth the laminar points which are identified by this procedure slightly with a running mean filter, because $P(t)$ fluctuates slightly around the threshold during laminar phases as it was seen in Fig. 3.27, but connected segments of laminar phases are desirable. This smoothed time series will be called $s(t)$ here.

It is important to notice that the calibration with the sine signal transfers the problem

of estimating a threshold for the PE to the problem of estimating a reliable dominant frequency which is representative of the frequency during laminar phases which can be difficult in cases with broad or highly multimodal spectra. It also only works under the assumption that the frequency of the laminar phases does not fluctuate on short timescales. Of course extensions of this algorithm to make use of multiple reference signals with different frequencies are possible. Another approach to handle laminar phases with varying frequencies could be an adaptive measurement of the dominant frequency. As a general rule the relative frequencies p_0 and p_{23} decrease when increasing the frequency of the reference signal. Therefore, to increase sensitivity of the algorithm higher frequencies should be preferred in case of multiple distinct peaks in the spectrum. In case of very rare occurrence of laminar phases it is very unlikely that the correct frequency can be determined in an automatic manner using standard frequency detection methods and predefined frequencies based on previous knowledge about the experiment should be used. An investigation of the effect of the window length on the results of this algorithm is found in Sec. A.4.

Application of the Algorithm to a Rabbit VF

An application of the algorithm is shown in Fig. 3.27. The monotonous order patterns are identified with a lag of 2 frames. The bandpass filter for the ECG has a lower cutoff frequency of 0.5 Hz and an upper cutoff frequency of 25 Hz. The window length and the smoothing window length are set to 250 frames which equals 0.5 seconds. Segments in the ECG are highlighted where $s(t) > 0$.

It can be seen that many laminar phases are detected that visually match the criteria of a laminar phase. However also some differences to the visual inspection can be noted immediately:

- One short phase of higher complexity between 30.4 s and 30.8 s was detected as laminar. $s(t)$ is exceptionally low during this interval. This is probably the result of a quite long smoothing window and the very sharp criterion of $s(t) > 0$.
- The regular looking phase between 37 s and 38 s is not detected. This stems from a change in frequency during that period which is approximately 8 Hz instead of 7.2 Hz which is the dominant frequency of the ECG.

3.3.8. Summary and Conclusions

This section discussed measures for quantifying complexity of ECG signals and compared them using the correlation coefficient. The possibility to use these quantities in

3. Results

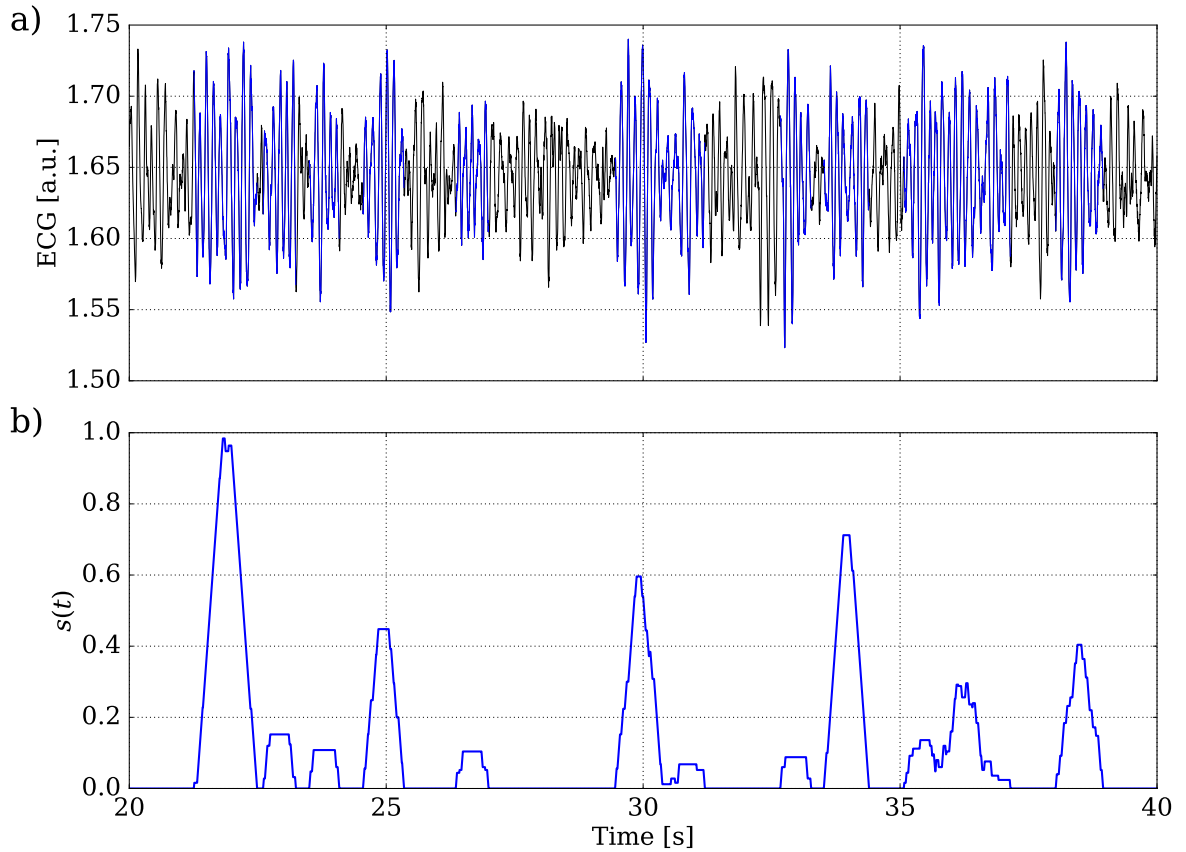


Figure 3.27.: a) ECG of a VF of a rabbit heart. The laminar phases which are detected are highlighted in blue. b) The smoothed time series of laminar points $s(t)$. A value of 1 indicates that all points inside the smoothing window have a value of $P(t)$ larger than the threshold given by the reference signal.

3.3. Quantification of Complexity Fluctuations in the ECG

a machine learning analysis was analysed using data from ex vivo experiments. Statistical properties of low complexity periods were analysed and an algorithm for detecting laminar phases efficiently was described.

- It can be concluded that the detection of complexity fluctuations is possible using multiple different complexity measures. Because laminar phases often have a higher amplitude than more complex phases, the windowed standard deviation of the ECG can already be used as a straight-forward indicator. However, other quantities can be much easier to interpret. Also robustness should be considered a major criterion and relying on mere amplitude information could be dangerous. The simple frequency distribution as measured by PSE seems not to be a good measure which is probably due to the small window length.
- Predicting the shock outcome using a short time segment before the shocks did not give good results. The amount of data needed for reliable analyses using machine learning methods is higher than currently available.
- The algorithm for detecting laminar phases described in Sec. 3.3.7 is able to detect laminar phases and does not rely on setting thresholds for the complexity quantity. Instead the problem of setting a complexity threshold is transferred to the problem of estimating a representative dominant frequency. Furthermore, the algorithm is very fast and can be applied to small window lengths. The logic required for its implementation is very simple which makes highly efficient technical applications feasible, such as usage in real-time systems. In case there is not a single dominant frequency or it is hard to estimate the application of this algorithm can become difficult. The approach of calibrating the threshold using a sine can also be transferred to other complexity measures.

3.4. Quantification of Spatiotemporal Complexity

During the ex vivo experiments with rabbit and pig hearts fluorescence activity on the surface is recorded by four cameras. These recordings can be analysed to understand the spatiotemporal complexity of arrhythmias and to investigate the processes governing their termination. The first part of this section describes a small series of experiments which was used to test a protocol for pacing dependent on the complexity measured from signals derived from the fluorescence images.

The focus of the analysis in the second part of this section is the question whether information from the camera signals can be used to understand complexity fluctuations in the ECG during VF. The application of measures for spatiotemporal complexity will be demonstrated on a dataset showing VF and complexity fluctuations in the ECG.

3.4.1. Entropy Camera Experiments

Two ex vivo experiments with rabbit hearts were conducted to investigate the possibility to use signals from multiple cameras to allow for a complexity-triggered intervention with a spatially resolved complexity measure. These experiments were designed and conducted together with Sebastian Berg.

In these experiments PE is computed for camera traces which is then used to define entropy regimes. The camera traces are averages over areas of the fluorescence signal (see Sec. 3.4.1). The four cameras of the perfusion experiment setup (see Sec. 3.2) record the fluorescence signal on the surface of the heart from different angles and are therefore able to capture different perspectives of the spatiotemporal dynamics.

Protocol

The experimental protocol was similar to the protocol described in Sec. 3.2:

- A pace-up¹⁷ protocol was used to estimate the defibrillation threshold for 10 monophasic pulses with overdrive pacing (using 0.9 times the cycle length for the cycle length of the pacing).
- Shocks were applied in a paired way for both regimes. For each pair, a coin toss

¹⁷This is done analogous to the procedure described in Sec. 3.2 by increasing the energy in steps of 20% until the first successful defibrillation is reached. This energy is then confirmed by decreasing and increasing the energy again at least one time.

determined whether the first shock should be into the high complexity or low complexity regime.

- Induction was carried out with 50 Hz far field pacing at 30 V.
- In case of a non-successful shock trial in the determined PE regime, a biphasic single shock at 80 V was used as a backup shock.
- Waiting time between the shock trials was at least 3 min.
- After the application of two shocks in different regimes the procedure was repeated and another coin-toss determined the next complexity regime.

For determining the dominant frequency of the VF the ECG was used.

Definition and Implementation of the PE Regimes

The camera software¹⁸ allows for the selection of an area of the image from which a trace can be extracted. The trace is then the average of the fluorescence signal within that defined region. This trace is send to the pacing software¹⁹. The pacing software then computes the PE from the camera traces and allows for triggering on defined PE regimes.

There is no ad hoc definition of complexity regimes for multiple signals. The following strategy was used, again making use of a threshold μ_i and a standard deviation σ_i which both are derived from the individual distributions of PE values for camera i :

- Low PE: $PE_i(t) < \mu_i - \sigma_i \forall i \in C$
- High PE: $PE_i(t) > \mu_i + \sigma_i \forall i \in C$

In this definition $PE_i(t)$ refers to the permutation entropy computed from the trace of camera i and C is the set of activated cameras. Activation and deactivation of cameras was implemented for the case that the camera signal of a specific camera could not be used reliably.

¹⁸MultiRecorder, see appendix, Sec. A.10.

¹⁹Pulsar, see appendix, Sec. A.10

3. Results

Amplitude	$N_{\text{Success}}^{\text{LowPE}}$	$N_{\text{No Success}}^{\text{LowPE}}$	Amplitude	$N_{\text{Success}}^{\text{LowPE}}$	$N_{\text{No Success}}^{\text{LowPE}}$
18 V	0	1	51 V	3	2
22 V	0	1	57 V	1	0
30 V	1	0	62 V	1	0
32 V	1	0	68 V	1	0
47 V	1	1	83 V	1	1

Table 3.5.: Results of the entropy camera experiment on 2016-09-05 for the condition “Low PE”. See Sec. 3.4.2 for details.

3.4.2. Results

On both days it was possible to induce VF, but only on the second day sustained VFs could be obtained. A good camera signal quality could be achieved. Due to technical problems with the calibration of the ECG amplifiers, the ECG signal was not always reliable. This resulted in some cases in very noisy ECG signals. As two ECGs were setup it was possible to switch the ECG channel in case of a corrupted signal.

First experiment day (2016-09-05)

It was not possible to induce sustained VFs on the first day, because self-terminations occurred frequently. Out of 116 entropy camera pacing attempts only 43 were marked as usable during the experiment. 62 of the 73 non usable attempts were not usable, because of a self-termination. Most of the remaining non usable attempts were VFs that changed into VT. Data analysis revealed that also all of the shock attempts in the “High PE” condition were also self-terminations just before the shock. As the signal after the self-termination yielded a high PE on all camera traces²⁰, shocks were initiated which lead in 100% of the cases to a re-induction of a VF. During the experiment this effect was not recognized, because the short period of termination was not visible during the conduction of the experiment. Solutions for handling problems like this in the future could include a separate detection of self-termination or a very strong noise-filter, although it has to be checked carefully whether these approaches are adequate for VF and do not corrupt necessary information.

For documentation purposes the results of the shocks given in the “Low PE” condition are given in Tab. 3.5.

On this day, no cryoablation zone was prepared on the rabbit heart. Induction of VFs in rabbit hearts can be highly facilitated by the use of a cryoablation zone.

²⁰The parameters for the PE in combination with the short window length of 0.5s are not suitable for detecting sinus rhythm. This usually leads to a high PE during sinus rhythm.

3.4. Quantification of Spatiotemporal Complexity

Amplitude	$N_{\text{Success}}^{\text{LowPE}}$	$N_{\text{No Success}}^{\text{LowPE}}$	$N_{\text{Success}}^{\text{HighPE}}$	$N_{\text{No Success}}^{\text{HighPE}}$	Cohen's h
26 V	0	2	0	2	0.0
29 V	1	1	0	1	1.57
29 V*	1	4	1	4	0.0
30 V	2	3	4	1	-0.84
32 V	1	0	1	0	0.0

Table 3.6.: Results of the entropy camera experiment on 2016-09-07 for both experimental conditions (“Low PE” and “High PE”). See Sec. 3.4.2 for details. The asterisk indicates a second series at 29 V done after recalibration of one camera (“Front Right”).

Second experiment day (2016-09-07)

On the second experimental day a cryoablation zone was used. Therefore induction of sustained VFs was reliably possible, but the heart became also ischemic. On this day the pace up protocol led to a defibrillation threshold of 26 V. Four unsuccessful defibrillation shocks (two into each regime) suggested an increase in voltage. Simultaneously it was observed that CL was estimated too high by the automatic CL detection algorithm which could have been caused by noise in the ECG signal. Using previous measurements of VFs on the same day the CL was therefore fixed to 0.116 s. The waiting time between the shock attempts was raised from 3 min to 5 min to make sure that the heart recovered as well as possible from the VF and shock procedure.

It was possible to acquire 29 data points (shown in Tab. 3.6) for the analysis with some changes during the course of the experiment:

- The second series done at 29 V which is marked with an asterisk in Tab. 3.6 was done after a recalibration of the field of view of camera “Front Right”. Furthermore after the third shock of this series camera “Front Left” had to be excluded due to bad signal.
- The last four shocks of the series at 30 V required multiple recalibrations of the PE margins.

One occurrence of an unsuccessful shock at 29 V into the low PE regime was observed which changed the VF into VT which terminated shortly afterwards.

As it is visible in Tab. 3.6 for the entries for 26 V and 29 V* there seems to be no clear difference in success probabilities between both regimes. The series at 30 V would rather indicate a higher success probability for the “High PE” regime. One experimental observation is that it is extremely difficult to calibrate the PE thresholds such that both regimes can be reached during the same period of VF. It was already described in

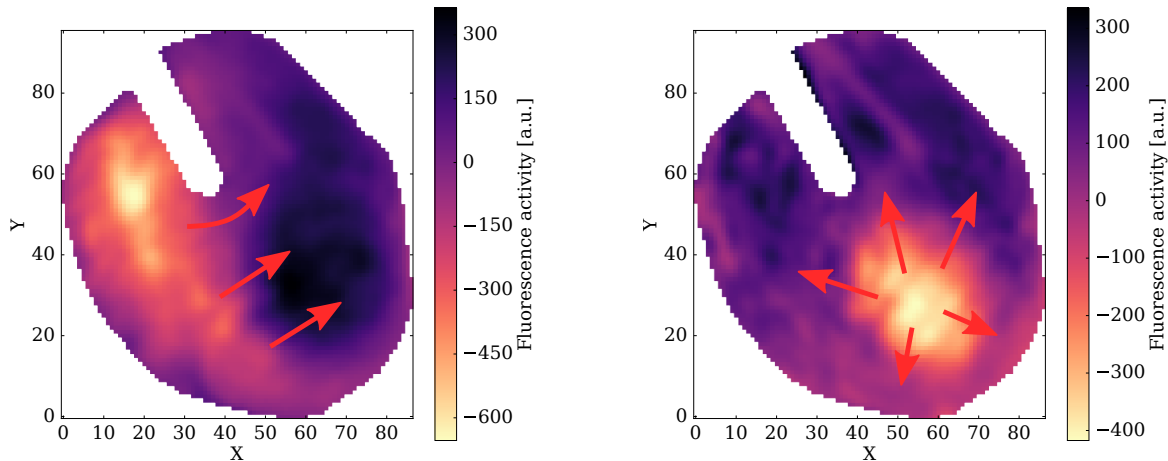
3. Results

Sec. 2.2.2 that there are some theoretical problems associated with the quantification of complexity from surface camera data only:

- Noise from various sources can deteriorate the quality of the necessary information significantly, which can only partly be coped with by (live) data preprocessing. See also Sec. 2.5 for a discussion of noise sources.
- The surface data only contains limited information about the full dynamical state of the system. See also Sec. 3.4.3 for a more detailed discussion of this problem.
- As it will be demonstrated in Sec. 3.5.1 a low complexity of the dynamical system can manifest itself heterogeneously in spatially resolved complexity measures. This suggests more sophisticated definitions of the complexity regimes based on specific configurations of rotors.

During this experiment fluorescence signals of the heart during VF of very high quality were recorded. One of these datasets will be analysed in the next section for demonstrating the application of complexity measures for spatiotemporal dynamics to real data.

3.4.3. Analysis of Surface Camera Data



(a) Snapshot of the front left camera of a rabbit heart during VF. This snapshot shows plane wave activity at frame 1556 (3.1s). The arrows indicate movement of the waves.

(b) Snapshot of the front left camera of a rabbit heart during VF. This snapshot shows focal activity at frame 1203 (2.4s) with propagating circular waves which emerged from below the surface of the heart. The arrows indicate movement of the waves.

Figure 3.28.: Two snapshots from the front left camera of a rabbit heart during VF. This dataset was recorded on 2016-09-05 and belongs to the entropy camera pacing experiment series described in Sec. 3.4.1.

One of the fluorescence datasets²¹ from the entropy camera experiments is analysed here for researching the association between spatiotemporal complexity recorded on the surface and complexity fluctuations in the ECG. The recordings consist of one video per camera at a resolution of 128×128 pixels sampled at 500 Hz and 16 bit per pixel. DI-4-ANEPPS has been used as the voltage sensitive dye. As a result of the implementation used here, the upstrokes of the action potential are inverted and point downwards. General preprocessing of the video data includes the removal of camera-specific jitter, masking and cropping and spatial and temporal filtering. The masking is done manually by selecting an area where activity at a high signal to noise ratio is observed and excluding all points outside this area from the analysis. During this procedure also activity in unwanted areas of the heart is removed. In Fig. 3.45 it is visible in the top left corner that a stripe containing a pacing electrode has been masked out. Temporal filtering is done using a Butterworth bandpass filter with lower frequency at 0.5 Hz and upper frequency at 30 Hz. Spatial filtering is done for each image of the video separately using a Gaussian smoothing filter with a standard deviation of 1.5.

²¹Video no. 127 of Exp. 01, 2016-09-05

3. Results

The processing and the analysis of the video data is done using PythonAnalyser which is described in Sec. A.5 in the appendix. PythonAnalyser includes many other methods for quantifying spatiotemporal dynamics, like dominant frequency maps, wave tracking and the approach based on entropy rate presented in [92]. The analysis presented here is focused on specific quantities which were considered the most appropriate for determining the relationship between fluorescence signals from ex vivo experiments and complexity fluctuations during VF.

Fig. 3.29 shows the results obtained for the computation of the phase synchronisation index (PSI) separated by camera. The PSI has been computed by generating a phase signal for each pixel using the zero-crossing method²². The PSI is calculated using Eq. 2.23. As the PSI has to be calculated pairwise between each pair of time series, the computation can become extremely resource intensive. As neighbouring pixels contain very similar information, subsampling of the image is a reasonable option. Therefore only every fourth time series, both in x- and y-direction, are used for the calculation. The length of the time window, named N in Eq. 2.23 is set to 250 frames which equals half a second. Here the PSI has been computed for every 10th time step (20 ms). Each point in one PSI time series shown here represent the average over the PSI values of all pairs of time series the PSI was computed from.

The values for the phase synchronisation index vary between 0.38 and 0.57 which is rather low compared to the full interval $[0, 1]$ suggesting that a complete phase synchronisation of the full tissue was never observed on a single camera. There seems to be a correspondence between both front cameras, especially up to 4 s which is quantifiable by a correlation coefficient of 0.7. The correlation coefficient between the back cameras is 0.46 and there seems to be no correlation between the front and back cameras (average correlation coefficient of -0.08). The period of higher synchronisation which is identified by the front cameras at approximately 3 s can be associated with the plane wave activity visible in Fig. 3.28a while Fig. 3.28b seems to belong to a less synchronized time interval.

²²The phase signal is determined by interpolation between consecutive intersections of the time series with the baseline in the same direction.

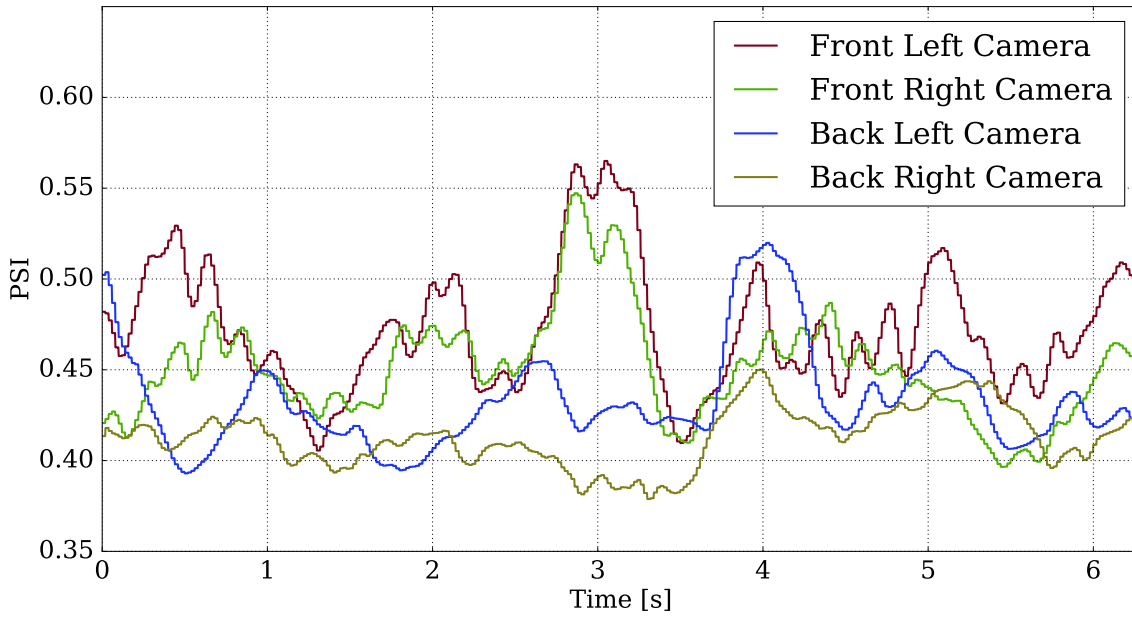


Figure 3.29.: Time series of the Phase Synchronisation Index (PSI) for all four cameras of the entropy camera pacing dataset.

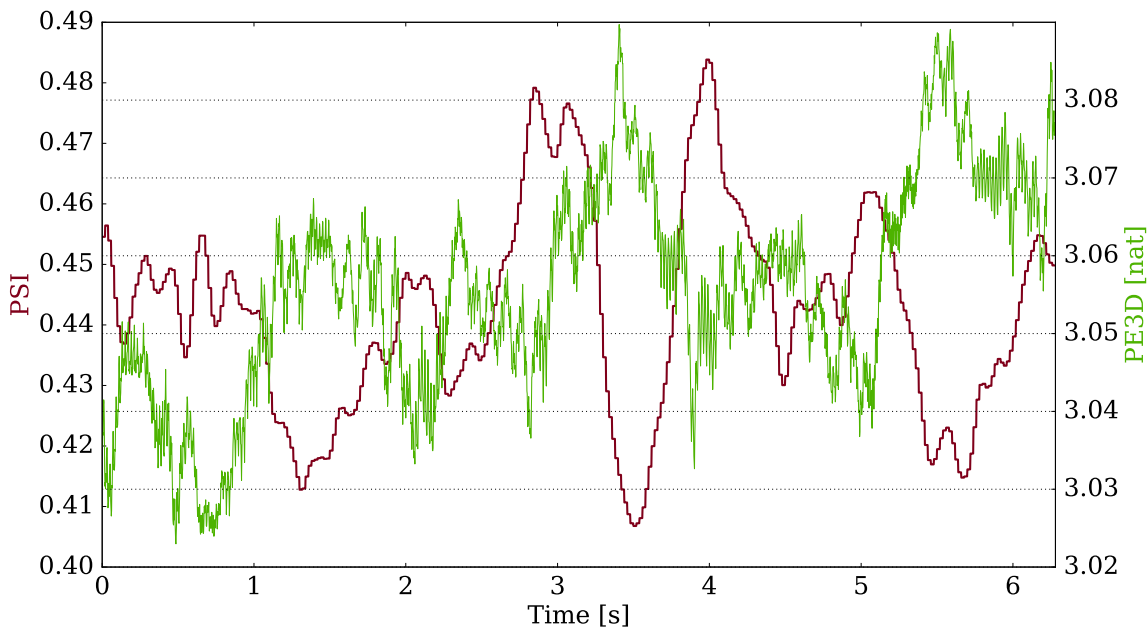


Figure 3.30.: Time series of the mean PSI and mean 3D permutation entropy (PE3D) for the entropy camera pacing dataset.

3. Results

Fig. 3.30 show the results obtained for the same dataset for the 3D permutation entropy PE3D. The PE3D is the three-dimensional extension of the permutation entropy and quantifies the distribution of spatiotemporal order patterns as described in Sec. 2.2.3. It is computed here for temporal intervals of 0.5 s a spatial lag of 12 pixels²³, a temporal lag of ten time steps and on a subset of every fourth time series in x- and y-direction. It is anti correlated to the PSI with a correlation coefficient of -0.41.

A similar quantity which does not take temporal information into account is the two-dimensional permutation entropy (PE2D) described in Sec. 2.2.3. Fig. 3.31 shows the application of this quantity to the rabbit heart dataset. This quantity reacts much more sensitive to changes due to the movement of waves over the tissue. One obvious effect is that the emergence of new waves creates many different spatial order patterns resulting in an increase in the PE2D. The opposite effect is seen when the waves leave the field of view or vanish due to annihilation. As these small scale fluctuations are usually unwanted when looking at the complexity of the camera signals, a running mean smoothing filter with a window length of 0.5 s has been applied. The smoothed version of the PE2D seems to resemble some aspects of the dynamics which are also visible in the PSI. This especially holds for the desynchronised time period at 5.5 s. Also for the synchronised time period at 4 s a strong decrease in PE2D is achieved. For the synchronised time period at 3 s, however, the smoothed PE2D does suggest simpler patterns. Also between zero and 1.5 s the PE2D and PSI curves indicate a correlation instead of an anticorrelation. The waves which lead to synchronisation of the tissue can have different shapes and can therefore lead to different two-dimensional order pattern statistics. This can explain why there does not necessarily have to be an anticorrelation between PSI and PE2D, and the latter quantity contains additional information.

A similar comparison can be done for the number of phase singularities which is displayed in Fig. 3.32. One important observation for the raw number of phase singularities in Fig. 3.32b is that it decreases to zero very often. One reason for this is that the activity visible on the surface does not only consist of spiral-like patterns, but very often also of plane waves or focal activity which does not produce phase singularities. It again makes sense to take broader time windows into account for comparison. The smoothed NPS which is shown in Fig. 3.32a is also able to highlight many features of the spatiotemporal dynamics which are visible in the PSI. In this example dataset the smoothed NPS is anticorrelated to PSI with $C = -0.43$ and correlated to the PE2D with $C = 0.41$ and to the PE3D with $C = 0.62$.

²³Note that this is reduced to 3 pixels on the subsampled video.

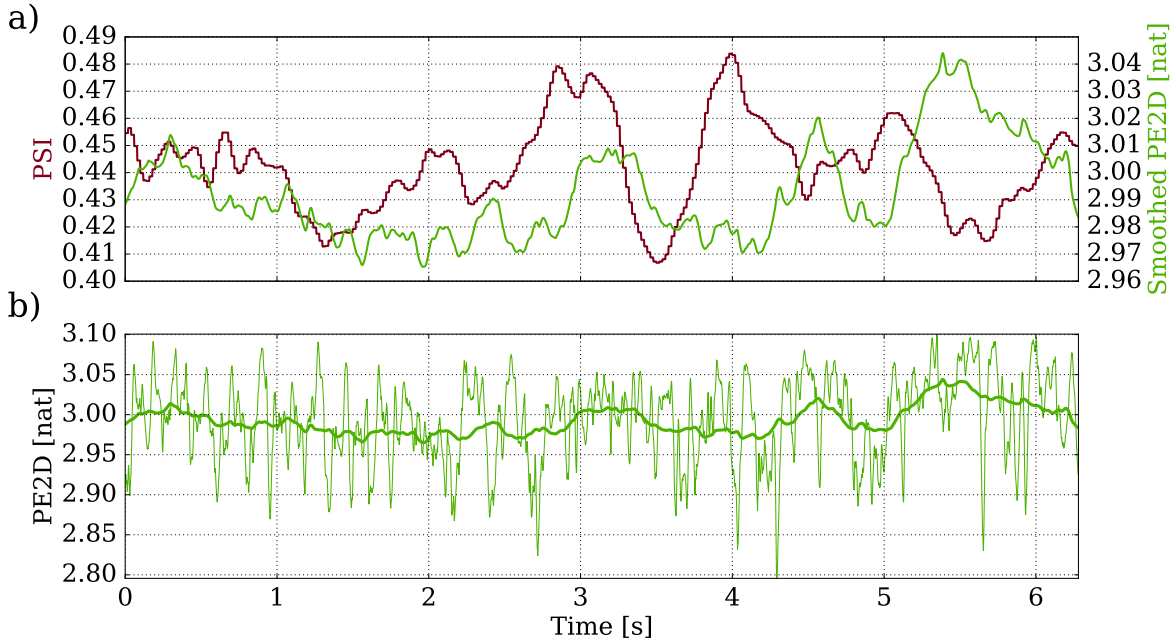


Figure 3.31.: Comparison between the PSI and the two-dimensional permutation entropy (PE2D). a) shows the PSI together with the smoothed version of the PE2D. b) displays the raw PE2D and the smoothed version. Both, PSI and PE2D are averages over all corresponding quantities computed for the individual cameras.

The next comparison shown here is between PSI and the permutation entropy (PE) derived from the ECG. This comparison is carried out to answer the question whether there is a direct relation between the complexity derived from the ECG and the complexity measures for spatiotemporal dynamics derived from the camera data.

Fig. 3.33 shows three different comparisons where in all cases the green line is the PE. Fig. 3.33a shows the average of the PSI over all four cameras. It is visible that in the beginning between 1s and 2.4s the PE seems to correspond very well to the dynamics depicted by the PSI. The drop in PSI is accompanied by a strong rise in PE and also the rise in PSI shortly afterwards is followed by a steep decrease in the complexity of the ECG signal. Up to 5s there seems to be a completely different relation between both complexity time series while it seems to be anticorrelated again afterwards. To investigate the possible effect of different camera perspectives the same analysis has also been done for a PSI average only over both front cameras in Fig. 3.33b and for a PSI average only over both cameras on the back side in Fig. 3.33c. There are some minor differences visible between Fig. 3.33b and Fig. 3.33c, especially regarding the time periods of higher synchronisation at 3s and 4s which are visible only on one of the views respectively. The general conclusion, however, does not change much.

3. Results

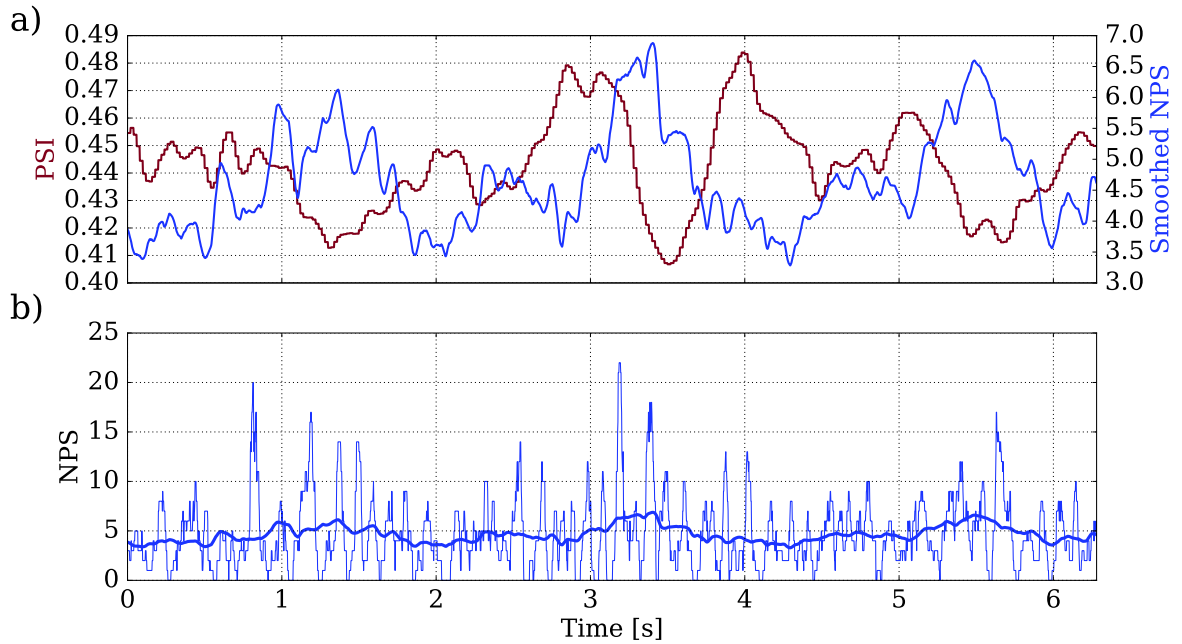


Figure 3.32.: Comparison between the PSI and the number of phase singularities (NPS). a) shows the PSI together with the smoothed version of the NPS. b) displays the raw NPS and the smoothed version. The PSI is the average over all PSI time series computed individually for each camera. The NPS is the sum of the phase singularities on all cameras.

The observations for the comparison between PE and NPS in Fig. 3.34 are very similar to the comparison between PSI and PE. Up to 3s there seems to be a linear dependency between both quantities, especially when looking at the average over all cameras in Fig. 3.34a. This trend does not continue and no coherent period of linear dependency is found afterwards. Especially in Fig. 3.34 it is interesting to see that patterns sometimes seem to match on different cameras. Starting from 3.8s the PE curve seems to much better follow the NPS curve when averaging over the back cameras in Fig. 3.34c than when averaging over the front curves in Fig. 3.34b.

Although it might be possible that the measures for quantifying complexity applied here do not capture sufficient information from the measured signals to be able to fully quantify the association between the ECG and the fluorescence data, one conclusion from this analysis is that this relation cannot be established using a single ECG and data from the surface of the tissue. This is completely in line with results obtained for simulated data in Sec. 3.5.1 and Sec. 3.5.3. One conclusion from Sec. 3.5.1 is that it is not unlikely to record the ECG from an angle where the complexity situation is much different than it would be expected by looking at the number of phase filaments.

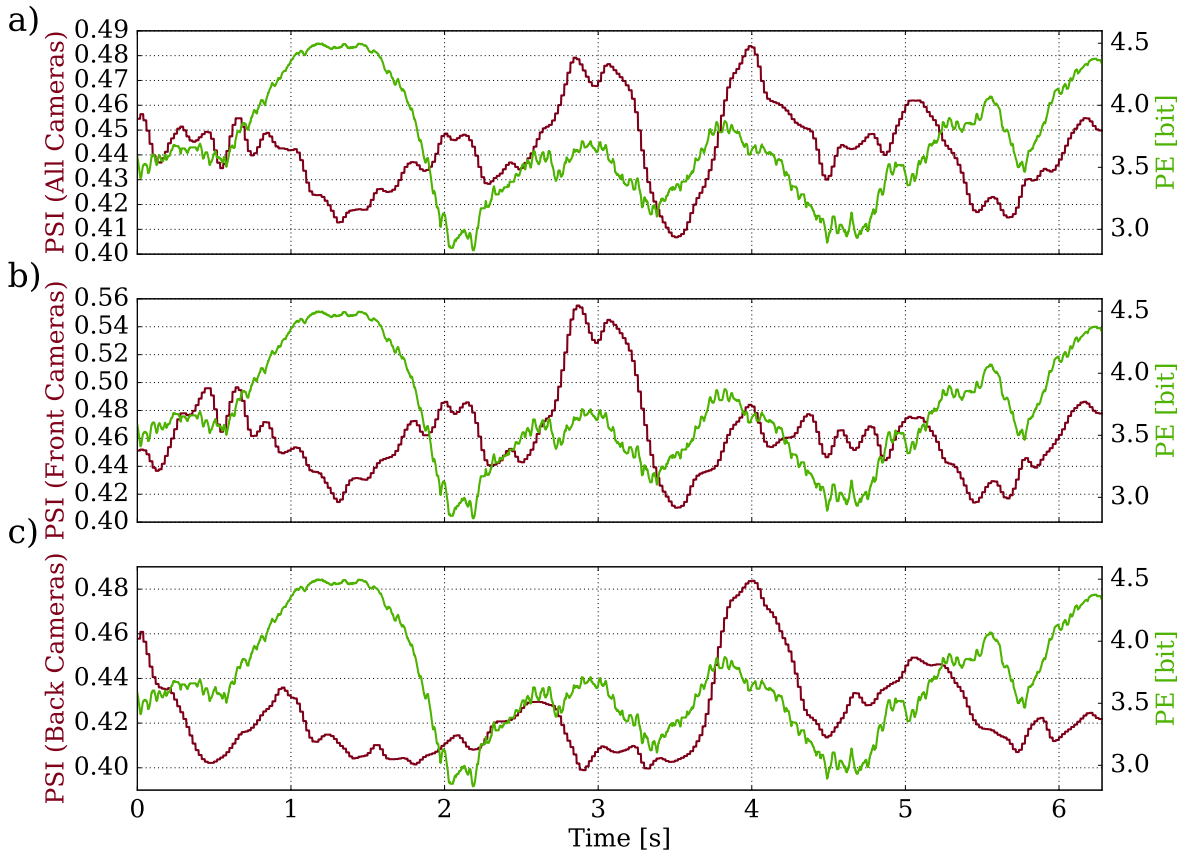


Figure 3.33.: Comparison between the PSI and the PE which is derived from the ECG. a) b) and c) display the PE as a light green line. a) shows the PSI as an average over all four cameras. b) shows the PSI average only over the two cameras “Front Left” and “Front Right”. c) shows the PSI average only over the two cameras “Back Left” and “Back Right”.

3. Results

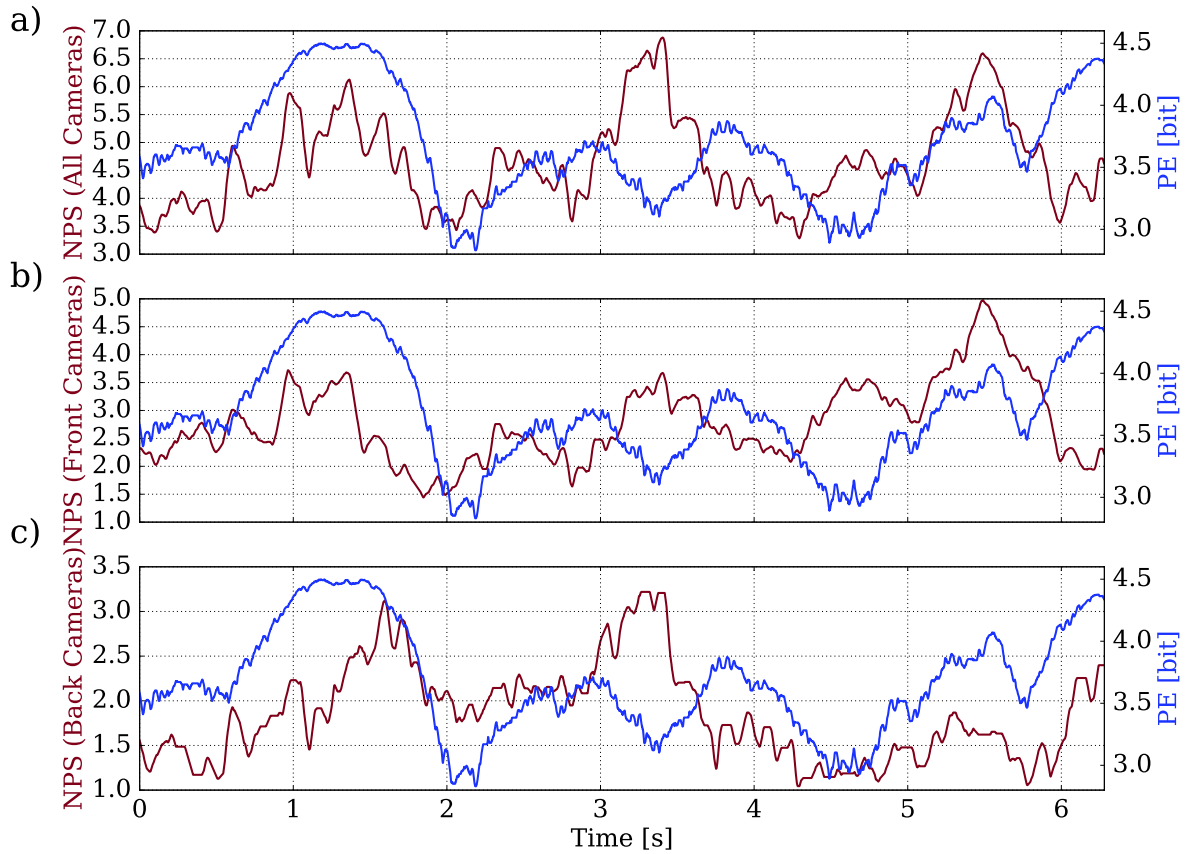


Figure 3.34.: Comparison between NPS and PE which is derived from the ECG. a) b) and c) show PE as a blue line. a) shows the average number of phase singularities (NPS) over all four cameras. b) shows only the average of NPS over the two front cameras “Front Left” and “Front Right”. c) shows the average of NPS over the two back cameras “Back Left” and “Back Right”.

Fig. 3.35 summarizes the correlations between the quantities discussed here.

3.4.4. Summary and Conclusions

In this section experimental results from experiments to trigger the defibrillation on PE derived from fluorescence signals were presented. Furthermore data from fluorescence imaging were analysed using several methods for analysing the complexity of spatiotemporal dynamics. The following conclusions can be drawn:

- The entropy camera pacing experiments did not show a better success probability for defibrillation shocks given into low complexity periods than for shocks given

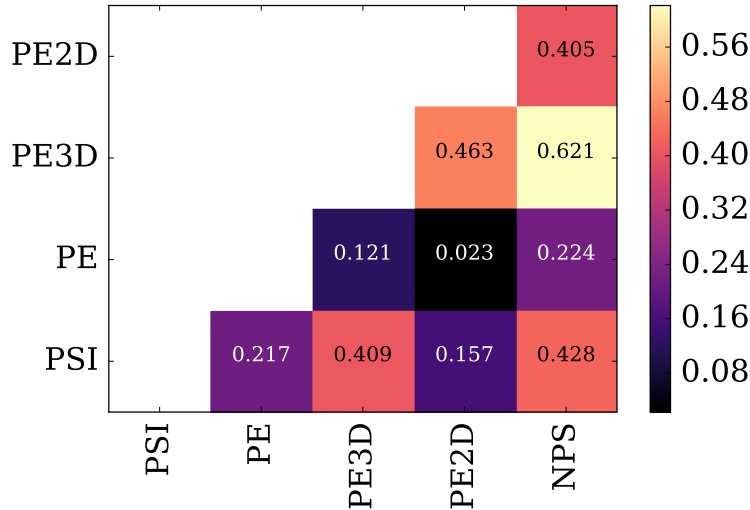


Figure 3.35.: Summary of the correlations of the complexity measures discussed in Sec. 3.4.3. PE is the permutation entropy computed from the ECG in bit. The other quantities are the respective time series averaged over all four cameras. PSI was multiplied by -1 before computing the correlations.

into high complexity periods.

- All quantities for measuring spatiotemporal complexity detect variations in complexity. There is some overlap in the detection, most notably the correlation between PE3D and NPS of $C = 0.62$. No conclusive dependencies between the complexity measures derived from the fluorescence signals and complexity of the ECG were seen.
- Different complexity was seen on different camera views. Especially between the two front cameras and the two back cameras differences in the magnitude of synchronisation were observed.
- Regarding the mismatch between complexity measured from the ECG and from the fluorescence data, there are two main hypotheses:
 - The spatiotemporal dynamics on the surface does not reveal enough information about the full state of the system.
 - The ECG information given by one ECG direction does not contain enough information to be representative of the spatiotemporal dynamics.

Although only the detailed analysis of one dataset is shown here, it is exemplary for many video datasets from many experiments which have been analysed for the same

3. Results

purpose. Also many other quantities for analysing fluorescence data were tried, such as wave tracking, dominant frequency maps and activation maps. However no stable association between the complexity of spatiotemporal dynamics and the complexity in the ECG could be concluded.

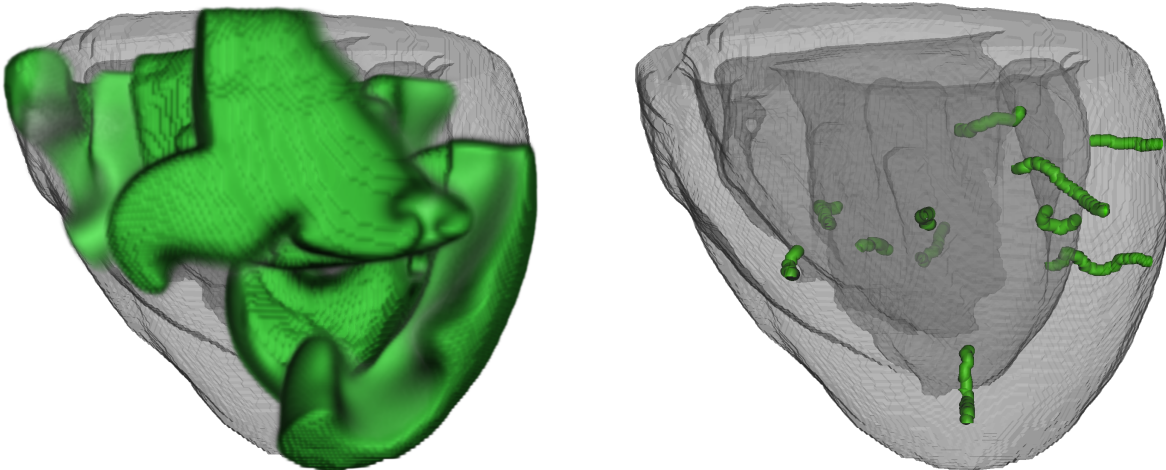
The following section will investigate the dependency between the complexity in the ECG and the direction of measurement using simulated data. In experimental settings the dependency between surface activity, ECG and the full dynamic state of the heart is much more difficult to assess and requires the development of novel measurement devices.

3.5. Angular Dependency of Complexity Fluctuations

This section will shed light on the origin of the complexity fluctuations in the ECG by analysing data from 3D Fenton-Karma simulations which have been computed by Thomas Lilienkamp. The dataset includes a time series of the full three-dimensional state of V_m of the simulation, the computations of the ECG as shown in Sec. 2.3 and a time series of the number of phase filaments (see Sec. 2.2.2). Sec. A.9 gives more information about this collaborative project. Parts of the results of this section are contained in a publication which is currently in preparation.

Sec. 3.5.1 shows that complexity fluctuations in the ECG also exist in this simulated cardiac system. They can be associated with the number of three dimensional vortices which are quantified by NFIL. Furthermore it will be shown that the correlation between PE and NFIL is dependent on the angle of the virtual ECG point electrode which reveals the spatiotemporal nature of the phenomenon of complexity fluctuations.

In order to illustrate the simulation data, two snapshots of V_m and filaments are given in Fig. 3.36 and Fig. 3.37.

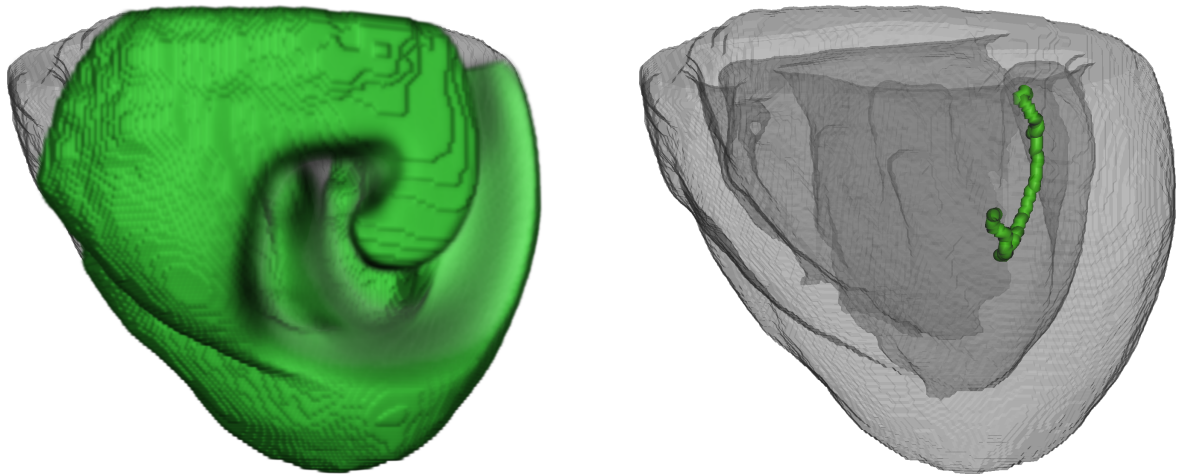


(a) Snapshot of V_m of the simulated heart at frame 2200 showing several interacting scroll waves.

(b) Snapshot of the phase filaments of the simulated heart at frame 2200. The phase filaments are the centers of rotation of the scroll waves.

Figure 3.36.: Snapshots of V_m and the phase filaments at frame 2200 for the simulated heart, simulation no. 95. These snapshots are taken from an angle of 115 degrees (see Fig. 3.42 for details).

3. Results



(a) Snapshot of V_m of the simulated heart at frame 3170 seen from an angle of 115 degrees (please refer to Fig. 3.42 for details).

(b) Snapshots of the phase filaments of the simulated heart at frame 3170.

Figure 3.37.: Snapshots of V_m and the phase filaments at frame 3170 for the simulated heart, simulation no. 95, showing a single scroll wave. These snapshots are taken from an angle of 115 degrees (see Fig. 3.42 for details).

3.5.1. Results from 3D Simulations

Fig. 3.38 and Fig. 3.40 show the results obtained for two different simulation cases in a detailed and condensed manner. Each figure is showing the following subplots:

- a) The PE time series obtained for each of the 360 angles of the ECG. The two dashed colored lines indicate the angular locations of two ECG excerpts displayed in b) and c). The blue line corresponds to the angle under which the PE has the minimum correlation to NFIL and the yellow line corresponds to the angle yielding the maximum correlation coefficient.
- b) The ECG excerpt (computed using Eq. 2.27) corresponding to the PE time series marked with the **yellow** line in a). This ECG excerpt belongs to the PE time series which has the **maximum correlation coefficient** with NFIL.
- c) The ECG excerpt (computed using Eq. 2.27) corresponding to the PE time series marked with the **blue** line in a). This ECG excerpt belongs to the PE time series which has the **minimum correlation coefficient** with NFIL.
- d) The raw number of phase filaments is plotted as a black time series. As described

3.5. Angular Dependency of Complexity Fluctuations

in Sec. 2.2.2 this number can be directly associated with the number of rotation centers of three dimensional vortices. The red line in this subplot is the smoothed number of phase filaments (NFIL). It is smoothed using a running mean with the same window size that has been used for the calculation of the PE (250 simulation frames²⁴). This red line is also added to the subplot e) for facilitating the comparison with the PE time series.

- e) shows the PE time series in black which is obtained for the maximum value of the correlation coefficient between PE and NFIL. This means that this PE time series belongs to the yellow line in a) and to the ECG excerpt in b). For comparison NFIL is plotted as a dashed red line. The dashed gray line in the background indicates the PE obtained from the ECG which yielded the minimum correlation coefficient between PE and NFIL. As described earlier this PE belongs to the blue line in a) and to the ECG excerpt in c).

In addition to these two overview plots in Fig. 3.38 and Fig. 3.40, plots which display the corresponding correlation values are given in Fig. 3.39 and Fig. 3.41. These two plots show the relationship between the value of the correlation coefficient between PE and NFIL²⁵ and the angle under which the ECG was acquired. The two vertical lines refer to the horizontal lines in Fig. 3.38 and Fig. 3.40:

- The yellow line marks the angle under which the correlation coefficient between PE and NFIL has its **maximum** value.
- The blue line marks the angle under which the correlation coefficient between PE and NFIL has its **minimum** value.

The values for the respective correlation coefficients are given in the box at the upper edge of the plots. The exact values for the angles of observation are given in the lower box.

The two simulation cases (no. 50 and no. 95) have been chosen for demonstration here because they show two qualitatively different situations which will be described in more detail in the text below. The main difference is the appearance of a time period with a very strong angular dependency of the correlation for simulation case no. 95.

²⁴The justification for this smoothing procedure lies in the comparison to the PE which has been computed for exactly the same window length. The smoothing can be expected to remove small timescale variations and produce a quantity that shows variations on a similar time scale. This procedure leads to slightly higher values of the correlation coefficient than a computation of the correlation of PE with the raw number of phase filaments would indicate.

²⁵NFIL always refers to the smoothed version of the number of phase filaments.

3. Results

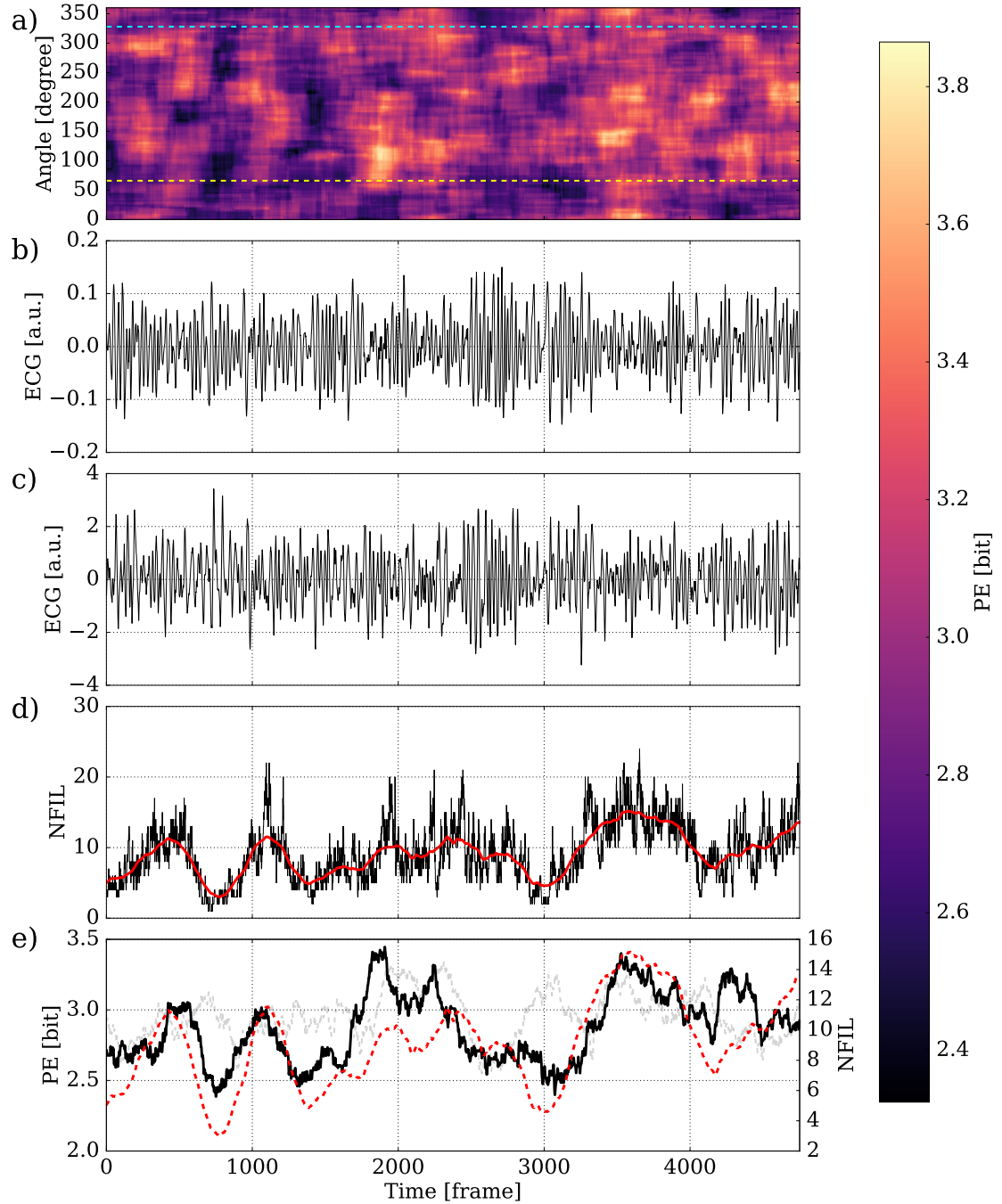


Figure 3.38.: Angular dependency of the PE computed for the realistic ECG defined in Eq. 2.27 which was calculated for the 3D Fenton-Karma simulation dataset no. 50. a) shows the development of PE over time for 360 angles. b) shows an ECG excerpt at 66 degrees (horizontal yellow line in a)). c) shows an ECG excerpt at 328 degrees (horizontal blue line in a)). d) shows the raw number of phase filaments (black) together with its smoothed version (NFIL, red line). e) shows the PE (black) of the ECG from b) together with NFIL (dashed red line). For comparison the PE of the ECG from c) is added in light gray color. See the text for more details.

Detailed Discussion

The result for the first simulation case displayed here in Fig. 3.38 reveals a lot of information about the nature of laminar phases. It was already shown in Sec. 3.3 that this type of simulation produces fluctuations in the ECG similar to those observed in ex vivo experiments or humans (see Fig. 3.2, Fig. 3.3 and Fig. 3.5). In Fig. 3.38a) phases of low complexity can be identified by dark spots which correspond to low values of PE. Interestingly the simulated ECG does not reveal laminar phases so easily to the eye as they do not seem to be coupled so much to the amplitude of the ECG signal. One example is the first laminar phase in this VF episode which can be seen around frame 800 in Fig. 3.38a) and Fig. 3.38e): The PE shows a clear drop to just above 2.4 bit. Here we can be sure that this can in fact be considered a less complex phase in a dynamical sense, as simultaneously the number of phase filaments (NFIL) drops below 4 (with minimum being one).

The black spots and lighter areas suggest a dependency on the angle of the ECG electrode. This effect is quantified in Fig. 3.39 which shows the correlation coefficient between PE and NFIL when the angle is varied. The maximum correlation is 0.62 and the minimum correlation is 0.17.

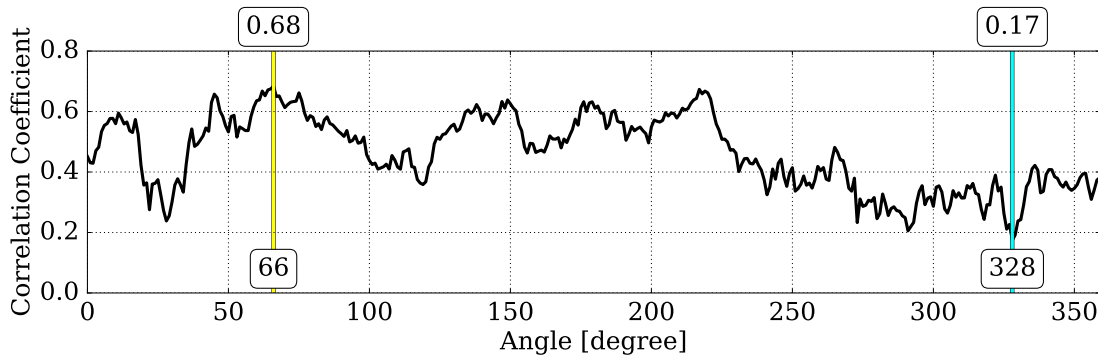


Figure 3.39.: Correlation coefficient between the smoothed number of filaments and the PE computed for different angles of the ECG from which the respective PE was computed. This figure visualizes that there are angles under which the complexity computed from the ECG can be associated much better with the complexity of the underlying spatiotemporal dynamics than others.

The second case shown here even demonstrates a more interesting spatiotemporal phenomenon. In Fig. 3.40 it is clearly visible that there is a temporal region with a very prominent laminar phase around frame 3000 which is visible for a specific range of angles. For $\varphi = 84^\circ$ however the ECG appears to be extremely complex achieving PE values close to 3.6 bit.

3. Results

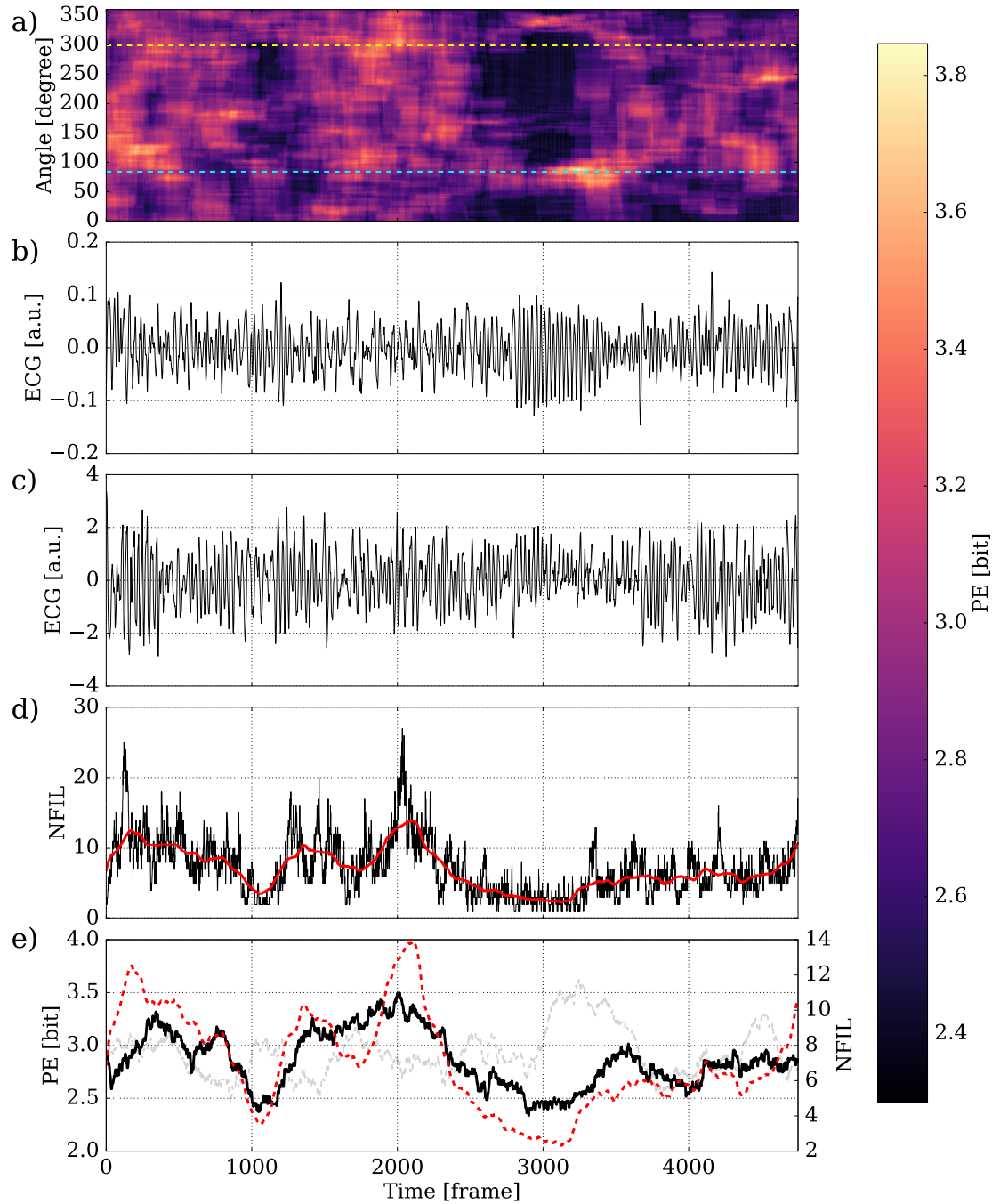


Figure 3.40.: Angular dependency of the PE computed for the realistic ECG defined in Eq.2.27 which was calculated for the 3D Fenton-Karma simulation dataset no. 95. a) shows the development of PE over time for 360 angles. b) shows an ECG excerpt at 299 degrees (horizontal yellow line in a)). c) shows an ECG excerpt at 84 degrees (horizontal blue line in a)). d) shows the raw number of phase filaments (black) together with its smoothed version (NFIL, red line). e) shows the PE (black) of the ECG from b) together with NFIL (dashed red line). For comparison the PE of the ECG from c) is added in light gray color. See the text for more details.

Fig. 3.41 quantifies this situation using the correlation coefficient and emphasizes the extreme situation for this simulation case: The correlation coefficient can become $C = 0.81$ for $\varphi = 299^\circ$. For some angles the correlation coefficient drops below zero down to a minimum of $C = -0.33$.

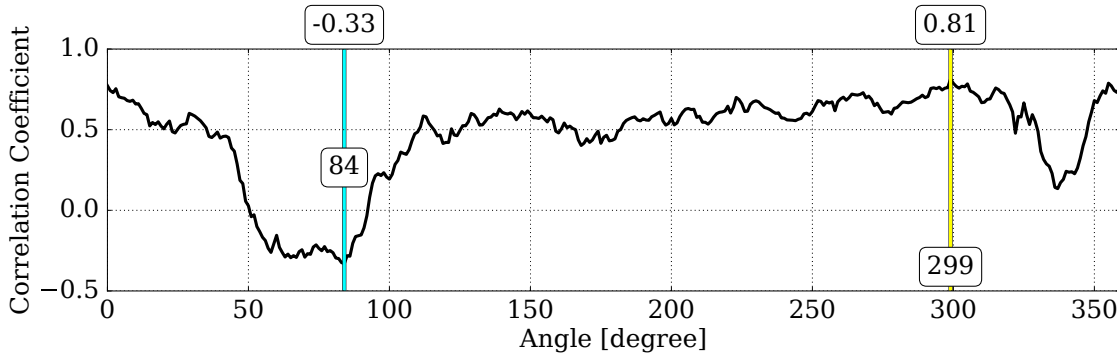


Figure 3.41.: Dependency of the correlation coefficient between NFIL and the PE for on the angle of the ECG for simulation case 95. The yellow and blue lines mark the points of maximum and minimum correlation and show the corresponding exact angle (lower box) and the associated correlation value (upper box).

This finding has important practical implications. In order to make reliable estimates for the complexity of the ECG for development of specific pacing strategies it is important to not rely on single ECG measurements. It is important to use ECG electrodes covering different directions in order to reliably capture laminar phases. Fig. 3.39 and Fig. 3.41 suggest that the number of ECG directions needed is not too high which will be discussed quantitatively in the next section.

It should also be pointed out that although there might be some tendency for specific angles allowing for better predictions than others. One reason to assume this lies in the anatomy and geometry of the heart itself. Some anatomical structures can be expected to attract rotors, allowing for example pinning, and therefore increase the likelihood to detect important dynamics in the respective regions. However, this can not generally be expected, as the spatiotemporal dynamics in the heart can show very different behaviours. As it can already be seen in the two examples provided here there are some cases which are more extreme in terms of heterogeneity between different angles than others and also the angles which would allow better predictions differ very much.

3. Results

Simulation Case (i)	$C_{i,i,\max}$	p_i
50	0.68	0.00
55	0.69	0.00
65	0.79	0.00
75	0.67	0.00
80	0.63	0.08
90	0.56	0.15
95	0.81	0.00
100	0.77	0.00
105	0.49	0.00
110	0.77	0.00
115	0.64	0.00
120	0.66	0.00
125	0.67	0.00
135	0.51	0.15

Table 3.7.: Results for the correlations and p -values of all simulation cases. See Sec. 3.5.2 for a description of the corresponding surrogate test.

3.5.2. Surrogate Analysis of Correlations

In order to test whether correlation results are stable and significant the maximum correlation coefficients (Eq. 2.28) have been calculated for other simulation cases and a surrogate test has been carried out as follows: Assuming that the dynamics of the simulation cases are independent from each other there should be a much lower maximum correlation between the number of filaments of simulation case j and the (angle dependent) PE of simulation case i for $i \neq j$ than for $i = j$. In other terms, the number of filaments of simulation case j can be seen as surrogates for determining the maximum correlation between NFIL and the (angle dependent) PE of simulation case i . Therefore the following procedure was used as a surrogate test. In this description $C_{i,j,\max}$ is defined as the maximum Pearson correlation coefficient over all angles φ :

$$C_{i,j,\max} = \max(C(\text{NFIL}_j, \text{PE}_i(\varphi))) \quad (3.4)$$

- Calculate the real correlation values $C_{i,i,\max}$ using Eq. 3.4 for simulation case i .
- Compute the distribution of correlation values $C_{i,j,\max}$ using Eq. 3.4 for $j \neq i$.
- Determine the p -value p_i as the fraction of $C_{i,j,\max}$ with $j \neq i$ which are greater than or equal to $C_{i,i,\max}$.

Tab. 3.7 displays the result of the correlation values and the p -values calculated in this

analysis. A mean correlation of 0.67 with standard deviation of 0.10 is achieved for all simulation cases reported here. Three of the cases lead to a non-significant p -value larger than the commonly used significance threshold of 0.05. All other 11 cases show a highly significant correlation, because non of the surrogates gave a correlation value larger than or equal to the real one.

A similar procedure can also be used to test whether for case i there are cases with $k \neq j \wedge (k = i \vee j = i)$ which result in $C_{j,k,\max} \geq C_{i,i,\max}$. The result is qualitatively similar, giving non-zero p -values only for simulation cases 80 ($p = 0.08$), 90 ($p = 0.12$), 105 ($p = 0.12$) and 135 ($p = 0.27$).

3.5.3. Analysis of Surface Camera Data

In order to investigate details of the effect observed in Fig. 3.40 around frame 3000 data from surface cameras can be used. This type of data mimics the experimental approach where fluorescence data is only available from the surface of the heart and only for a low number of projections. Camera data of this simulation dataset has been extracted and comprises four different views of the surface of V_m . These datasets are preprocessed using spatial Gaussian smoothing (with a standard deviation of the Gaussian kernel of 2.0) and pointwise normalization (subtraction of the temporal mean and division by the standard deviation). Different spatiotemporal aspects are analysed using phase singularity analysis, phase synchronisation index and PE3D.

Fig. 3.42 shows an overview about the geometry of the angle dependent ECG and the positions of the cameras relative to the simulated heart. Figs. 3.43-3.46 show snapshots from the four cameras at two distinct time points which were selected from the overview presented in Fig. 3.40 of the previous section:

- Frame 2200 of the simulation is a snapshot during a period of high spatiotemporal disorder with multiple phase filaments and a high PE.
- Frame 3000 displays the situation during the period with strongly heterogeneous complexity.

During the heterogenous phase, cameras one, three and four show mainly plane wave activity. The movement of the plane waves is indicated by the red arrows in Figs. 3.43b, 3.45b and 3.46b.

3. Results

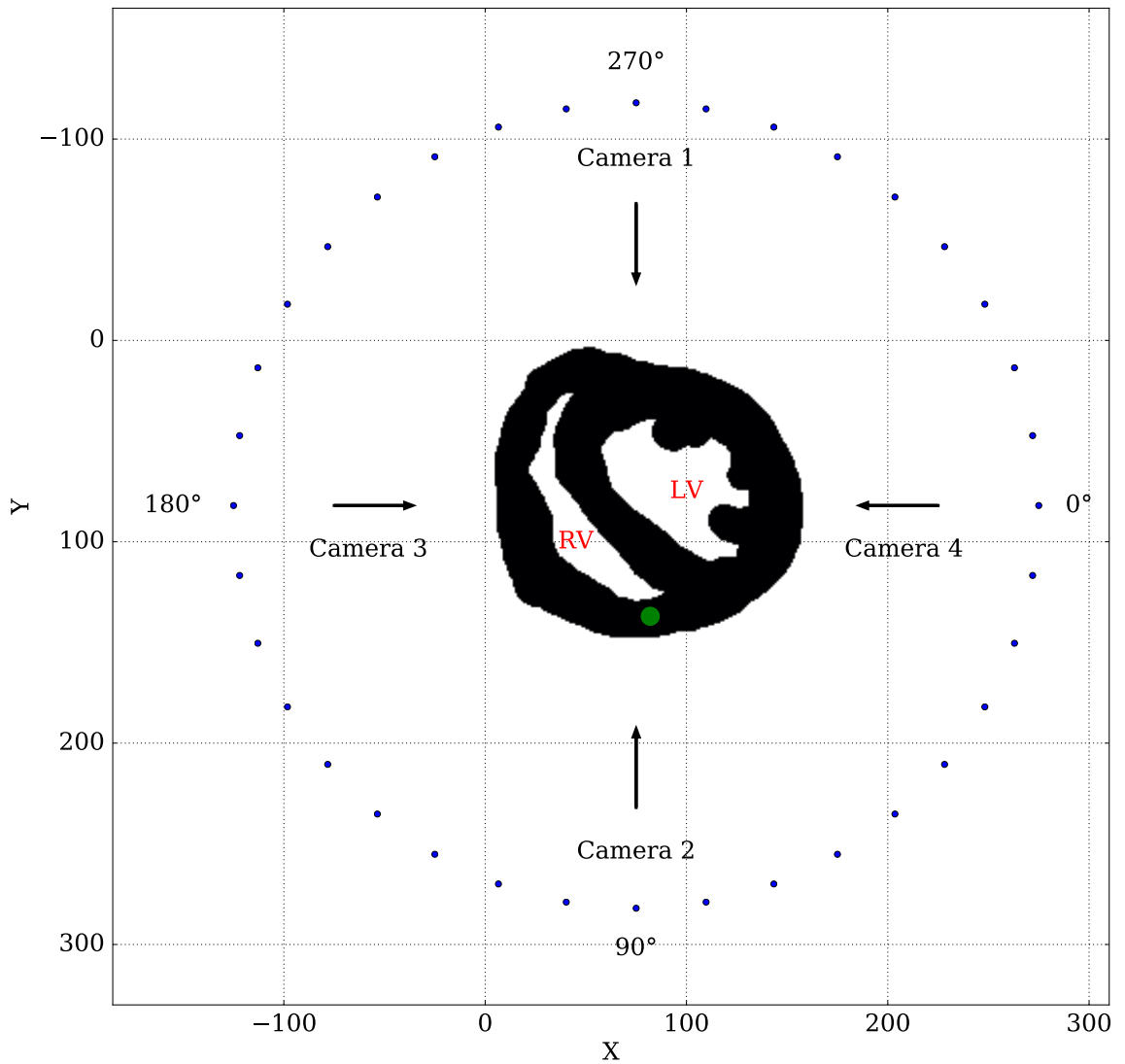
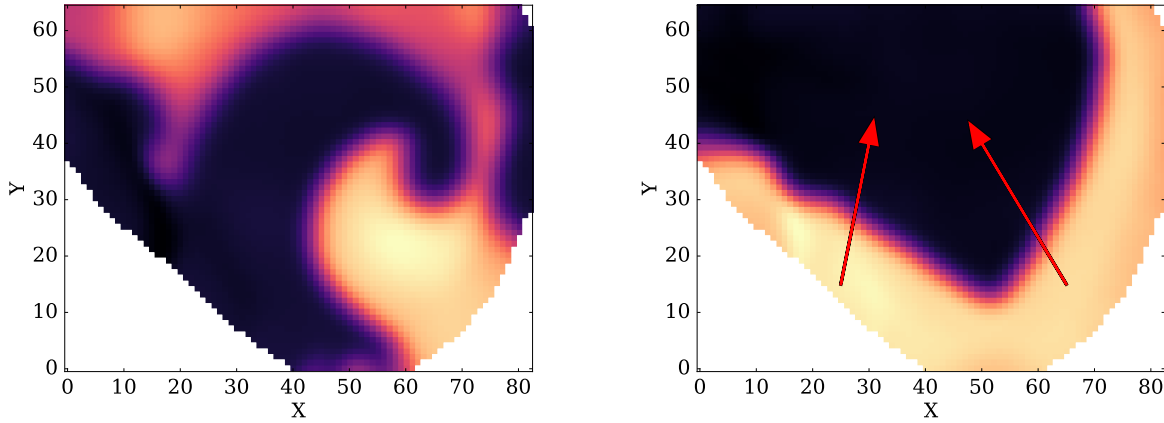


Figure 3.42.: Overview over the camera positions and positions of the simulated ECG electrodes. The object in the center is a slice through the simulation domain at a constant height ($z = 15$). Black color corresponds to simulated tissue while white color indicates absence of tissue. The blue points illustrate the positions of the ECG electrodes used for extracting the realistic ECG (only every tenth electrode is plotted here) using Eq. 2.27. The cameras are sketched by the black arrows and record the surface of the simulated rabbit heart. A slice through the left ventricle (LV) and the right ventricle (RV) is visible. The green spot marks the approximate location of the filament of the scroll wave which appeared during the heterogenous laminar phase which is discussed in the text. It is also visible in the camera snapshot at frame 3170 in Fig. 3.44.

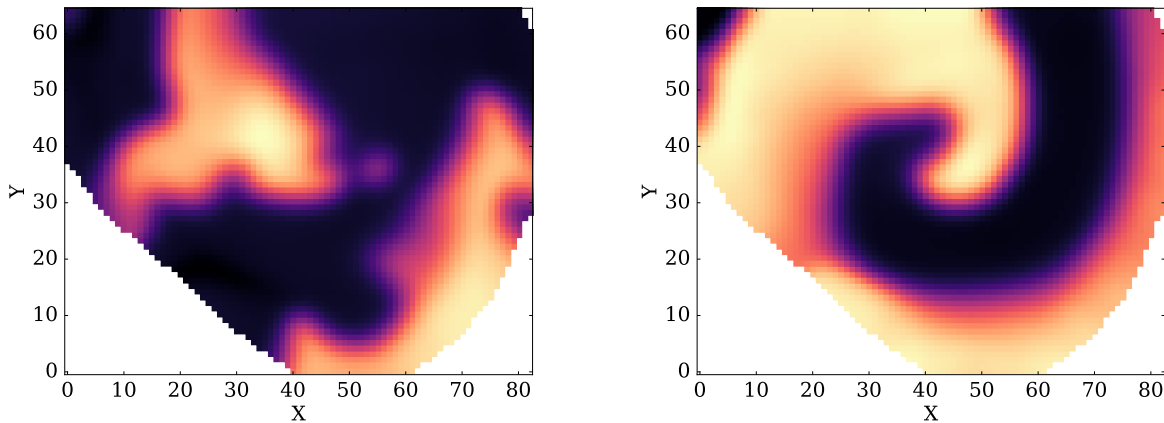
3.5. Angular Dependency of Complexity Fluctuations



(a) Snapshot of the surface of V_m at frame 2200. This snapshot in time lies within a period of high complexity according to Fig. 3.40.

(b) Snapshot of the surface of V_m at frame 3170. This temporal interval indicates a situation with very inhomogeneous complexity with respect to the angle of observation (see Fig. 3.40). The arrows indicate the movement of the (plane) waves.

Figure 3.43.: Snapshots of camera 1 which observes the simulated rabbit heart under an angle of 270 degrees.

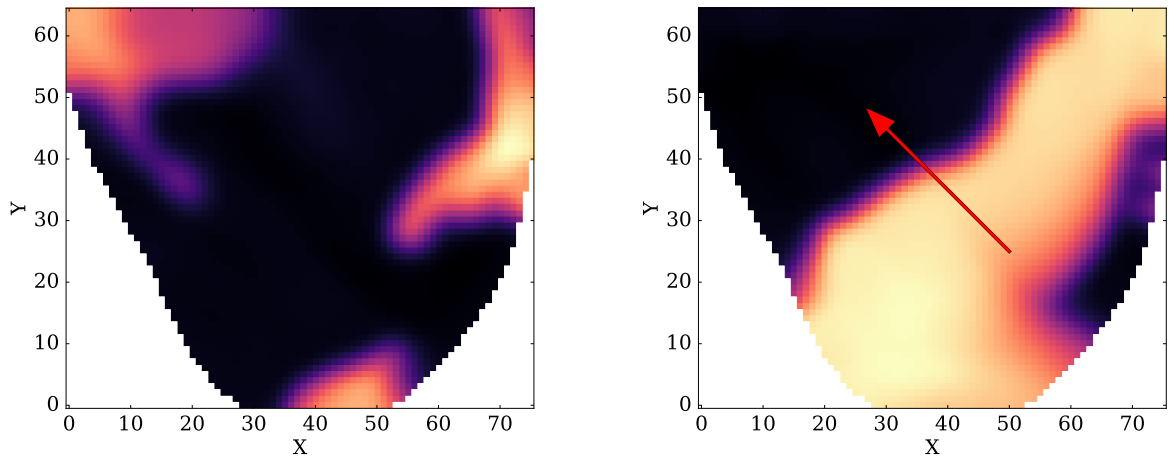


(a) Snapshot of the surface of the V_m at frame 2200. This temporal interval shows a period of high complexity according to Fig. 3.40.

(b) Snapshot of the surface of V_m at frame 3170. This temporal interval indicates a situation with very inhomogeneous complexity with respect to the angle of observation (see Fig. 3.40).

Figure 3.44.: Snapshots of the camera 2 which observes the simulated rabbit heart under an angle of 90 degrees.

3. Results



(a) Snapshot of the surface of V_m at frame 2200. This temporal interval shows a period of high complexity according to Fig. 3.40.

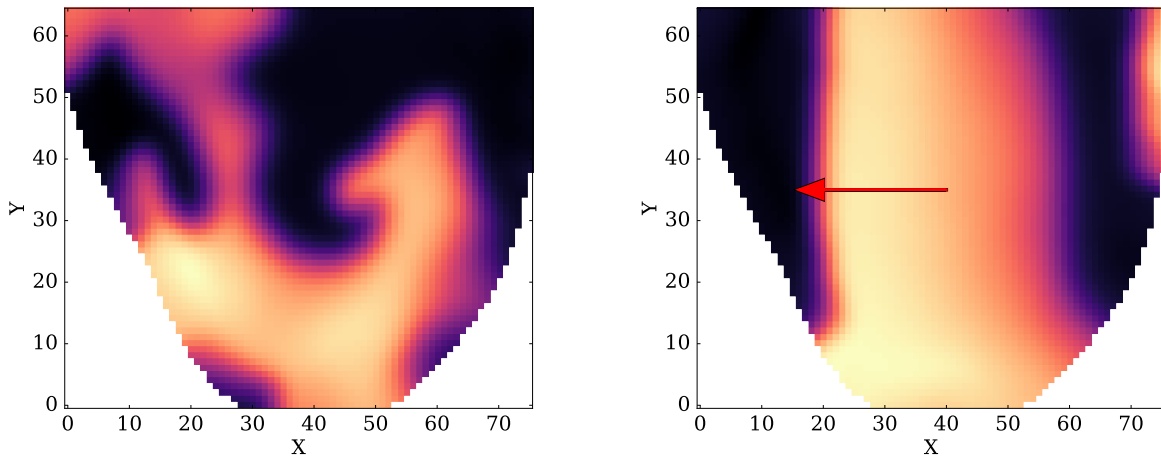
(b) Snapshot of the surface of V_m at frame 3170. This temporal interval indicates a situation with very inhomogeneous complexity with respect to the angle of observation (see Fig. 3.40). The arrow indicates the direction of movement of the (plane) wave.

Figure 3.45.: Snapshots of the camera 3 which observes the simulated rabbit heart under an angle of 180 degrees.

Fig. 3.47 and Fig. 3.48 show the results obtained for the application of PE2D and PE3D to the video. The raw results for the PE2D and PE3D are visible in the background in light colors. As the raw quantities show heavy fluctuations, especially for the PE2D, smoothed versions are added to the figures on top of them. The fluctuations are the result of one property of the excitation waves on the surface: Wave activity which enters or leaves the field of view leads to heavy changes in the number of spatial order patterns. In case of the PE2D the fluctuations are very high. In case of the PE3D there are less fluctuations because of the temporal component of the patterns.

Both measures show heavy dips around frame 3000 in some of the cameras. Camera 2, which looks directly at the spiral, does not lead to a decrease in neither PE2D nor PE3D. For camera 4 a heavy drop in both quantities can be seen. According to PE2D the wave activity in camera 1 and 3 is very similar in complexity while PE3D assigns higher spatiotemporal complexity to camera 1 than to camera 3.

Fig. 3.49 and Fig. 3.50 show the camera dependent results obtained for PSI and NPS. It can be seen that the single scroll wave leads to a constant single phase singularity in camera 2. Furthermore it can be seen that a high level of synchronization is registered on all four cameras.



(a) Snapshot of the surface of V_m at frame 2200. This temporal interval shows a period of high complexity according to Fig. 3.40.

(b) Snapshot of the surface of V_m at frame 3170. This temporal interval indicates a situation with very inhomogenous complexity with respect to the angle of observation (see Fig. 3.40).

Figure 3.46.: Snapshots of camera 4 which observes the simulated rabbit heart under an angle of 0 degrees. The arrow in b) sketches the movement of the (plane) wave.

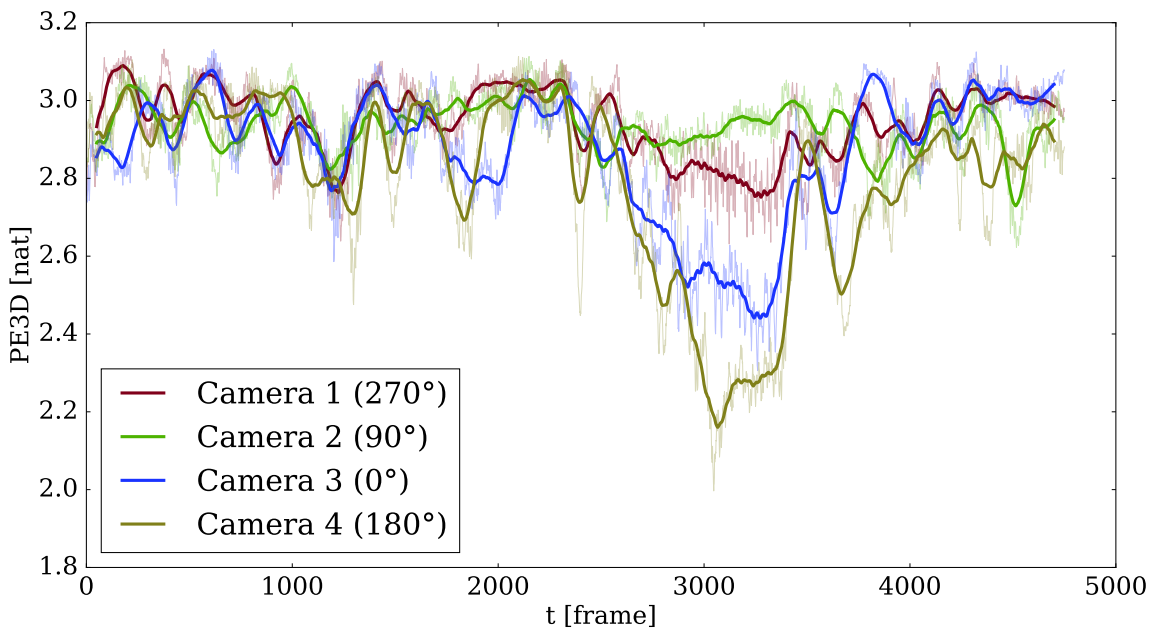


Figure 3.47.: This figure shows the result of the application of the three-dimensional permutation entropy (PE3D) to all four cameras of the simulated data.

3. Results

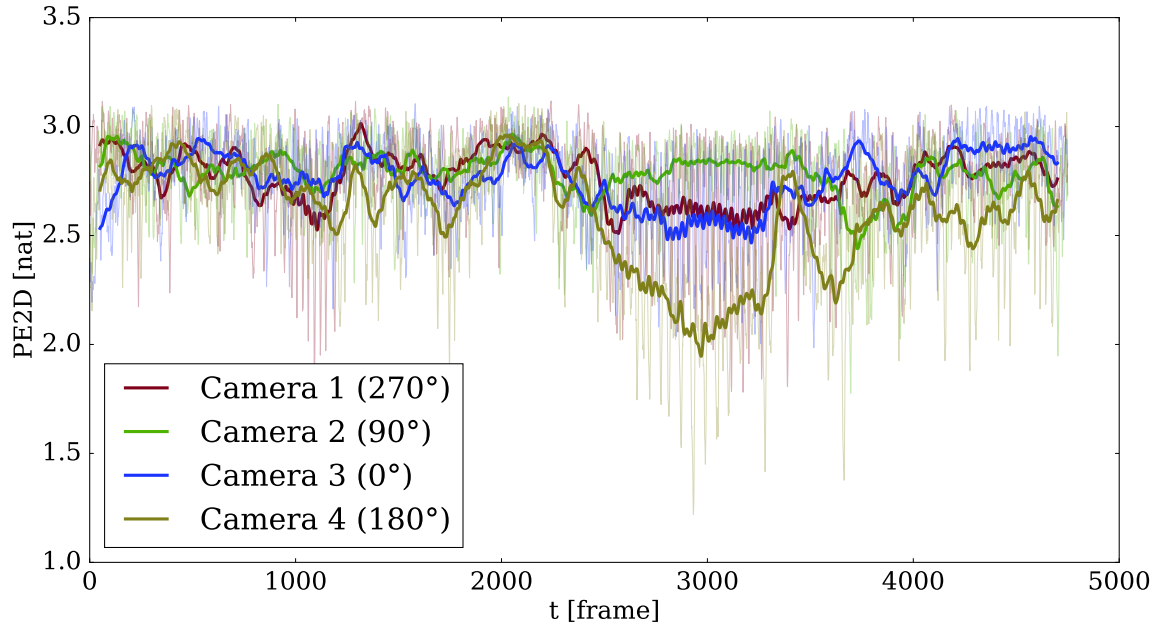


Figure 3.48.: This figure shows the results of applying the two-dimensional permutation entropy (PE2D) to all four cameras of the simulated data.

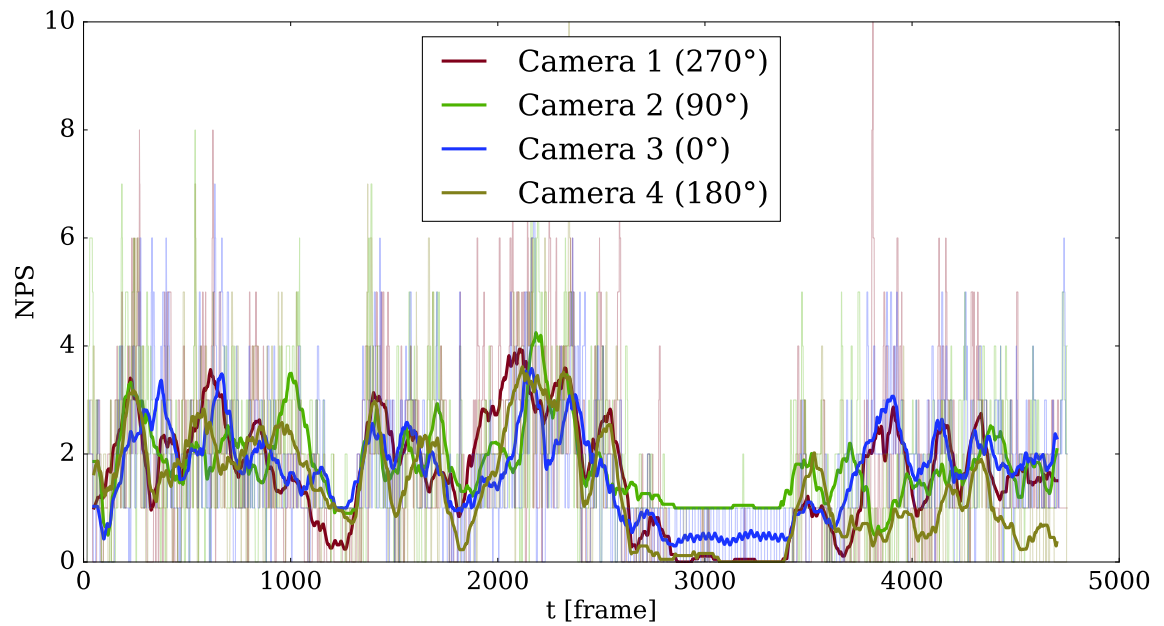


Figure 3.49.: Overview over the results for the application of the phase singularity detection algorithm to the four cameras of the simulation data. The thick lines show the smoothed version of the number of phase singularities (NPS) while the raw data is shown in the background.

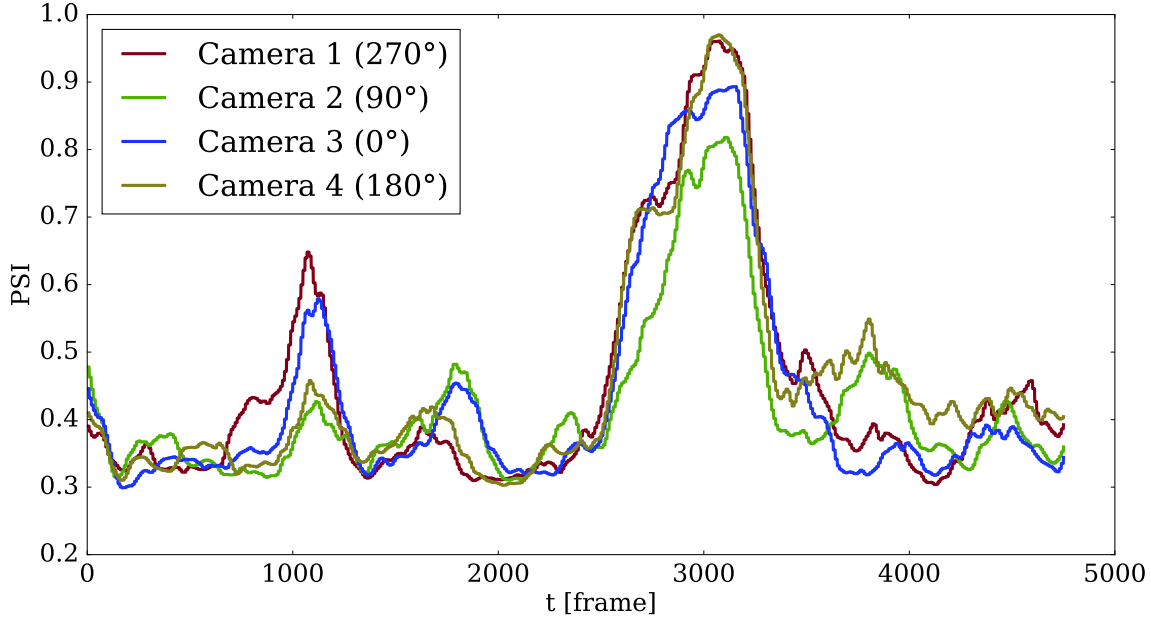


Figure 3.50.: Overview over the results obtained for the Phase Synchronisation Index (PSI) applied to the simulation video data.

3.5.4. Estimation of ECG channels needed for reliable ECG complexity detection

In order to estimate how many ECG electrodes are needed to obtain a reliable correlation between NFIL and PE the following investigation has been carried out: Let $PE_{\varphi}(t)$ be the PE time series belonging to the electrode at angle φ . The initial set of values for φ is $\{0, 1, \dots, 359\}$. For each number of electrodes N there are $n_{el} = \frac{360}{N}$ possible electrode configurations $k \in [0, \frac{360}{N} - 1]$ assuming equidistantly spaced electrodes. For each of these n_{el} configurations the correlation coefficient $C_{N,k}$ between NFIL and the average PE time series is computed:

$$\overline{PE}_k(t) = \frac{1}{N} \sum_{j=1}^N PE_{\varphi_{j,k}}(t) \quad (3.5)$$

$$\varphi_{j,k} = k + (j - 1) \cdot \frac{360}{N} \quad (3.6)$$

Fig. 3.51 and Fig. 3.52 demonstrate how the distribution of $C_{N,k}$ changes under variation of N by showing the average taken over k for each N and the corresponding standard deviations and extreme values.

3. Results

To compare with randomly placed electrodes the mean PE given in Eq. 3.5 has also been computed for 100 different configurations calculated by randomly drawing N values for $\varphi_{j,k}$ without replacement from the set of angles $\{0, 1, \dots, 359\}$. This created distributions for $C_{N,k}$ which are summarized in Fig. 3.53 and Fig. 3.54.

Fig. 3.51 shows the results of this investigation for the first simulation case which was shown in Fig. 3.38 for equidistantly placed electrodes. It can be seen that the average correlation rises quite quickly to a value of 0.78 and converges to a final value of 0.83. This implies that already five electrodes are sufficient to obtain almost the maximum correlation between PE and NFIL in this example.

Although the maximum correlation is lower, the situation is very similar in Fig. 3.52: A correlation value of 0.74 is reached already for 5 electrodes and converges to 0.78. A very prominent difference between Fig. 3.51 and Fig. 3.52 can be seen in the results for small numbers of electrodes: The standard deviation and the range of the extreme cases is much higher for case 95. The reason for this is of course the strong angular dependency of case 95 around frame 3000 which causes a high sensitivity on the positions of the electrodes.

Another interesting finding can be seen in Fig. 3.51. The initial maximum value of 0.68 as indicated by the upper dashed green line (or given in Tab. 3.7) is lower than the value which is reached for large numbers of electrodes. This can be explained by the fact that there cannot be expected to exist an optimal direction from which the PE should be computed. Instead, the angle under which the correlation between PE and NFIL becomes maximal can vary over time and, as in this case, a superposition of PE time series can lead to higher correlations. However, this situation has been found to be not the common case for the simulation cases investigated.

3.5. Angular Dependency of Complexity Fluctuations

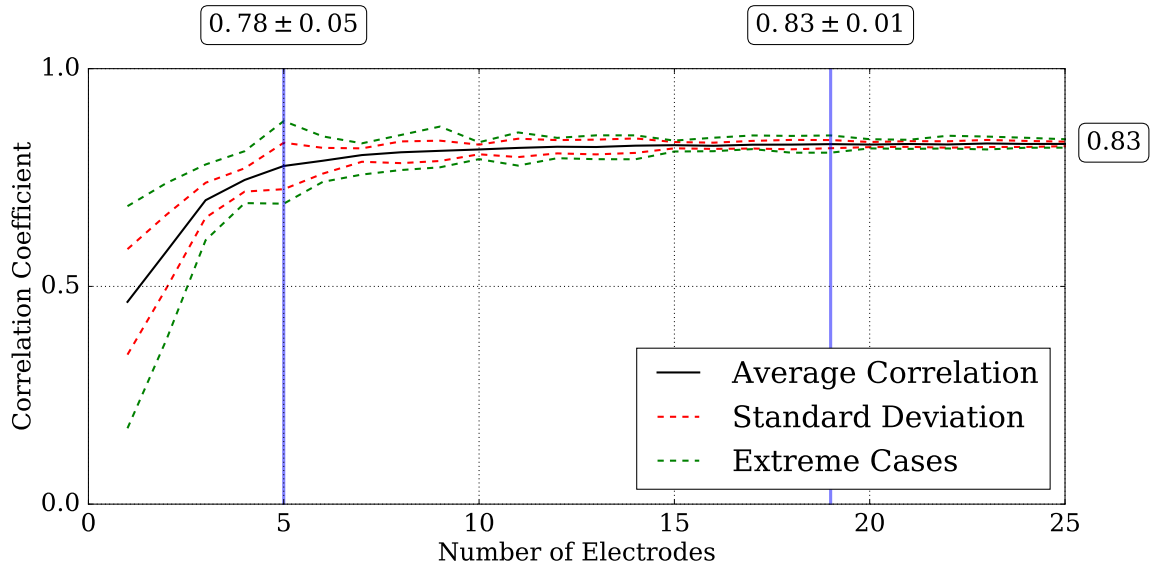


Figure 3.51.: Mean, standard deviation and extreme values of $C_{N,k}$ for the simulation case 50 using equidistantly spaced electrodes.

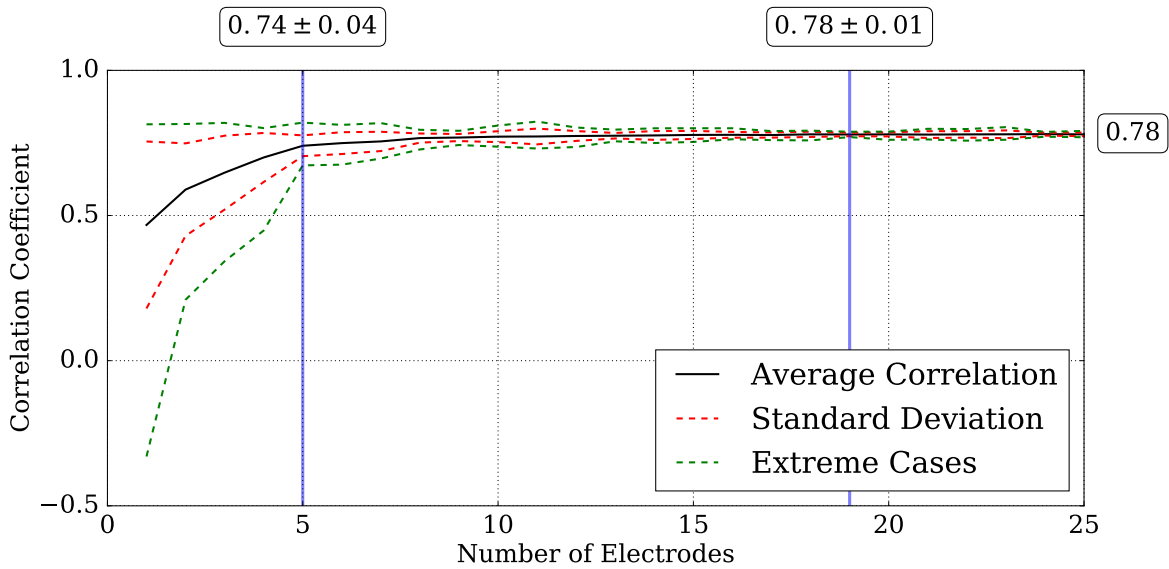


Figure 3.52.: Mean, standard deviation and extreme values of $C_{N,k}$ for the simulation case 95 using equidistantly spaced electrodes.

3. Results

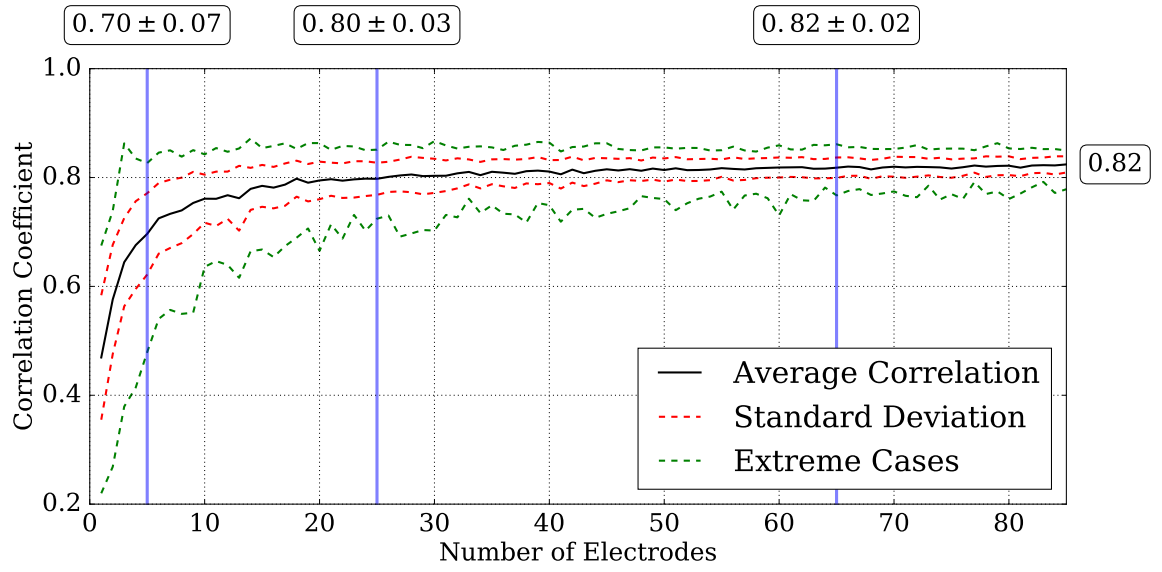


Figure 3.53.: Mean, standard deviation and extreme values of $C_{N,k}$ for the simulation case 50 using randomly spaced electrodes.

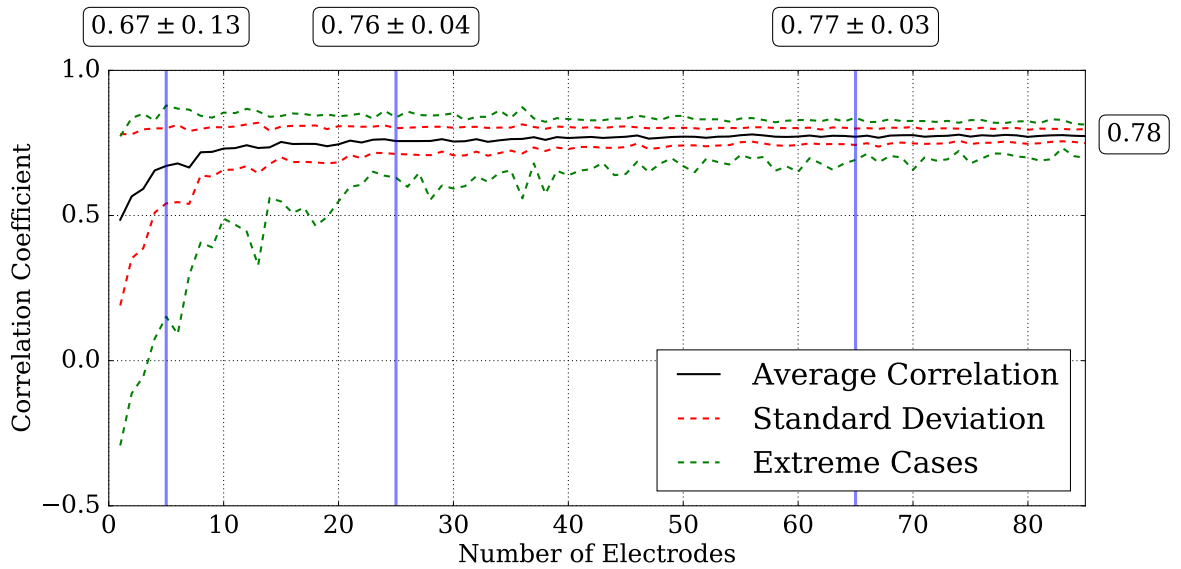


Figure 3.54.: Mean, standard deviation and extreme values of $C_{N,k}$ for the simulation case 95 using randomly spaced electrodes.

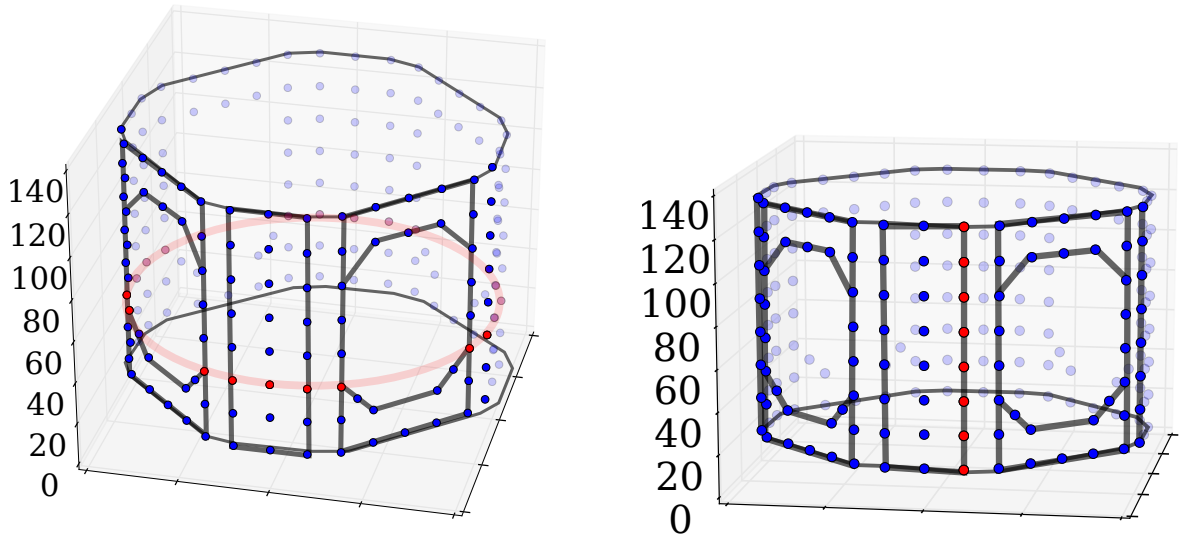
Especially for the second example seen in Fig. 3.54 it can be seen that the standard deviation and range of the extreme cases do not converge as quickly for the random configurations compared to the equidistantly spaced electrode configurations. Furthermore the mean values do not increase strictly monotonously, but are dithering slightly. It is difficult to give a specific recommendation for a number of electrodes in this case. This investigation might possibly include very inefficient constellations and is therefore not very likely to be considered in experimental settings.

3.5.5. Multielectrode Recordings obtained in Inverse ECG experiments

This dataset was acquired in a cooperation with EP Solutions SA by Johannes Schröder-Schetelig and Walther Schulze. The primary aim of this experiment was to evaluate the quality of the inverse ECG method [60]. In this thesis one dataset²⁶ containing a longer recording of a VF is used to demonstrate the angular dependency of fluctuations in complexity in a real experimental setting.

²⁶Segment 2.3 of the ex vivopig experiment on 2016-05-30

3. Results



(a) Sketch of the multi-electrode experimental setup. The figure schematically shows the bath and the plates to which the electrodes are attached. The holes in four of the eight plates are needed to allow for camera recordings. The red circle illustrates the level of height $z = 48$ which has been used to extract electrodes for the analysis carried out in Sec. 3.5.5.

(b) Another sketch of the multi-electrode experimental setup. The electrodes marked in red have been used to carry out the analysis of the effect of height on the complexity of the ECG discussed in Sec. 3.5.5.

Figure 3.55.: The setup of the electrodes during the multi-electrode experiments.

For analysing the multi-electrode data obtained in the inverse ECG experiments all data channels were extracted given a specific height. As it can be seen in Fig. 3.55 the total number of available electrodes is different for some heights. This has technical reasons in the original setup, as there had to be sufficient space for the camera views which is assured by the holes in each plate. The ECG time series for this experiment were preprocessed with a Butterworth bandpass filter with a low cutoff frequency of 0.5 Hz and a high cutoff frequency of 45 Hz as there was a difference in the signal to noise ratio between the channels.

3.5. Angular Dependency of Complexity Fluctuations

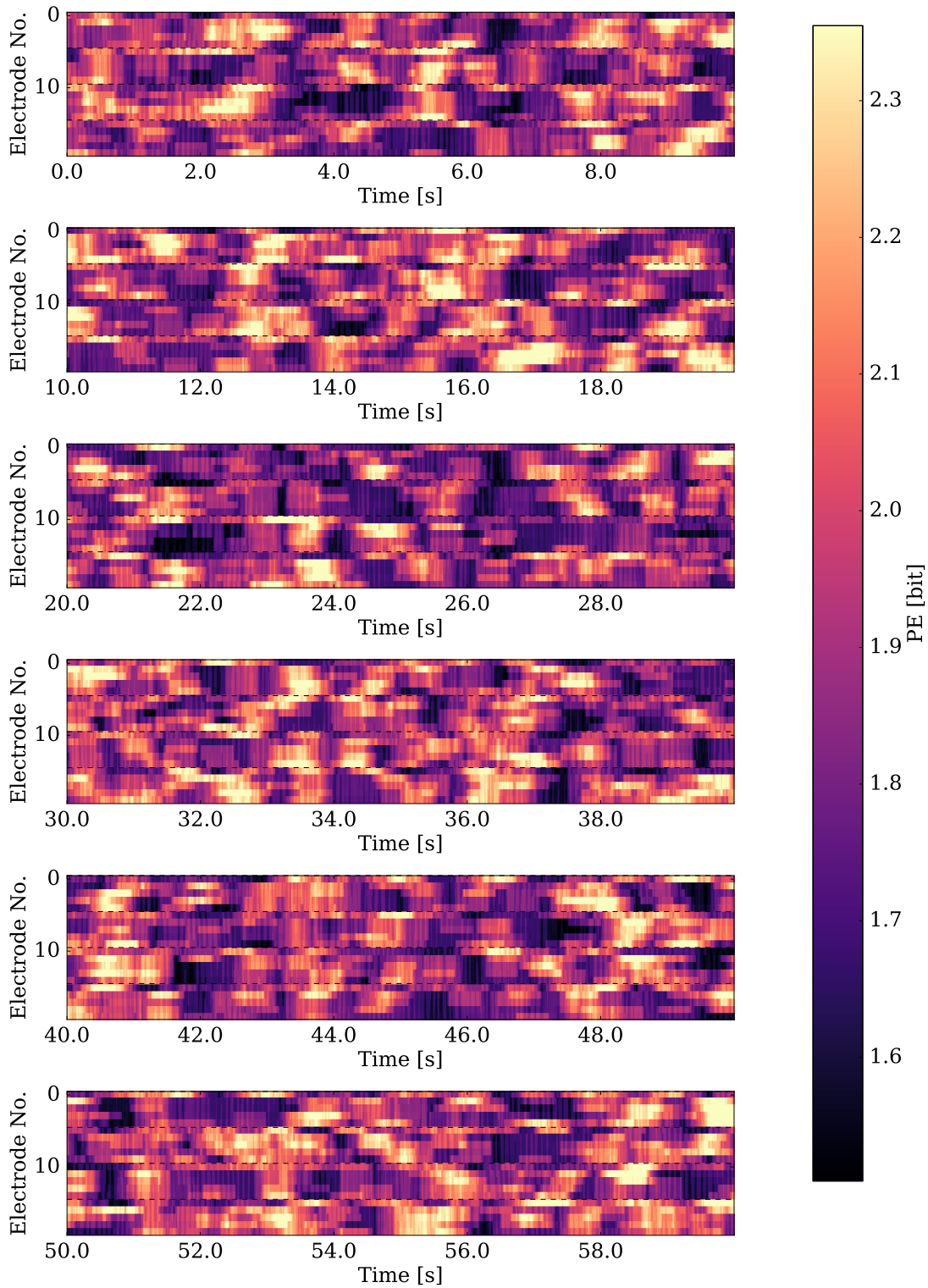


Figure 3.56.: A 60s excerpt for a VF of a pig heart recorded with the multielectrode setup as described in Sec. 3.5.5. The rows are successive sections of the PE time series. The dashed black lines mark the separation of the plates as depicted in Fig. 3.55. The ECG recordings shown here are extracted from height $z = 48$ at which each plate contained five electrodes. 123

3. Results

Fig. 3.56 shows an overview over the time series of the permutation entropy obtained for height $z = 48$. For this height 5 electrodes were available per plate (see Fig. 3.55a). The dashed lines mark the separation between consecutive sequences of 5 electrodes due to the camera hole. This separation is also visible in a qualitative change in the patterns. It can be seen clearly that in many cases laminar phases are occurring for periods of different lengths which are in most cases not visible in all of the ECG channels. This excerpt shows a section with a duration of 60 s in ten second segments for each row.

An obvious effect is that the variation in entropy for a specific time point is much less between electrodes lying on the same plate as the variation between electrodes from different plates. This is due to the fact that the observed angle of electrical activity is much more different between the plates than within the plates (see Fig. 3.56).

The patterns observed in this figure are very similar to the patterns obtained in the 3D simulations discussed in Sec. 3.5: Laminar phases arise for short time periods (approximately 0.1 s to 1.5 s) which are in many cases visible on only one electrode plate.

Comparison of two ECG channels

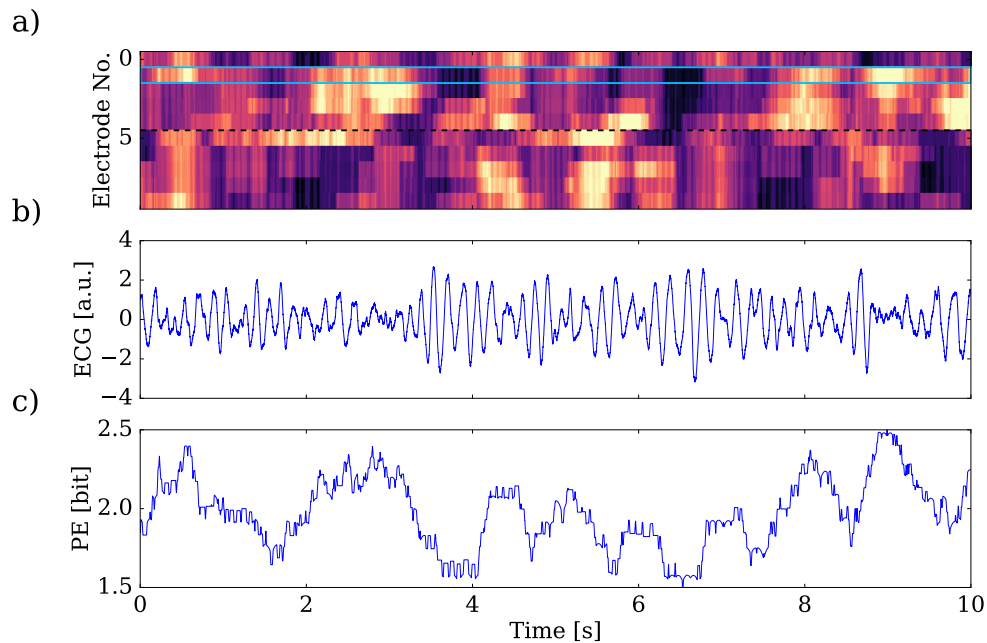


Figure 3.57.: An excerpt from Fig. 3.56 showing only the first ten seconds and the PE of the first ten electrodes in (a). The ECG from electrode No. 1 which is highlighted in blue in the figure is displayed in (b). The same color palette as in Fig. 3.56 has been used.

In order to illustrate the effect on single ECG time series, two channels from Fig. 3.56 have been extracted and plotted in Fig. 3.57 and Fig. 3.58. It can be seen that several laminar phases which are visible in channel 1 which is displayed in Fig. 3.57 are not visible in channel 6 (Fig. 3.58). E.g. the two very prominent laminar phases at approximately 4s and 6.5s which are visible in Fig. 3.57 are not visible in Fig. 3.58.

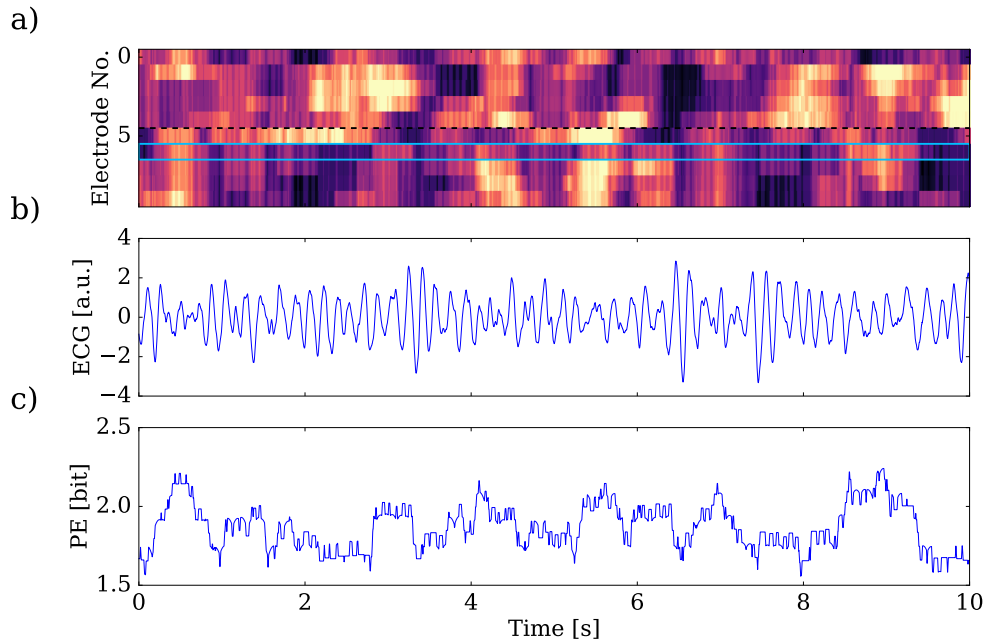


Figure 3.58.: An excerpt from Fig. 3.56 showing only the first ten seconds and the PE of the first ten electrodes in (a). The ECG from electrode No. 6 which is highlighted in blue in the figure is displayed in (b). The same color palette as in Fig. 3.56 has been used.

Effect of the height of the electrode on the VF complexity

The effect of the height of the electrode is demonstrated in Fig. 3.59. For this figure the electrodes which were taken to compute the permutation entropies are located as it is sketched in Fig. 3.55b. This figure suggests that there is no strong dependency on the height of the electrode, because in many cases, laminar phases and very complex phases are visible for most electrodes at different heights.

3. Results

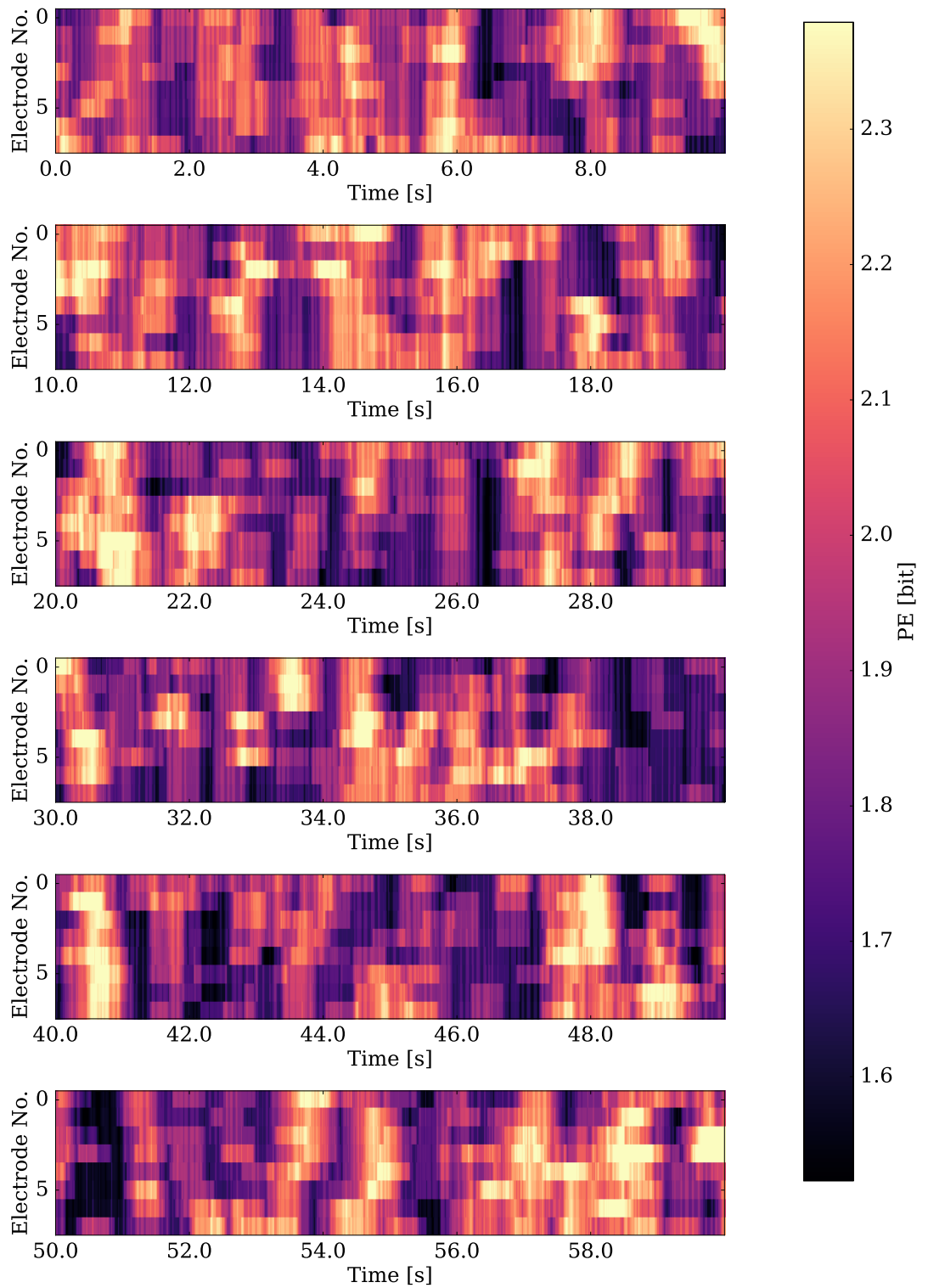


Figure 3.59.: Scan of the vertical direction (z) of the pig heart VF using the multielectrode ECG setup. The configuration is shown in Fig. 3.55b.

3.5.6. Summary and Conclusion

This section about fluctuations in ECG complexity in 3D Fenton-Karma simulations on a realistic rabbit heart geometry can be summarized as follows:

- ECGs calculated for simulations of electrical wave propagation in cardiac systems show intermittent complexity variations similar to those observed for real hearts. These complexity variations can be detected using permutation entropy.
- There is a correspondence between the permutation entropy and the number of phase filaments in the system. The correlation coefficient between both quantities reaches maximum values between 0.51 and 0.81 in the simulations considered here and is predominantly significant in a surrogate test. These correlations imply that a lower complexity in the ECG signal is likely to stem from a spatiotemporal state with fewer rotors.
- There can be a strong dependency of the correspondence described in the last point on the angle of observation of the ECG. This was analysed using surface projections similar to optical imaging data. This analysis made clear that the heterogeneous situation was due to the fact that the ECG as measured from regions close to one rotation center has a much higher complexity than ECGs from parts where the system is driven by plane waves emitted from that rotor.
- It was shown that the dominant low complexity phases can be detected on the surface by utilizing very different spatiotemporal properties. Two- and three-dimensional permutation entropies seem to be more sensitive to the specific excitation patterns while the phase singularities and the phase synchronisation index quantify more general properties of the medium. The phase synchronisation index gives the most straight-forward interpretation here and is not influenced by the spiral on camera two.
- The usage of multiple ECG electrodes for the detection of laminar phases has been studied and suggests a set of at least five equidistantly spaced electrodes.
- The effect of the angular dependency of ECG complexity has been shown in ECGs from an ex vivo experiment.

Some additional notes and clarifications which could be helpful for the design of future experiments:

- It should be emphasized that although the laminar phases are likely to correspond to states with a low number of vortices the apparent laminarity in the ECG is due to the plane waves produced by it. The rotor itself looks quite complex in

3. Results

proximate ECG electrodes.

- The simulation case 95 is an example for a very heterogeneous situation. The mean PE time series used in the analysis of the previous section can in the future probably be replaced by a set of very specific detection criteria for low complexity. One idea would be decision trees using the PE values of multiple electrodes as features. A detailed investigation of the possible heterogeneous constellations is a prerequisite for that.

4. Discussion and Outlook

This chapter will briefly summarize the findings from Chapter 3. The discussion and outlook will follow afterwards.

4.1. Summary

In this thesis complexity fluctuations of the cardiac dynamics during ventricular fibrillation were investigated with the aim of better understanding the disease and for developing and improving therapeutic methods. This chapter will summarize the most important results from the preceding chapter and discuss implications for this field of research. Detailed summaries of the individual sections of the results chapters can be found in Sec. 3.1.1, Sec. 3.2.3, Sec. 3.3.8, Sec. 3.4.4, and Sec. 3.5.6.

Short-timescale complexity fluctuations in the ECG time series during VF were shown for different species and realistic simulations of excitable media. These fluctuations were quantified using permutation entropy, wavelet entropy, power spectral entropy, windowed standard deviation, and wavelet energy. It was found that there is a high correlation among most of the methods, except for power spectral entropy which seems to suffer from short window lengths needed for this analysis. Statistical properties of the laminar phases were studied and an algorithm for efficient detection of laminar phases was proposed and evaluated.

Using data from numerical 3D-simulations on a realistic rabbit heart geometry it was shown that the complexity fluctuations are significantly correlated to the number of phase filaments in the medium which are a direct indicator of the number of rotation centers of electrical excitation waves. This analysis also revealed that the effect of the wave propagation on the ECG may strongly depend on the direction under which the ECG is recorded. An in-depth analysis of a particularly heterogeneous period using simulated camera data highlighted that rotors produce complex patterns in proximate electrodes. Their wave emission, however, causes synchronisation of remote areas in the tissue which appear very regular when recorded with ECG electrodes. In order to have a sufficiently high correlation of NFIL and PE a parameter scan showed that at least five equidistantly spaced electrodes should be used. Data from an ex vivo experiment with

4. Discussion and Outlook

a pig using a multielectrode measurement setup revealed that an angular dependency of the complexity fluctuations can also be detected experimentally using PE.

An experimental protocol was established to experimentally test whether shocks into more regular periods in the ECG improve defibrillation success at a constant energy. Ex vivo experiments with eight rabbits and three pigs showed only anecdotal periods with an improvement using this PE dependent intervention strategy. However, some conceptual and technical issues were identified and analysed with important implications for future experiments. These will be discussed at the end of this section. The shock protocol using permutation entropy or other complexity measures has been included in a patent application. An application of random forests to predict the shock result using complexity features of the experimental ECGs before the shock did only yield limited insight and suffers heavily from too small amounts of data.

A small series of experiments was carried out to test for the possibility to use fluorescence signals for complexity triggered pacing protocols. This procedure did not lead to results favoring a specific complexity regime as measured by a spatially resolved PE estimated from the surface activity. The fluorescence data was analysed employing multiple methods for quantifying spatiotemporal dynamics. Also multi-dimensional variants of the permutation entropy were employed to video data and compared to the phase synchronisation index and the number of phase singularities. The complexity of the ECG signal from a single ECG direction shows a partial correlation with spatiotemporal complexity measures which is not strong enough to conclude a significant association. This especially holds for the number of phase singularities measured on the surface of the tissue.

The main findings can be summed up as follows:

- The application of PE to sliding windows of ECG time series is a robust method for quantifying short-timescale complexity fluctuations.
- The PE time series has a significant correlation with the number of rotors in 3D-simulations on a realistic rabbit heart geometry and this correlation can be highly dependent on the angle of observation.
- In a series of ex vivo experiments with pig and rabbit hearts only anecdotal evidence for an increase in success probability for low energy antifibrillation pacing into laminar phases over more complex phases at a constant energy was found.
- The correspondence between spatiotemporal complexity derived from fluorescence imaging and the complexity derived from the ECG measured for a single direction is not high enough to conclude a significant association.

4.2. Discussion and Outlook

The first research question brought up in the introduction in Sec. 1.6 focused on the quantification of complexity fluctuations in the ECG during VF. From the analysis carried out in this thesis it becomes clear that very different approaches can be used and share a lot of similarities. From speed considerations, simplicity in implementation and robustness, PE can definitely be recommended for practical applications which possibly have to analyse the data in real-time. The direct accessibility to the order pattern statistics estimated during calculation of the PE turned out to be an advantage and led to the construction of an even faster algorithm for detecting laminar phases. The PCA entropy on the other hand proved to be an intuitively interpretable measure for the extent of the set of reconstructed states which comes at the drawback of longer computation times. A simple definition of a laminar phase using a threshold for the PE based on mean and standard deviation was given initially. A more systematic definition of a laminar phase from the patterns visible in the ECG was developed later using the calibration of the threshold using a sine signal with the same frequency as the VF.

This quantification of complexity fluctuations provided the basis for the use in experimental protocols.

The phenomenological definitions of laminar phases were supported using data from 3D-simulations of the heart. The initial observation of a partial correlation of the complexity measures with the number of phase filaments was precised with a more detailed analysis using a realistic ECG definition. The significant correlation at decent values for the Pearson correlation coefficient indicates strongly that there is an association between the number of scroll waves in the heart and the ECG complexity fluctuations. This generally suggests that the spatiotemporal complexity during VF can be estimated using information from ECGs. The angular dependent complexity analysis clearly showed that it can be precarious to rely on single ECG channels. Especially the possibility of very inhomogenous complexity patterns that belong to very simple spatiotemporal configurations can lead to misdetections of low complexity states. This angular effect has not only been shown for simulation data, but can be also seen in data from ex vivo multielectrode measurements with pig hearts. This result has two main implications: Firstly, it is very desirable to use multiple measurement directions for the ECG for the detection of laminar phases. Technical applications with a real-time estimation of ECG complexity from multiple electrodes can be considered to benefit even more from fast algorithms like the one presented in this thesis. Secondly, the detection of laminar phases from multiple ECG directions cannot be reduced to the detection of the detection of a laminar phase on each channel simultaneously. Instead one branch of future research on laminar phases should concentrate on performing the angular complexity analysis presented here on more simulated hearts for strengthening the understanding of the associations between specific patterns of angular dependency and the corresponding spatiotemporal dynamics. This whole framework might in the future lead to a very

4. Discussion and Outlook

sensitive and specific method for the detection low complexity states using ECGs. It can be concluded that the analysis presented here leads to a deeper insight into the relation between complexity fluctuations of the ECG and the spatiotemporal organization during VF.

From the comprehensive analysis of optical imaging data during VF, from which an exemplary dataset was discussed in detail in this thesis, a reliable association between complexity measured on the surface of the heart and the complexity of the ECG signal cannot be concluded. This supports a previous assumption that the surface simply might not contain enough information about the full state of the system. Especially the prevalent cases of a plane wave entering or leaving the field of view and waves emerging from below the surface are only covered partially by common measures for the complexity of excitable media. Furthermore, the results are also in line with the findings obtained for the simulation data. The complexity was calculated only for one direction from the ECG and might contain only limited information. Here again the implication holds that future measurements should make use of multiple ECG directions. Additionally new methods currently under development like ultrasound imaging and optical coherence tomography will likely enable the tracking of phase filaments experimentally in the whole medium.

Based on the series of ex vivo experiments the third research question from Sec. 1.6 can not be answered positively yet. Although some anecdotal periods of increased success probability for laminar phases were found, the majority of experiments did not show a reliable improvement. One important observation from all ex vivo experiments with rabbits described here is that it was difficult to induce stable VF episodes without a cryoablation zone. Additionally the VF episodes became more stable when the hearts became more ischemic. This could suggest that the VF episodes found in ex vivo experiments with rabbit hearts are generally not very complex, so that it is difficult to see large differences between more complex periods and less complex periods during VF. Another important explanation why no big difference in probabilities of shock outcome could be detected, follows directly from the analyses of complexity in ECG time series from 3D-simulations of the heart presented here. The result that a low number of rotors can lead to a very heterogenous situation of complexity leads to the conclusion that the ECG should be recorded from multiple directions in experiments to reliably detect laminar phases. Also the investigation of the dependency of the correlation between phase filaments and PE strongly suggests that at least five equidistantly spaced electrodes should be used for shocks triggered on specific PE periods.

At the time of finishing this thesis, the experimental procedure for an ex vivo experiment using an eight electrode measurement system has already been set up and the experiment is in progress.

5. Bibliography

- [1] *Mediasim Framework*. Accessed: 2017-02-02. URL: <http://mediasim.org>.
- [2] *MultiRecorder, a multiple-camera recording and analysis software*. Accessed: 2014-10-06. URL: <http://www.bmp.ds.mpg.de/multirecorder.html>.
- [3] P. S. Addison, J. N. Watson, G. R. Clegg, M. Holzer, F. Sterz, and C. E. Robertson. Evaluating arrhythmias in ECG signals using wavelet transforms. *IEEE Engineering in Medicine and Biology Magazine*, 19(5):104–109, 2000.
- [4] D. Albanese, R. Visintainer, S. Merler, S. Riccadonna, G. Jurman, and C. Furlanello. mlpy: Machine learning python, 2012. [arXiv:1202.6548](https://arxiv.org/abs/1202.6548).
- [5] J. Amigó. *Permutation Complexity in Dynamical Systems*. Springer Series in Synergetics. Springer Berlin Heidelberg, Berlin, Heidelberg, 2010.
- [6] C. F. Babbs, W. A. Tacker, J. F. VanVleet, J. D. Bourland, and L. A. Geddes. Therapeutic indices for transthoracic defibrillator shocks: effective, damaging, and lethal electrical doses. *American Heart Journal*, 99(6):734–738, 1980.
- [7] J. Baglama and L. Reichel. Augmented Implicitly Restarted Lanczos Bidiagonalization Methods. *SIAM Journal Scientific Computing*, 27(1):19–42, 2005.
- [8] J. Baglama and L. Reichel. Restarted block Lanczos bidiagonalization methods. *Numerical Algorithms*, 43(3):251–272, 2007.
- [9] P. Baldi, S. Brunak, Y. Chauvin, C. A. Andersen, and H. Nielsen. Assessing the accuracy of prediction algorithms for classification: an overview. *Bioinformatics*, 16(5):412–424, 2000.
- [10] C. Bandt and B. Pompe. Permutation Entropy: A Natural Complexity Measure for Time Series. *Physical Review Letters*, 88(17):174102, 2002.
- [11] G. H. Bardy, T. D. Ivey, M. D. Allen, G. Johnson, R. Mehra, and H. L. Greene. A prospective randomized evaluation of biphasic versus monophasic waveform pulses on defibrillation efficacy in humans. *Journal of the American College of Cardiology*,

5. Bibliography

- 14(3):728–733, 1989.
- [12] D. Barkley. Barkley model. *Scholarpedia*, 3(11):1877, 2008. revision #91029.
- [13] D. Barkley. A model for fast computer simulation of waves in excitable media. *Physica D*, 49:61–70, 1991.
- [14] D. Barrett. *Cardiac Care: An Introduction for Healthcare Professionals*. John Wiley & Sons, August 2006. Google-Books-ID: JARhIV6C3xcC.
- [15] A. Behrend, P. Bittihn, and S. Luther. Predicting unpinning success rates for a pinned spiral in an excitable medium. In *2010 Computing in Cardiology*, pages 345–348, 2010.
- [16] R. M. Bell, M. M. Mocanu, and D. M. Yellon. Retrograde heart perfusion: the langendorff technique of isolated heart perfusion. *Journal of Molecular and Cellular Cardiology*, 50(6):940–950, 2011.
- [17] P. Bittihn, G. Luther, E. Bodenschatz, V. Krinsky, U. Parlitz, and S. Luther. Far field pacing supersedes anti-tachycardia pacing in a generic model of excitable media. *New Journal of Physics*, 10(10):103012, 2008.
- [18] L. Breiman. Random Forests. *Machine Learning*, 45(1):5–32, 2001.
- [19] L. Breiman, J. Friedman, C. J. Stone, and R. A. Olshen. *Classification and Regression Trees*. Taylor & Francis Ltd, New York, 1984.
- [20] D. S. Broomhead and G. P. King. Extracting qualitative dynamics from experimental data. *Physica D*, 20(2):217–236, 1986.
- [21] S. Butterworth. On the theory of filter amplifiers. *Wireless Engineer*, 7:536–541, 1930.
- [22] T. Bánsági and O. Steinbock. Three-dimensional spiral waves in an excitable reaction system: Initiation and dynamics of scroll rings and scroll ring pairs. *Chaos*, 18(2):026102, 2008.
- [23] E. M. Cherry and F. Fenton. Visualization of spiral and scroll waves in simulated and experimental cardiac tissue. *New Journal of Physics*, 10:125016, 2008.
- [24] B. Chicote, U. Irusta, R. Alcaraz, J. J. Rieta, E. Aramendi, I. Isasi, D. Alonso, and K. Ibarguren. Application of Entropy-Based Features to Predict Defibrillation Outcome in Cardiac Arrest. *Entropy*, 18(9):313, 2016.

- [25] J. Christoph. Intramural visualization of scroll waves in the heart. 2014.
- [26] R. H. Clayton, E. A. Zhuchkova, and A. V. Panfilov. Phase singularities and filaments: Simplifying complexity in computational models of ventricular fibrillation. *Progress in Biophysics and Molecular Biology*, 90(1–3):378–398, 2006.
- [27] J. Cohen. Statistical power analysis for the behavioral sciences (second ed.), 1988.
- [28] J. Eason and N. Trayanova. Phase Singularities and Termination of Spiral Wave Reentry. *Journal of Cardiovascular Electrophysiology*, 13(7):672–679, 2002.
- [29] I. R. Efimov, W. Li, and A. Janardhan. Methods and devices for three-stage ventricular therapy, 2014. U.S. Classification 607/5, 607/14; International Classification A61N1/368, A61N1/362, A61N1/39; Cooperative Classification A61N1/3918, A61N1/3956, A61N1/3906, A61N1/3981, A61N1/3624, A61N1/395.
- [30] B. Efron. Bootstrap Methods: Another Look at the Jackknife. In S. Kotz and N. L. Johnson, editors, *Breakthroughs in Statistics*, Springer Series in Statistics, pages 569–593. Springer New York, 1992. DOI: 10.1007/978-1-4612-4380-9_41.
- [31] B. Efron. Second Thoughts on the Bootstrap. *Statistical Science*, 18(2):135–140, 2003.
- [32] F. H. Fenton, E. M. Cherry, and L. Glass. Cardiac arrhythmia. *Scholarpedia*, 3(7):1665, 2008.
- [33] F. Fenton and A. Karma. Vortex dynamics in three-dimensional continuous myocardium with fiber rotation: Filament instability and fibrillation. *Chaos*, 8(1):20–47, 1998.
- [34] F. H. Fenton and E. M. Cherry. Models of cardiac cell. *Scholarpedia*, 3(8):1868, August 2008.
- [35] F. H. Fenton, E. M. Cherry, H. M. Hastings, and S. J. Evans. Multiple mechanisms of spiral wave breakup in a model of cardiac electrical activity. *Chaos*, 12(3):852–892, 2002.
- [36] F. H. Fenton, S. Luther, E. M. Cherry, N. F. Otani, V. Krinsky, A. Pumir, E. Boddenschatz, and R. F. Gilmour. Termination of Atrial Fibrillation Using Pulsed Low-Energy Far-Field Stimulation. *Circulation*, 120(6):467–476, 2009.
- [37] R. Fisch, J. Gravner, and D. Griffeath. Metastability in the Greenberg-Hastings Model. *The Annals of Applied Probability*, 3(4):935–967, 1993.

5. Bibliography

- [38] V. Fuster, L. E. Rydén, D. S. Cannom, H. J. Crijns, A. B. Curtis, K. A. Ellenbogen, J. L. Halperin, J.-Y. L. Heuzey, G. N. Kay, J. E. Lowe, S. B. Olsson, E. N. Prystowsky, J. L. Tamargo, S. Wann, A. T. F. Members, S. C. Smith, A. K. Jacobs, C. D. Adams, J. L. Anderson, E. M. Antman, J. L. Halperin, S. A. Hunt, R. Nishimura, J. P. Ornato, R. L. Page, B. Riegel, E. C. f. P. Guidelines, S. G. Priori, J.-J. Blanc, A. Budaj, A. J. Camm, V. Dean, J. W. Deckers, C. Despres, K. Dickstein, J. Lekakis, K. McGregor, M. Metra, J. Morais, A. Osterspey, J. L. Tamargo, and J. L. Zamorano. ACC/AHA/ESC 2006 Guidelines for the Management of Patients With Atrial Fibrillation. *Circulation*, 114(7):e257–e354, 2006.
- [39] A. L. Goldberger, L. A. N. Amaral, L. Glass, J. M. Hausdorff, P. C. Ivanov, R. G. Mark, J. E. Mietus, G. B. Moody, C.-K. Peng, and H. E. Stanley. PhysioBank, PhysioToolkit, and PhysioNet. *Circulation*, 101(23):e215–e220, 2000.
- [40] A. P. M. Gorgels. *Electrocardiography*, pages 43–77. Springer London, London, 2007.
- [41] S. D. Greenwald. *The development and analysis of a ventricular fibrillation detector*. Thesis, Massachusetts Institute of Technology, 1986.
- [42] A. Hamzei, T. Ohara, Y. H. Kim, M. H. Lee, O. Voroshilovski, S.-F. Lin, J. N. Weiss, P.-S. Chen, and H. S. Karagueuzian. The role of approximate entropy in predicting ventricular defibrillation threshold. *Journal of Cardiovascular Pharmacology and Therapeutics*, 7(1), 2002.
- [43] T. Hastie, R. Tibshirani, and J. J. H. Friedman. *The elements of statistical learning*, volume 1. Springer New York, 2001.
- [44] A. Herlin and V. Jacquemet. Reconstruction of phase maps from the configuration of phase singularities in two-dimensional manifolds. *Physical Review E*, 85(5):051916, 2012.
- [45] R. K. Hobbie and B. J. Roth. *Intermediate Physics for Medicine and Biology*. Springer, April 2015.
- [46] T. Horie. Approximate entropy of electrocardiogram signals in atrial fibrillation. *Rinsho Byori*, 61(10):893–899, 2013.
- [47] D. Hornung. Cardiac Arrhythmia Termination on the Vascular and Organ Scale. 2014.
- [48] A. N. Iyer and R. A. Gray. An experimentalist’s approach to accurate localization of phase singularities during reentry. *Annals of Biomedical Engineering*, 29(1):47–59, 2001.

- [49] G. James, D. Witten, T. Hastie, and R. Tibshirani. *An Introduction to Statistical Learning: With Applications in R*. Springer Publishing Company, Incorporated, 2014.
- [50] M. Jenckel. Parameter estimation and critical point detection based on observed time series. Master's thesis, Georg-August Universität Göttingen, 2014.
- [51] Z. A. Jiménez, Z. Zhang, and O. Steinbock. Electric-field-controlled unpinning of scroll waves. *Physical Review E*, 88(5), 2013.
- [52] D. L. Jones and G. J. Klein. Ventricular fibrillation: The importance of being coarse? *Journal of Electrocardiology*, 17(4):393–399, 1984.
- [53] B. H. Kenknight, W. Hsu, Y. Lin, and J. Jones. Method and apparatus for treating cardiac arrhythmia using electrogram features, 2000. U.S. Classification 607/5; International Classification A61N1/39; Cooperative Classification A61N1/3962; European Classification A61N1/39M2.
- [54] T. Kreuz. Measures of neuronal signal synchrony. *Scholarpedia*, 6(12):11922, 2011.
- [55] V. I. Krinsky and K. I. Agladze. Interaction of rotating waves in an active chemical medium. *Physica D*, 8(1–2):50–56, 1983.
- [56] K. W. Kuelz, P.-W. Hsia, R. M. Wise, R. Mahmud, and R. J. Damiano. Integration of absolute ventricular fibrillation voltage correlates with successful defibrillation. *IEEE Transactions on Biomedical Engineering*, 41(8):782–791, 1994.
- [57] W. Li, C. M. Ripplinger, Q. Lou, and I. R. Efimov. Multiple Monophasic Shocks Improve Electrotherapy of Ventricular Tachycardia in a Rabbit Model of Chronic Infarction. *Heart Rhythm*, 6(7):1020, 2009.
- [58] C.-H. Luo. Luo-Rudy models. *Scholarpedia*, 6(10):6220, October 2011.
- [59] S. Luther, F. H. Fenton, B. G. Kornreich, A. Squires, P. Bittihn, D. Horning, M. Zabel, J. Flanders, A. Gladuli, L. Campoy, E. M. Cherry, G. Luther, Gisa Hasenfuss, V. I. Krinsky, A. Pumir, R. F. Gilmour Jr, and E. Bodenschatz. Low-energy control of electrical turbulence in the heart. *Nature*, 475:235–239, 2011.
- [60] R. S. MacLeod and D. H. Brooks. Recent progress in inverse problems in electrocardiology. *IEEE Engineering in Medicine and Biology Magazine*, 17(1):73–83, 1998.
- [61] M. Malik. Heart rate variability. *Annals of Noninvasive Electrocardiology*,

5. Bibliography

- 1(2):151–181, 1996.
- [62] D. R. Martin, C. G. Brown, and R. Dzwonczyk. Frequency analysis of the human and swine electrocardiogram during ventricular fibrillation. *Resuscitation*, 22(1):85–91, 1991.
- [63] J. Mingers. An Empirical Comparison of Pruning Methods for Decision Tree Induction. *Machine Learning*, 4(2):227–243, 1989.
- [64] J. D. Murray. *Mathematical Biology. II: Spatial Models and Biomedical Applications*. Springer, 3 edition, 2003.
- [65] L. J. L. Naresh Bajaj. Fibrillation Complexity as a Predictor of Successful Defibrillation. In *2005 27th Annual International Conference IEEE Engineering in Medicine and Biology (EMBC)*, pages 768–71, 2005.
- [66] J. T. Niemann, D. Burian, D. Garner, and R. J. Lewis. Monophasic versus biphasic transthoracic countershock after prolonged ventricular fibrillation in a swine model. *Journal of the American College of Cardiology*, 36(3):932–938, 2000.
- [67] H. Olkkonen. Computation of hilbert transform via discrete cosine transform. *Journal of Signal and Information Processing*, 01(01):18–23, 2010.
- [68] S. V. Pandit and J. Jalife. Rotors and the dynamics of cardiac fibrillation. *Circulation Research*, 112(5):849–862, 2013.
- [69] U. Parlitz, S. Berg, S. Luther, A. Schirdewan, J. Kurths, and N. Wessel. Classifying cardiac biosignals using ordinal pattern statistics and symbolic dynamics. *Computers in Biology and Medicine*, 42(3):319–327, 2012.
- [70] F. Pedregosa, G. Varoquaux, A. Gramfort, V. Michel, B. Thirion, O. Grisel, M. Blondel, P. Prettenhofer, R. Weiss, V. Dubourg, J. Vanderplas, A. Passos, D. Cournapeau, M. Brucher, M. Perrot, and E. Duchesnay. Scikit-learn: Machine learning in Python. *Journal of Machine Learning Research*, 12:2825–2830, 2011.
- [71] A. Pikovsky and M. Rosenblum. Synchronization. *Scholarpedia*, 2(12):1459, 2007.
- [72] G. Plank, L. J. Leon, S. Kimber, and E. J. Vigmond. Defibrillation Depends on Conductivity Fluctuations and the Degree of Disorganization in Reentry Patterns. *Journal of Cardiovascular Electrophysiology*, 16(2):205–216, 2005.
- [73] R. Plonsey and R. C. Barr. *Bioelectricity: A Quantitative Approach*. Springer Science & Business Media, 2000.

- [74] D. M. W. Powers. Evaluation: From precision, recall and f-measure to roc., informedness, markedness & correlation. *Journal of Machine Learning Technologies*, 2(1):37–63, 2011.
- [75] W. H. Press, S. A. Teukolsky, W. T. Vetterling, and B. P. Flannery. *Numerical Recipes 3rd Edition: The Art of Scientific Computing*. Cambridge University Press, New York, NY, USA, 3 edition, 2007.
- [76] A. Pumir, V. Nikolski, M. Hörning, A. Isomura, K. Agladze, K. Yoshikawa, R. Gilmour, E. Bodenschatz, and V. Krinsky. Wave emission from heterogeneities opens a way to controlling chaos in the heart. *Physical Review Letters*, 99(20):208101, 2007.
- [77] A. Pumir and V. Krinsky. Unpinning of a Rotating Wave in Cardiac Muscle by an Electric Field. *Journal of Theoretical Biology*, 199(3):311–319, 1999.
- [78] A. Pumir, S. Sinha, S. Sridhar, M. Argentina, M. Hörning, S. Filippi, C. Cherubini, S. Luther, and V. Krinsky. Wave-train-induced termination of weakly anchored vortices in excitable media. *Physical Review E*, 81(1):010901, 2010.
- [79] E. Pálsson and E. C. Cox. Origin and evolution of circular waves and spirals in *Dictyostelium discoideum* territories. *PNAS*, 93(3):1151–1155, 1996.
- [80] J. R. Quinlan. Simplifying decision trees. *International Journal of Man-Machine Studies*, 27(3):221–234, 1987.
- [81] J. R. Quinlan. Induction of decision trees. *Machine learning*, 1(1):81–106, 1986.
- [82] J. R. Quinlan. *C4.5: Programs for Machine Learning*. Morgan Kaufmann, 1993.
- [83] R Core Team. *R: A Language and Environment for Statistical Computing*. R Foundation for Statistical Computing, Vienna, Austria, 2016.
- [84] M. J. Reed, G. R. Clegg, and C. E. Robertson. Analysing the ventricular fibrillation waveform. *Resuscitation*, 57(1):11–20, 2003.
- [85] H. V. Ribeiro, L. Zunino, E. K. Lenzi, P. A. Santoro, and R. S. Mendes. Complexity-Entropy Causality Plane as a Complexity Measure for Two-Dimensional Patterns. *PLoS ONE*, 7(8):e40689, 2012.
- [86] C. M. Ripplinger, V. I. Krinsky, V. P. Nikolski, and I. R. Efimov. Mechanisms of unpinning and termination of ventricular tachycardia. *American Journal of Physiology - Heart and Circulatory Physiology*, 291(1):H184–H192, 2006.

5. Bibliography

- [87] J. Rogers. Combined phase singularity and wavefront analysis for optical maps of ventricular fibrillation. *IEEE Transactions on Biomedical Engineering*, 51(1):56–65, 2004.
- [88] A. Schlemmer, S. Berg, T. K. Shajahan, S. Luther, and U. Parlitz. Quantifying spatiotemporal complexity of cardiac dynamics using ordinal patterns. In *2015 37th Annual International Conference of the IEEE Engineering in Medicine and Biology Society (EMBC)*, pages 4049–4052, 2015.
- [89] A. Schlemmer, T. Lilienkamp, S. Berg, U. Parlitz, and S. Luther. Apparatus for applying electric pulses to living myocardial tissue, 2015.
- [90] A. Schlemmer, H. Zwirnmann, M. Zabel, U. Parlitz, and S. Luther. Evaluation of machine learning methods for the long-term prediction of cardiac diseases. In *2014 8th Conference of the European Study Group on Cardiovascular Oscillations (ESGCO)*, pages 157–158, 2014.
- [91] A. Schlemmer, T. Baig, S. Luther, and U. Parlitz. Detection and characterization of intermittent complexity variations in cardiac arrhythmia. *Physiological Measurement*, 38(8):1561, 2017.
- [92] A. Schlemmer, S. Berg, T. K. Shajahan, S. Luther, and U. Parlitz. Entropy Rate Maps of Complex Excitable Dynamics in Cardiac Monolayers. *Entropy*, 17(3):950–967, 2015.
- [93] M. Scholten, T. Szili-Torok, P. Klootwijk, and L. Jordaens. Comparison of monophasic and biphasic shocks for transthoracic cardioversion of atrial fibrillation. *Heart*, 89(9):1032–1034, 2003.
- [94] L. D. Sherman, A. Flagg, C. W. Callaway, J. J. Menegazzi, and M. Hsieh. Angular velocity: a new method to improve prediction of ventricular fibrillation duration. *Resuscitation*, 60(1):79–90, 2004.
- [95] H. L. Swinney and V. I. Krinsky. *Waves and Patterns in Chemical and Biological Media*. 1991.
- [96] C. M. Tracy, A. E. Epstein, D. Darbar, J. P. DiMarco, S. B. Dunbar, N. A. M. Estes, T. B. Ferguson, S. C. Hammill, P. E. Karasik, M. S. Link, J. E. Marine, M. H. Schoenfeld, A. J. Shanker, M. J. Silka, L. W. Stevenson, W. G. Stevenson, and P. D. Varosy. 2012 ACCF/AHA/HRS Focused Update of the 2008 Guidelines for Device-Based Therapy of Cardiac Rhythm Abnormalities. *Journal of the American College of Cardiology*, 60(14):1297–1313, 2012.
- [97] N. A. Trayanova. Whole-Heart Modeling Applications to Cardiac Electrophysiol-

ogy and Electromechanics. *Circulation Research*, 108(1):113–128, 2011.

- [98] G. S. Wagner and H. D. McIntosh. The use of drugs in achieving successful DC cardioversion. *Progress in Cardiovascular Diseases*, 11(5):431–442, 1969.
- [99] G. P. Walcott, C. R. Killingsworth, and R. E. Ideker. Do clinically relevant transthoracic defibrillation energies cause myocardial damage and dysfunction? *Resuscitation*, 59(1):59–70, 2003.
- [100] M. S. Wathen, M. O. Sweeney, P. J. DeGroot, A. J. Stark, J. L. Koehler, M. B. Chisner, C. Machado, and W. O. Adkisson for the PainFREE R Investigators. Shock Reduction Using Antitachycardia Pacing for Spontaneous Rapid Ventricular Tachycardia in Patients With Coronary Artery Disease. *Circulation*, 104(7):796–801, 2001.
- [101] J. N. Weiss, Z. Qu, P.-S. Chen, S.-F. Lin, H. S. Karagueuzian, H. Hayashi, A. Garfinkel, and A. Karma. The dynamics of cardiac fibrillation. *Circulation*, 112(8):1232–1240, 2005.
- [102] H.-B. Xie, G. Zhong-Mei, and H. Liu. Classification of ventricular tachycardia and fibrillation using fuzzy similarity-based approximate entropy. *Expert Systems with Applications*, 38(4):3973–3981, 2011.
- [103] A. M. Zhabotinsky. Belousov-Zhabotinsky reaction. *Scholarpedia*, 2(9):1435, 2007. URL: http://www.scholarpedia.org/article/Belousov-Zhabotinsky_reaction.
- [104] Q. Zhao and L. Zhang. ECG Feature Extraction and Classification Using Wavelet Transform and Support Vector Machines. In *2005 International Conference on Neural Networks and Brain*, volume 2, pages 1089–1092, 2005.
- [105] V. S. Zykov. Excitable media. *Scholarpedia*, 3(5):1834, 2008. URL: http://www.scholarpedia.org/article/Excitable_media.

6. List of Figures

1.1. Photo of rabbit heart in bath	7
1.2. Electrical conduction system and blood transport in the heart	9
1.3. QRS complex	11
1.4. Example of a rabbit ECG transitioning to VF	13
1.5. Example of a human VF (from Physionet)	18
2.1. Calculation of the permutation entropy	22
2.2. Overview over permutation entropy patterns	23
2.3. Illustration of a Daubechies wavelet of order 12	28
2.4. Two-dimensional permutation entropy	32
2.5. Three-dimensional permutation entropy	34
2.6. Illustration of the sliding of the tripod	35
2.7. Example of a decision tree	40
3.1. VF example for a human heart (from Physionet)	44
3.2. Permutation entropy calculated for the human VF	45
3.3. VF example and permutation entropy for a rabbit heart VF	46
3.4. VF example and permutation entropy for a pig heart VF	47
3.5. VF example and permutation entropy for as simulation	48
3.6. Photo of the perfusion setup with activated LED lighting	50
3.7. Sketch of the experimental setup	51
3.8. Photo of the experimental setup	52
3.9. Experiment on 2016-02-19 (rabbit ex vivo)	57
3.10. Experiment on 2016-02-29 (rabbit ex vivo)	59
3.11. Experiment on 2016-03-09 (rabbit ex vivo)	59
3.12. Experiment on 2016-04-19 (rabbit ex vivo)	60
3.13. Experiment on 2016-02-24 (pig ex vivo)	60
3.14. Experiment on 2016-02-25 (pig ex vivo)	61
3.15. Experiment on 2016-02-26 (pig ex vivo)	61
3.16. Details of the permutation entropy	66
3.17. Details of the PCA entropy	67
3.18. Details of the wavelet energy	70
3.19. Overview over complexity measures	71
3.20. Correlation matrix for single dataset from 2016-02-19 (rabbit ex vivo) . .	72
3.21. Correlation matrix for 2016-02-19 (rabbit ex vivo)	73

6. List of Figures

3.22. Correlation matrix for 2016-02-29 (rabbit ex vivo)	74
3.23. Correlation matrix for simulation data	75
3.24. Order pattern statistics for rabbit heart VF	81
3.25. Comparison of PE with relative frequencies of specific order patterns	82
3.26. Calibration of the threshold for laminar phases	83
3.27. Application of the algorithm for detecting laminar phases	86
3.28. Fluorescence activity during VF	93
3.29. PSI for four cameras	95
3.30. Mean PSI and mean PE3D	95
3.31. Time series for PSI and PE2D	97
3.32. Time series for PSI and NPS	98
3.33. Time series of PSI and PE	99
3.34. Time series of NPS and PE	100
3.35. Correlation matrix for the complexity measures for spatiotemporal activity	101
3.36. Snapshots of V_m and phase filaments in a simulation showing multiple interacting scroll waves	103
3.37. Snapshots of V_m and phase filaments in a simulation showing a single scroll wave	104
3.38. Angular dependency of the PE for simulation dataset no. 50	106
3.39. Correlation coefficient for different angles for simulation dataset no. 50	107
3.40. Angular dependency of the PE for simulation dataset no. 95	108
3.41. Correlation coefficient for different angles for simulation dataset no. 95	109
3.42. Overview over the camera positions and positions of the simulated ECG electrodes	112
3.43. Snapshots of camera 1 for the simulation dataset	113
3.44. Snapshots of camera 2 for the simulation dataset	113
3.45. Snapshots of camera 3 for the simulation dataset	114
3.46. Snapshots of camera 4 for the simulation dataset	115
3.47. Application of PE3D to simulated camera data	115
3.48. Application of PE2D to simulated camera data	116
3.49. Application of NPS to simulated camera data	116
3.50. Application of PSI to simulated camera data	117
3.51. Correlation coefficient between NPS and PE for different numbers of (equidistantly spaced) electrodes for simulation dataset no. 50	119
3.52. Correlation coefficient between NPS and PE for different numbers of (equidistantly spaced) electrodes for simulation dataset no. 95	119
3.53. Correlation coefficient between NPS and PE for different numbers of (ran- domly spaced) electrodes for simulation dataset no. 50	120
3.54. Correlation coefficient between NPS and PE for different numbers of (ran- domly spaced) electrodes for simulation dataset no. 95	120
3.55. Setup of the multielectrode experiment	122
3.56. Angular dependency of the PE for a pig ex vivo experiment	123
3.57. ECG and PE for electrode no. 1	124
3.58. ECG and PE for electrode no. 6	125

3.59. Vertical scan of PE	126
A.1. PE histograms for the experimental data (1)	150
A.2. PE histograms for the experimental data (2)	151
A.3. PE histograms for the experimental data (3)	152
A.4. Investigation of the effect of noise on PE and H_{PCA}	153
A.5. Investigation of the effect of irregularities on PE and H_{PCA}	153
A.6. Comparison of different window lengths	155
A.7. Quantification of the effect of varying window size	156
A.8. Screenshot PythonaAnalyser	157
A.9. Screenshot of the log manager panel of PythonAnalyser	158
A.10.Screenshot of the plugin tree panel of PythonAnalyser	159
A.11.Screenshot of the video control panel of PythonAnalyser	159
A.12.Photo of the perfusion setup	162
A.13.Photo of the bath with a rabbit heart	163
A.14.Snapshots of the phase filaments for the simulation seen from different angles. Fig. 3.42 visualizes the angles for simulation no. 95.	166
A.15.Different angles of the simulation data	166

7. List of Tables

3.1. Descriptive results of the entropy pacing experiment series.	55
3.1. Descriptive results of the entropy pacing experiment series.	56
3.2. Results of the Machine learning analysis	77
3.3. Results for the importances of the machine learning analysis	78
3.4. Statistical properties of laminar phases	79
3.5. Entropy camera results for 2016-09-05	90
3.6. Entropy camera results for 2016-09-07	91
3.7. Correlations and p -values of all simulation cases	110
A.1. Table of contributions to PythonAnalyser	160
A.2. Table of experimenters	164
A.3. Parameters for the three-dimensional simulations	165
A.4. List of software	167

A. Appendix

A.1. Energy Reductions in Rabbit Ex Vivo Experiments

The protocol is described here in terms of energies as this is the quantity given by commercial defibrillators and used in medical literature. The devices used in the ex vivo experiments use voltage values as input. In case of the rabbit ex vivo experiments Kepco amplifiers are used which produce rectangular defibrillation pulses with a fixed duration. In case of the pig ex vivo experiments a custom defibrillator called Debbie is used which makes use of capacitor discharge and therefore produces pulses with an exponential decay starting at the supplied peak voltage. In case of this thesis the absolute energy values supplied to the heart are of minor interest, because the comparison between shock trials of different types within each experiment is the major outcome. Therefore it seems more reasonable to report the raw voltage values in most cases as resistances can vary during the experiment and introduce additional errors. For the energy reductions during rabbit ex vivo experiments simply the ratio of the squared voltages can be reported, because:

$$1 - \frac{E_1}{E_2} = 1 - \frac{\int_0^T U_1(t) \cdot I_1(t) dt}{\int_0^T U_2(t) \cdot I_2(t) dt} \quad (\text{A.1})$$

$$= 1 - \frac{R \int_0^T U_1(t) \cdot U_1(t) dt}{R \int_0^T U_2(t) \cdot U_2(t) dt} \quad (\text{A.2})$$

$$= 1 - \frac{\hat{U}_1^2}{\hat{U}_2^2} \quad (\text{A.3})$$

because the time dependent voltages $U(t)$ can be replaced with the constant voltages \hat{U} and the current $I(t) = \frac{U(t)}{R}$.

In case of the pig ex vivo experiments the energy reductions, which were measured by the recording device using the voltage and current curves, will be reported.

These values are usually reported as an energy reduction which is

$$E_{\text{reduction}} = 1 - \frac{E_1}{E_2} \quad (\text{A.4})$$

A. Appendix

for $E_1 < E_2$. The energies and energy reductions reported here always refer to the energies for single pulses within a series of pulses.

A.2. Distribution of PE Values in Experimental Data

Histograms of PE values are given for all experimental ECG time series of three experiments per animal model in Fig. A.1, Fig. A.2 and Fig. A.3.

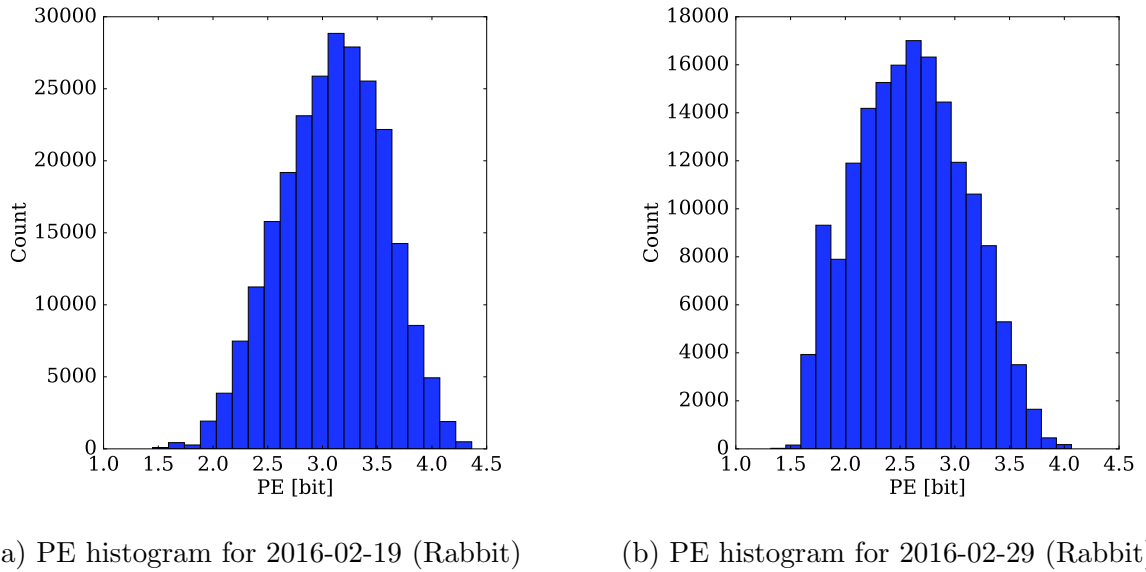
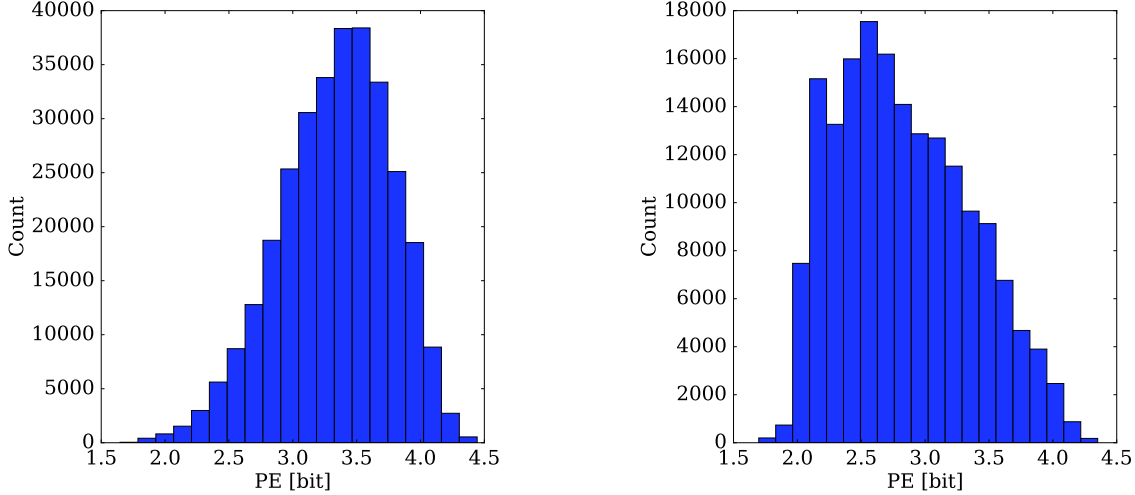


Figure A.1.: Histograms of the PE

A.3. Complexity for Artificial Signals

The complexity quantities have been tested on artificial signals to investigate specific properties. Two important effects will be shown here.

Fig. A.4 shows the effect of noise on PE and H_{PCA} . The artificial signal $s(t)$ is in this case a sine signal with a frequency of 6 Hz. Starting from 2 s a random signal (uniform distribution ranging from -1 to 1) is mixed in.



(a) PE histogram for 2016-03-09 (Rabbit)

(b) PE histogram for 2016-02-24 (Pig)

Figure A.2.: Histograms of the PE

$$s(t) = \sin(12\pi t)(1 - \beta(t)) + \text{random}(t)\beta(t)$$

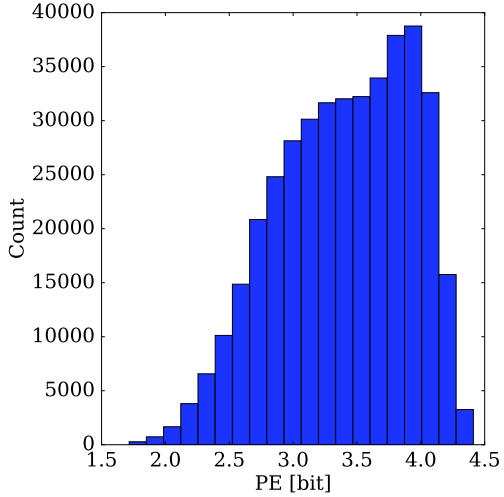
$$\beta(t) = \begin{cases} 0 & \text{if } t < 2 \text{ s} \\ \frac{t-2s}{2s} & \text{if } 2 \text{ s} \leq t < 4 \text{ s} \\ 1 & \text{if } t \geq 4 \text{ s} \end{cases}$$

It can be seen that H_{PCA} is constant at 1 bit and PE is almost constant at approximately 1.65 bit in the beginning. As soon as the window contains the partially noisy signal, both quantities start to increase. Both quantities reach their maximum values for the completely random signal, $H_{\text{PCA}} = \log_2 20 \approx 4.32$ and $\text{PE} = \log_2 4! \approx 4.58$.

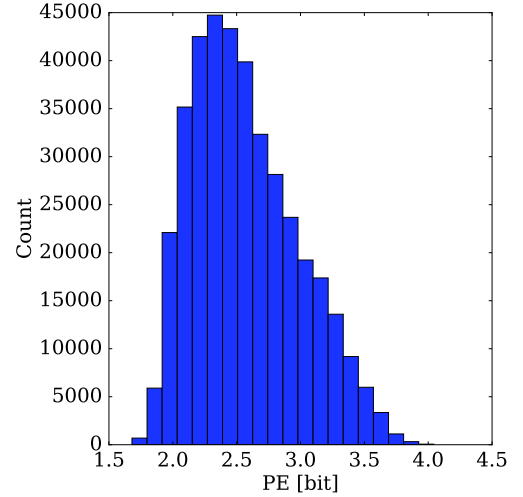
The second figure shown here demonstrates two effects, the reaction to short irregularities and the effect of enveloping the sine signal which creates patterns similar to the complexity fluctuations during VF.

The signal is defined in this case as follows:

A. Appendix



(a) PE histogram for 2016-02-25 (Fig)



(b) PE histogram for 2016-02-26 (Fig)

Figure A.3.: Histograms of the PE

$$s(t) = \sin(12\pi t)\alpha(t) + \sin(12\pi t) \cos(\pi t)^2\beta(t) + \gamma(t) \sin(22\pi t)$$

$$\alpha(t) = \begin{cases} 1 & \text{if } t < 2 \text{ s} \wedge t \notin [1 \text{ s}, 1.1 \text{ s}] \\ 0.09 & \text{if } 1 \text{ s} \leq t < 1.1 \text{ s} \\ 0 & \text{else} \end{cases}$$

$$\beta(t) = \begin{cases} 0 & \text{if } t < 2 \text{ s} \\ 1 & \text{else} \end{cases}$$

$$\gamma(t) = \begin{cases} 0 & \text{if } t < 4 \text{ s} \\ 0.2 & \text{else} \end{cases}$$

As it can be seen in Fig. A.5, the short reduction in amplitude at 1 s has a very different effect on H_{PCA} than on PE. The order patterns which constitute the PE do not depend on the amplitude at all and therefore the PE is not affected. H_{PCA} in contrast reacts quickly to the short irregularity. Also the squared cosine envelope does not influence the PE very much, because it is a time dependent modulation of the amplitude which does not create significantly different order patterns.

The adding of a sine signal at a higher frequency starting from 4 s leads to a similar variation in both quantities.

The difference in computation time between both quantities is very high. While computing the PE for $s(t)$ took on average 230 ms on a notebook with a standard CPU (2.6 GHz), H_{PCA} needed 4.2 s.

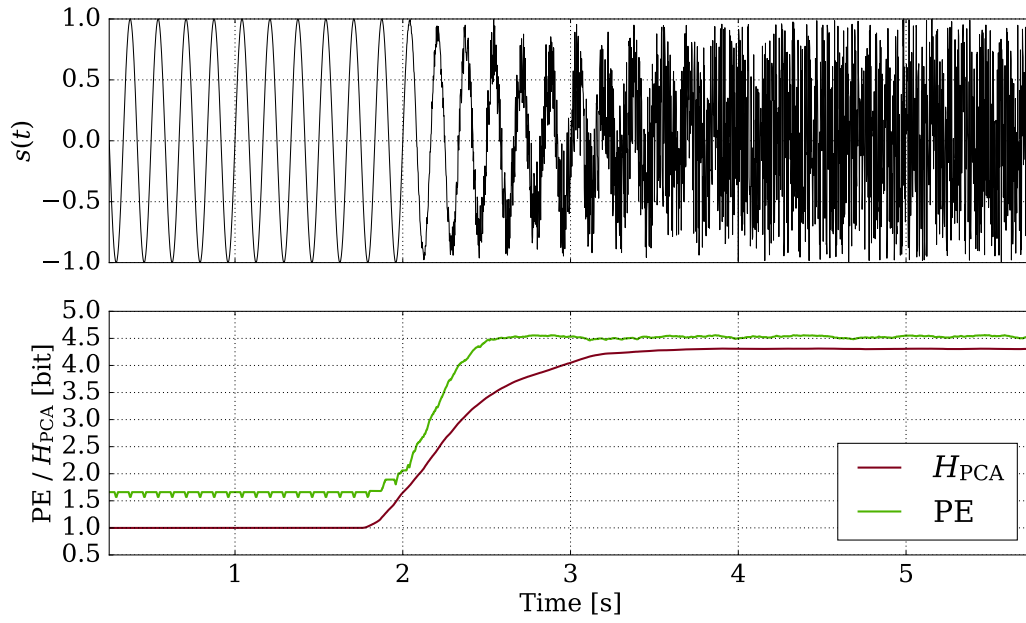


Figure A.4.: Investigation of the effect of noise on PE and H_{PCA} using an artificial signal $s(t)$.

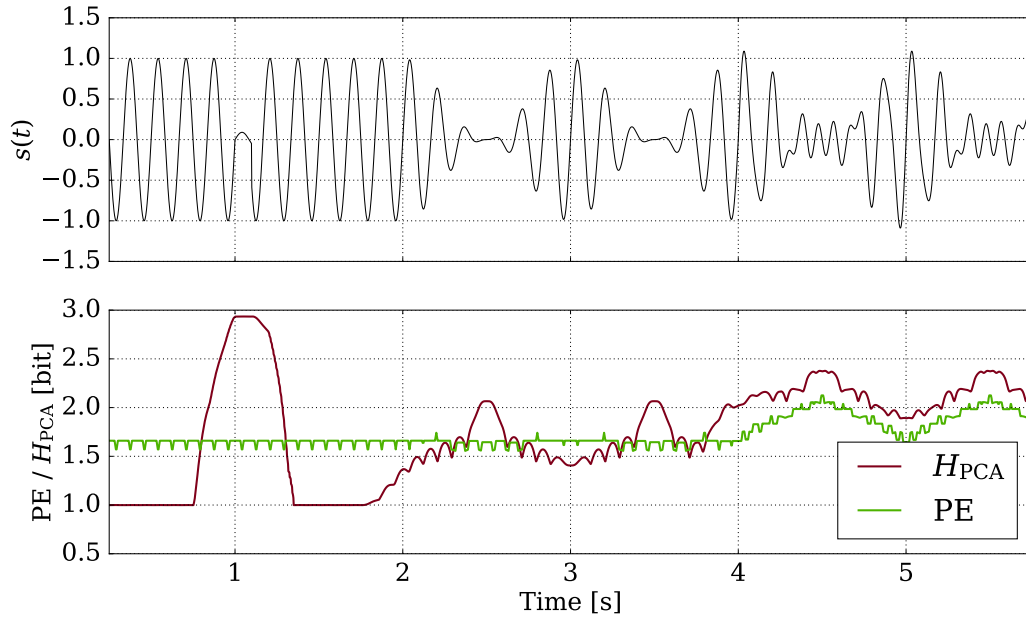


Figure A.5.: Investigation of the effect of irregularities on PE and H_{PCA} using an artificial signal $s(t)$.

A.4. Window Length

The window length is an important parameter for the estimation of the complexity of the ECG time series as it involves an important tradeoff:

- Short window lengths will quantify small timescale fluctuations in the signal and the measure will depend very sensitively on the signal characteristics. Furthermore the estimates of the relative frequencies can become inaccurate. In experiments short window lengths will allow for a quick intervention at optimal thresholds with possible misdetections due to very short and intermittent low complexity periods.
- Long window lengths will quantify the fluctuations on long timescales, but blur out the regions of transition. In experiments, too long window lengths will delay the intervention although the probability increases that a longer lasting low complexity period is found, which might indicate more stability.

To illustrate the effect of varying window lengths $P(t)$ (see Eq. 3.3) has been computed for different window lengths for an ECG of a rabbit VF obtained in the experiment on 2016-09-05¹. In Fig. A.6 it is visible that short window lengths lead to very high fluctuations. This is plausible, because for 100 ms only approximately one VF cycle is included in the window and small differences between the cycles become visible. For longer window sizes the differences do not seem to be very big, but the transitions between high complexity and low complexity periods in the ECG become blurred.

¹Experiment: ID 63, 2016-09-05, pulsar recordings 103814

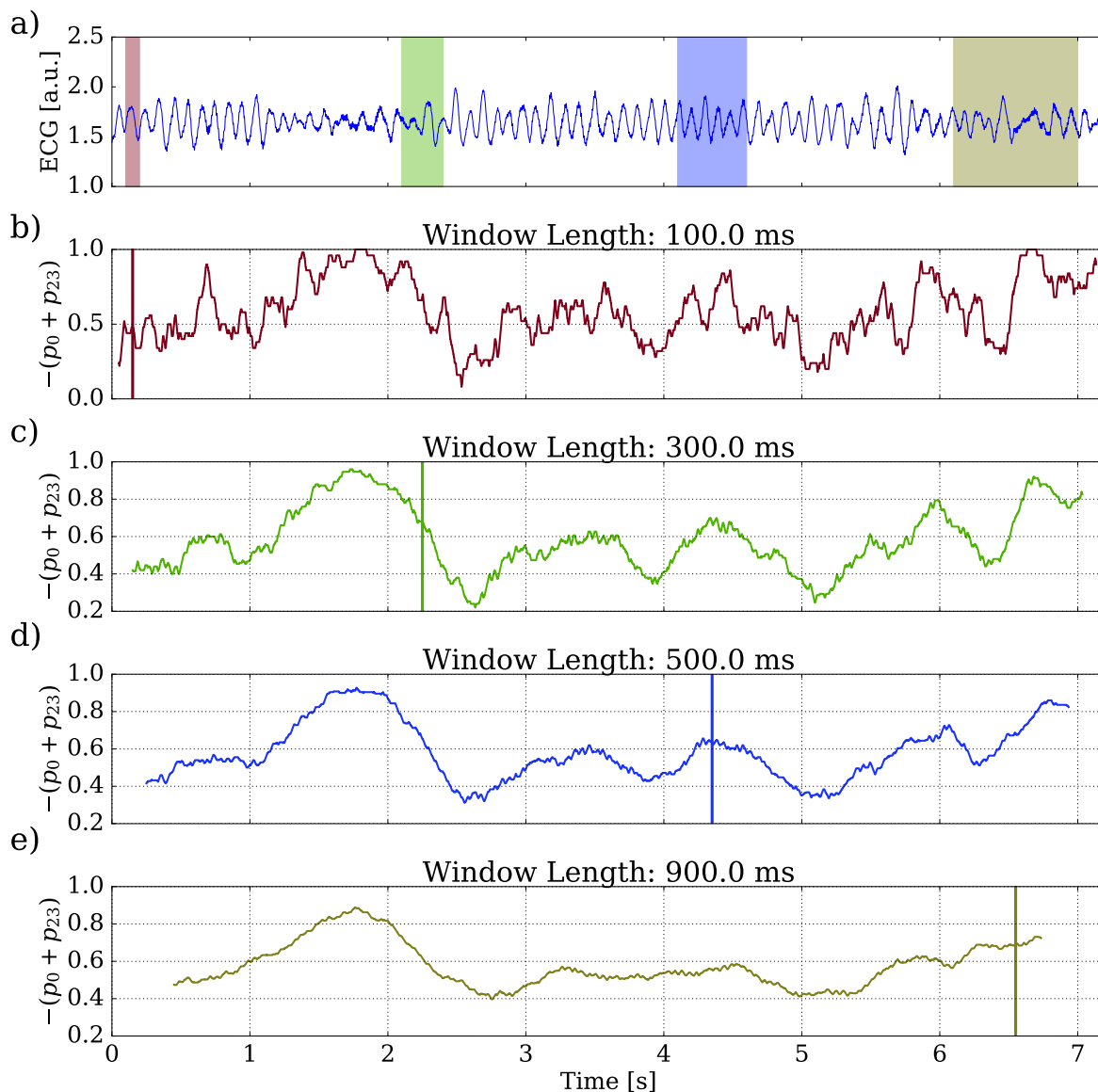


Figure A.6.: Examples for $P(t)$ computed for different window lengths. a) ECG signal for a VF of a rabbit. The colored rectangles indicate the window length of the example complexity time series in b)-e). b)-e) The $P(t)$ time series computed from the ECG time series in a) for window lengths which are given as the subplot title. The vertical lines mark the position of the complexity value which has been computed from the respective windows which are drawn in a).

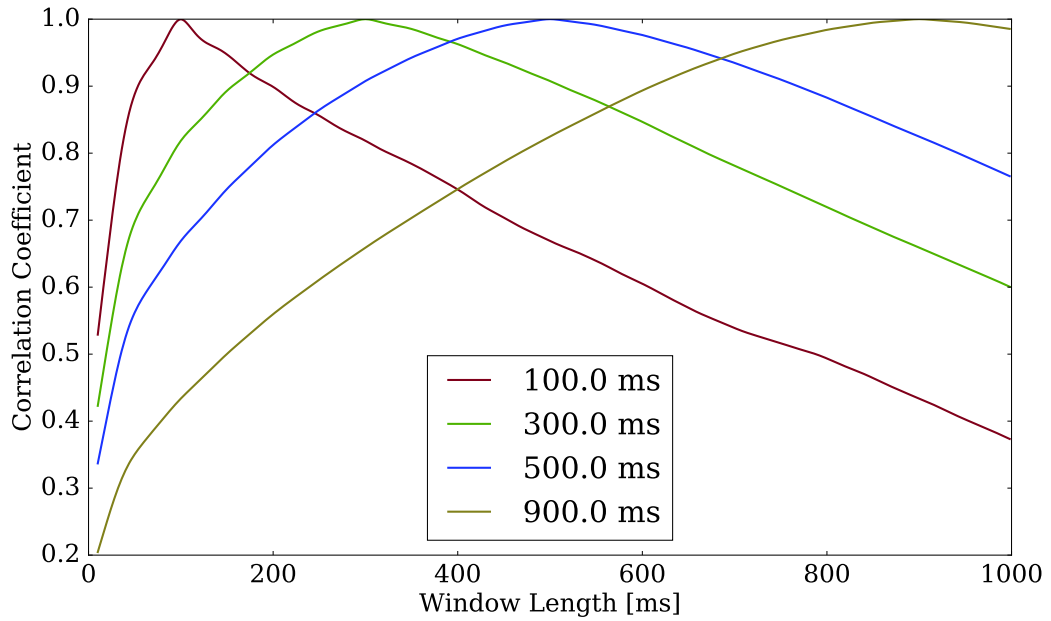


Figure A.7.: Quantification of the effect of varying window size using the ECG for the rabbit heart VF which was shown in Fig. A.6. Each line shows the dependency of the correlation between $P_{\text{ref}}(t)$ (with a fixed window length displayed in the legend) and $P(t)$ with different window length (abscissa). See the text in Sec. A.4 for more explanations.

Fig. A.7 shows the effect of systematically varying the window size. The blue line displayed in this figure has been computed by first calculating $P_{\text{ref}}(t)$ using the ECG shown in Fig. A.6a and a window length of 500 ms. Each point of the curve is calculated by computing the correlation coefficient between $P_{\text{ref}}(t)$ and the $P(t)$ using a different window length. Each color refers to a separate reference window length for $P_{\text{ref}}(t)$. It can be seen that there is a very high slope and a very distinct peak for the short reference window length of 100 ms while the curves become much smoother for increasing reference window length. It is visible that for the reference window length of 500 ms which is widely used within this thesis a broad range (190 ms to 942 ms) of really high correlations to other window lengths exist.

A.5. Development of Analysis Software

During this thesis large amounts of data were processed and analysed. This included very different types of data, for example video files, ECG time series and statistical data in the form of tables which was input into machine learning algorithms. For facilitating

the whole analysis procedure and for making algorithms, visualizations and the output of analyses available to other scientists a program was initiated and developed under the name of PythonAnalyser.

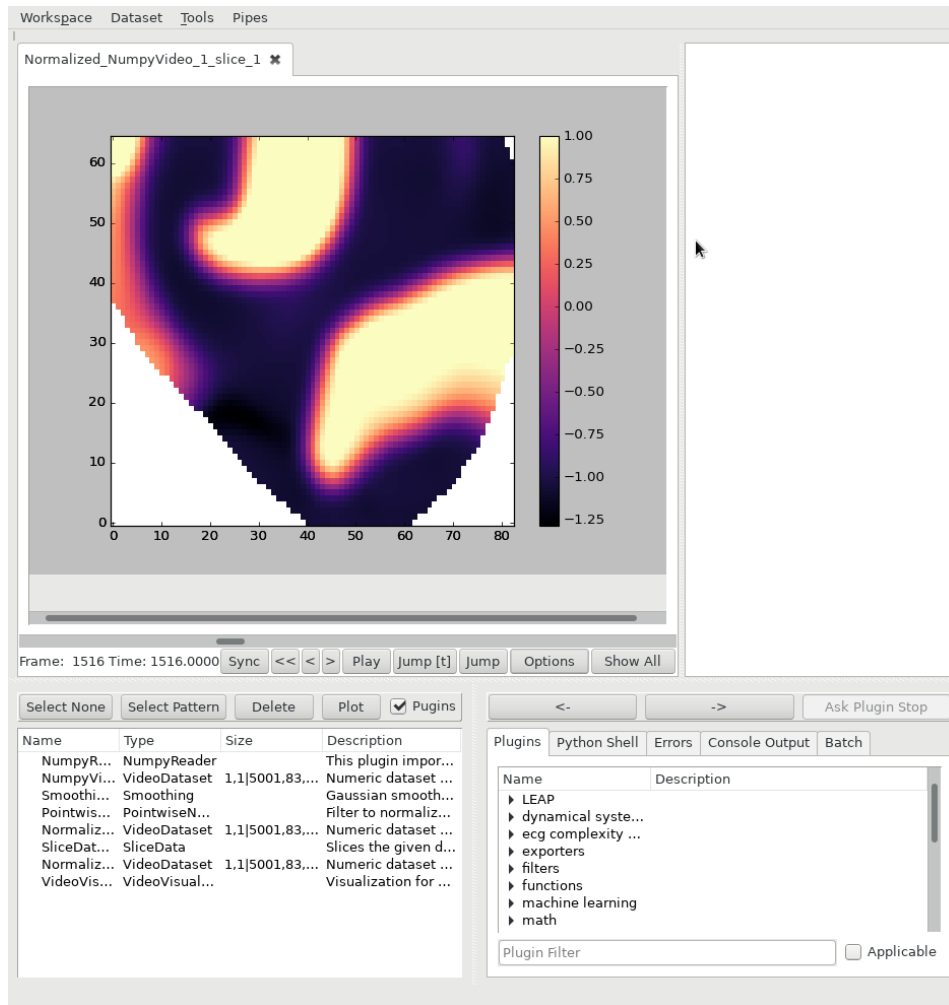


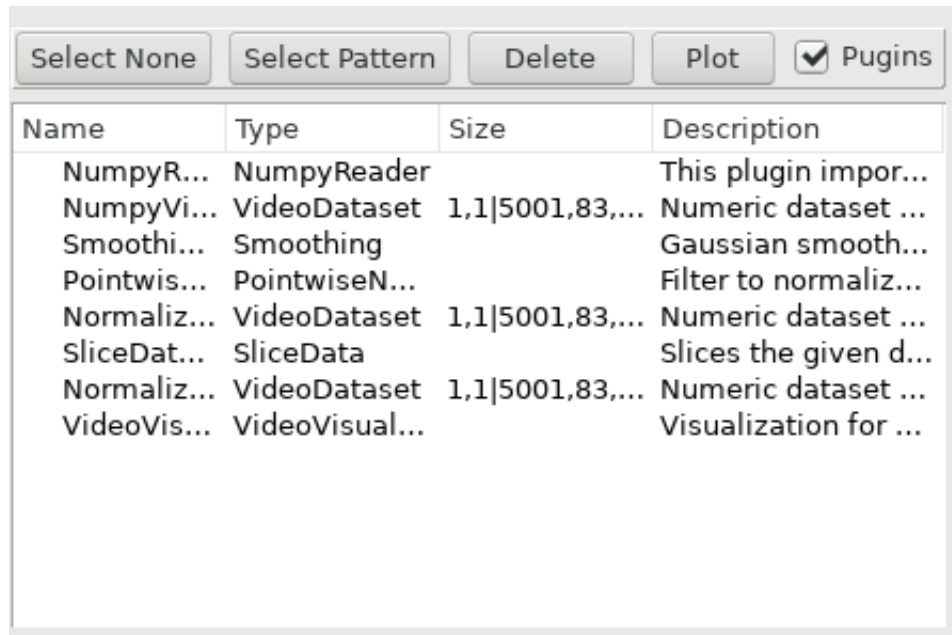
Figure A.8.: A screenshot of the graphical user interface of PythonAnalyser during the analysis of simulated camera data.

Fig. A.8 shows a screenshot of the graphical user interface (GUI) of the program during the analysis of simulated data. The upper half of the GUI is used by panels which can display different kinds of data such as videos, time series or tables. One special focus of the program is on video data analysis which is very prevalent for the analysis of excitable media and other spatially extended systems. The lower half of the GUI is split in two halves. The left panel contains the list of log entries which are a central element in PythonAnalyser: Data, analysis steps and visualizations have their individual types of log entries, but are stored simultaneously in the list of log entries. This allows for an interaction with all datasets involved in the analysis and is at the same time a history

A. Appendix

of all previous steps. Analyses can be stored in the form of workspaces on disk or into a database and completely retrieved later. An enlarged screenshot of the log manager interface can be seen in Fig. A.9. The right half of the lower panel which is shown in Fig. A.10 has different functions which are organized in tabs:

- **Plugins:** Displays all available algorithms which are loaded by the plugin system and allows for an application to the data selected in the log manager interface.
- **Python Shell:** An interactive python shell (using IPython) which can directly access all data and visualizations in the workspace.
- **Errors:** Displays warnings and errors.
- **Console Output:** Displays information which is output by plugins.
- **Batch:** Batch processing system which allows an automatic sequential application of algorithms to data.



The screenshot shows a window titled 'Log Manager' with a toolbar at the top containing buttons for 'Select None', 'Select Pattern', 'Delete', 'Plot', and a checked 'Pugins' tab. Below the toolbar is a table with the following data:

Name	Type	Size	Description
NumpyR...	NumpyReader		This plugin impor...
NumpyVi...	VideoDataset	1,1 5001,83,...	Numeric dataset ...
Smoothi...	Smoothing		Gaussian smooth...
Pointwis...	PointwiseN...		Filter to normaliz...
Normaliz...	VideoDataset	1,1 5001,83,...	Numeric dataset ...
SliceDat...	SliceData		Slices the given d...
Normaliz...	VideoDataset	1,1 5001,83,...	Numeric dataset ...
VideoVis...	VideoVisual...		Visualization for ...

Figure A.9.: The log manager interface of PythonAnalyser.

PythonAnalyser uses many numpy and matplotlib libraries for numerics and visualization. Many of the basic functionalities were extended to allow for time dependent display and can be synchronized with video data. Many functions responsible for controlling the visualization can be accessed interactively in the video control panel which is shown in Fig. A.11.

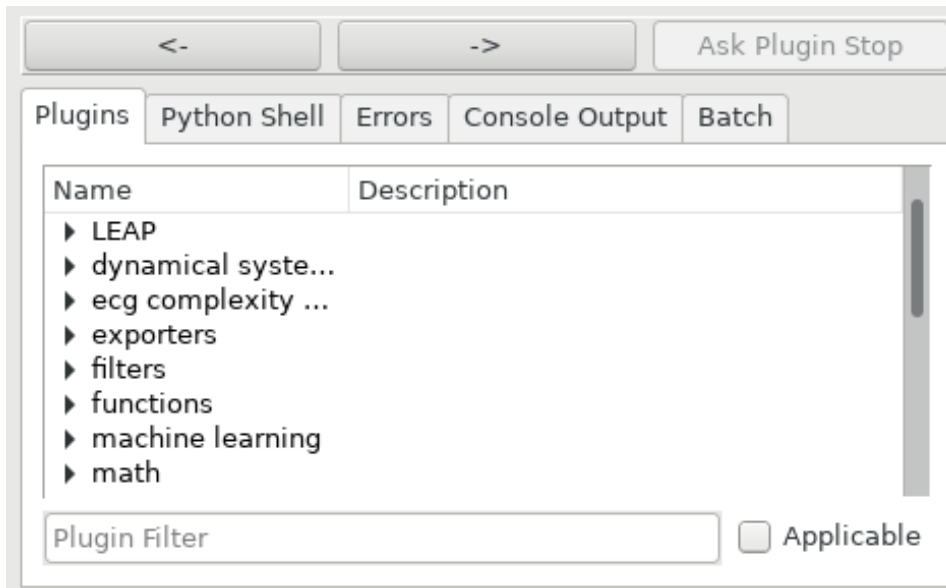


Figure A.10.: The plugin tree which is the main interface in PythonAnalyser for running plugins on data.

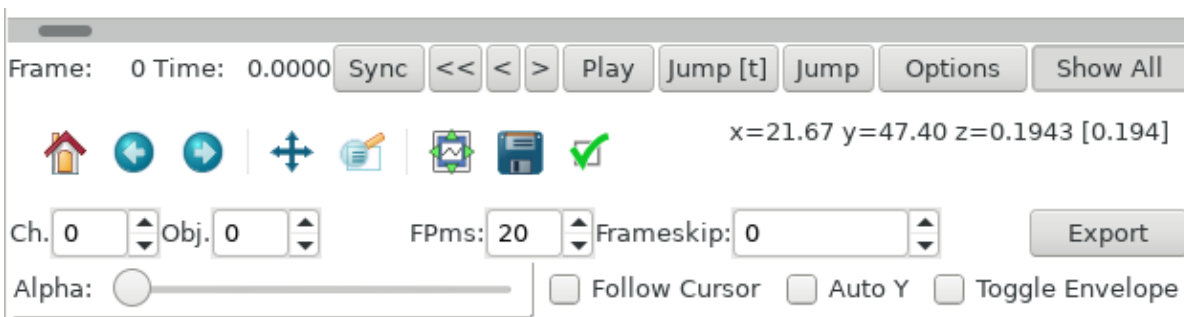


Figure A.11.: The video control panel of PythonAnalyser.

The set of plugins for PythonAnalyser already consists of a large number of different types of data import / export, analysis and visualization algorithms, for example:

- Import of video, time series or tabular data for many different formats
- Preprocessing of spatially extended data: filtering, cropping, slicing and masking
- Analysis of spatiotemporal dynamics: Different methods for calculating phases, activation maps, dominant frequency maps, analysis of phase singularities, phase synchronisation, multi dimensional permutation entropies (Sec. 2.2.3)
- Machine learning algorithms

A. Appendix

Author Name	No. Commits	Percentage of changes [%]	Current Rows
Alexander Schlemmer	494	49.6	18289
Sebastian Berg	215	15.3	7324
Daniel Hornung	56	10.2	3314
Martin Jenckel	53	10.6	2270
Henning Zwirnmann	41	5.6	1339
Henrik tom Wörden	38	1.2	453
Tariq Baig	20	4.7	1455
Johannes Schröder-Schetelig	17	2.5	1671
Sebastian Stein	2	0.3	196

Table A.1.: List of contributions to the PythonAnalyser code, generated with the gitinspector software. The table shows the total number of commits, the percentage of changes and the number of rows that survived and are contained in the current revision of the code. The latest commit for this data is 5fa1d89cb73cb08d62dfcc91d6aeb3b4bd9d8b72 (December 2016). The main python source code, but also scripts and documentation sources have been taken into account.

- Time series analysis
- Export of data and visualizations into many different formats

Although PythonAnalyser is mainly used as an interactive program for data analysis, it also has an interface for batch processing which can be used from the command line or in cluster computer environments. It is planned to make PythonAnalyser publicly available to the community as an open source project.

A.5.1. List of contributions

PythonAnalyser is a collaborative project and several people have joined development over time. Tab. A.1 lists all contributions to the PythonAnalyser git-repository² as measured by the software gitinspector³.

²git is used as the version control system, <https://git-scm.com>

³gitinspector 0.3.2, <https://github.com/ejwa/gitinspector>

A.6. Preparation of the Animal Hearts

All animal procedures were conducted in accordance with applicable local animal welfare regulations.

For the ex vivo experiments Heparin is injected and the animal is euthanized afterwards using Sodium Thiopental in case of the rabbits and Pentobarbital for the pigs. The heart is arrested afterwards using a high-potassium solution which leads to cardioplegia. The heart is put into ice-cold cardioplegia solution after it is excised from the animal and kept in there before it is attached to the Langendorff perfusion system [16]. The drug Blebbistatin is used which heavily reduces contraction of the heart so that the fluorescence recordings contain less motion artifacts.

In most of the rabbit ex vivo experiments cryo-ablation zones were induced which lead to a much more reliable VF induction. For most experiments one cryo-zone of 8 mm diameter was induced.

In case of the three pig ex vivo experiments in February 2016 a myocardial infarction model which is described in [96] was used as this model is clinically relevant. This procedure was carried out by Rabea Hinkel and Claudia Richter.

A.7. List of Experimenters

Tab. A.2 shows a list of all experimenters who have taken part in the conduction of the ex vivo experiments described in this thesis.

A.8. Data from Physionet

For demonstrating the phenomenon of complexity fluctuations during VF in human ECGs, a time series from the Physionet Sudden Cardiac Death Holter Database [41, 39] has been used in Sec. 1.3 and Sec. 3.3. The time series has been extracted from subject no. 31 starting from the VF onset time given on the website (13:42:24). The raw data is available under the address <https://physionet.org/pn3/sddb>.

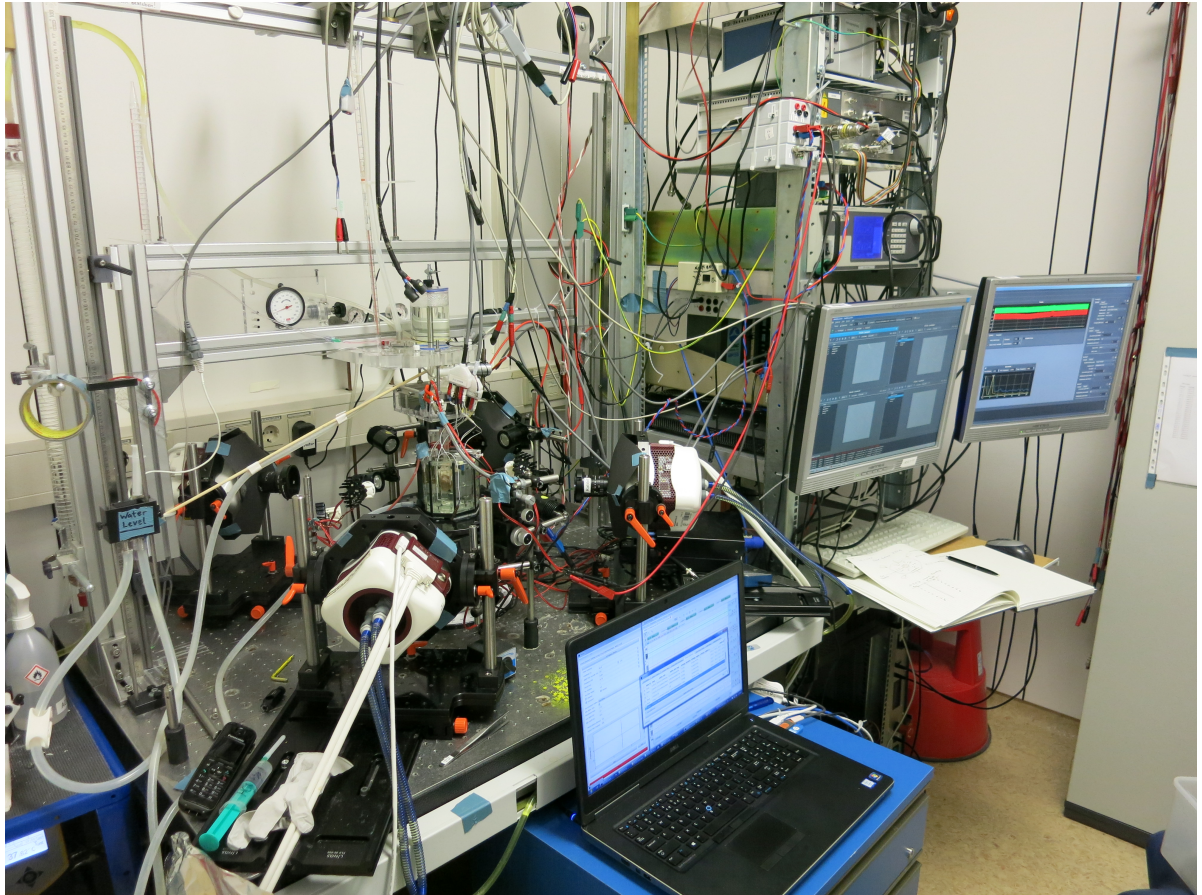


Figure A.12.: Another photo showing the perfusion setup. On the right the defibrillators (custom defibrillator “Debbie” for the pig ex vivo experiments and the Kepeco amplifier used for the rabbit ex vivo experiments) can be seen in the rack. The two screens below run the MultiRecorder recording software for the high speed cameras. More details are explained in Fig. 3.8.

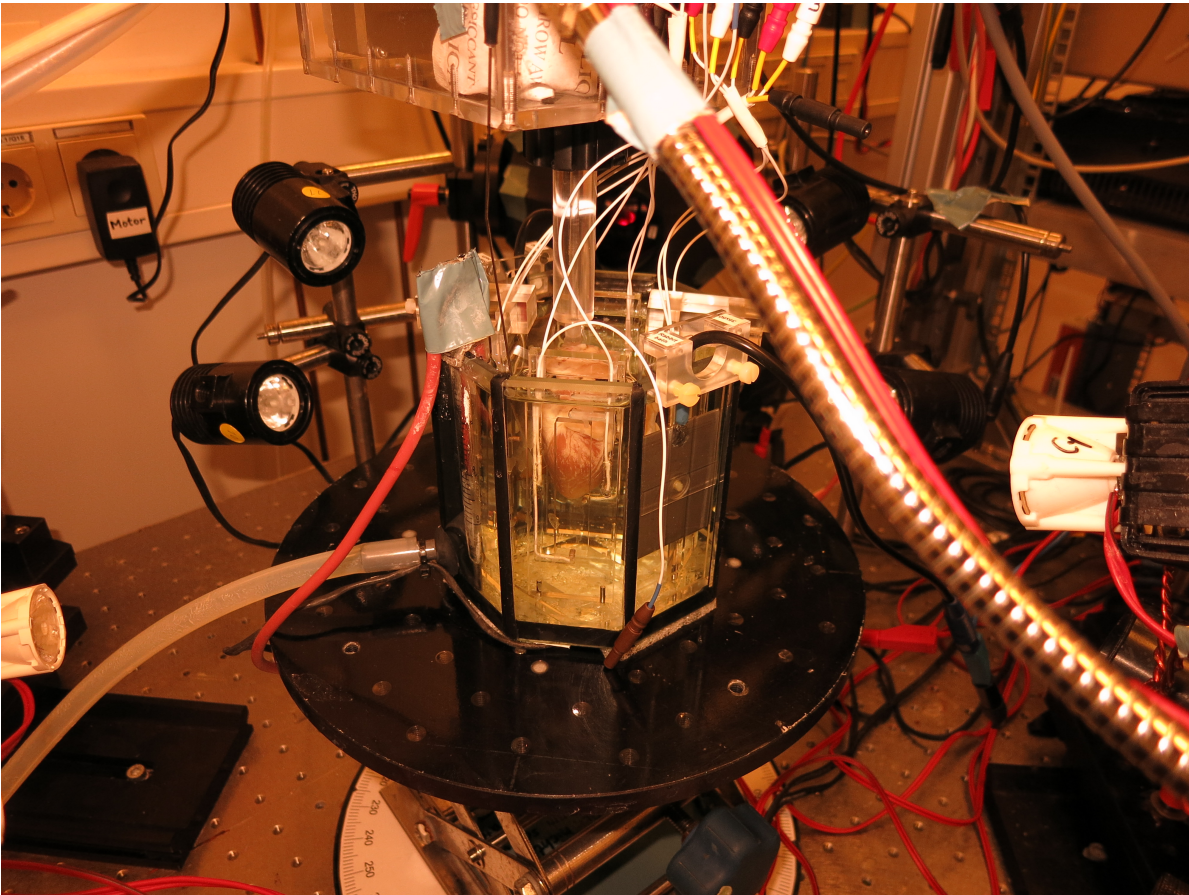


Figure A.13.: Photo of the bath with a rabbit heart.

A. Appendix

Date	Animal	Experimenters
2016-02-18	Rabbit	Daniel Hornung, Tariq Baig, Alexander Schlemmer
2016-02-19	Rabbit	Daniel Hornung, Alexander Schlemmer
2016-02-29	Rabbit	Daniel Hornung, Tariq Baig, Annette Witt
2016-03-09	Rabbit	Daniel Hornung, Tariq Baig
2016-03-10	Rabbit	Daniel Hornung, Johannes Schröder-Schetelig
2016-04-12	Rabbit	Daniel Hornung, Tariq Baig, Sergej Borowik
2016-04-14	Rabbit	Daniel Hornung, Tariq Baig, Sergej Borowik, Jann Hinnerk Ungerer
2016-04-19	Rabbit	Daniel Hornung, Tariq Baig
2016-02-24	Pig	Daniel Hornung, Tariq Baig
2016-02-25	Pig	Daniel Hornung, Annette Witt, Alexander Schlemmer
2016-02-26	Pig	Daniel Hornung, Tariq Baig, Sebastian Berg
2016-09-05	Rabbit	Sebastian Berg, Alexander Schlemmer
2016-09-07	Rabbit	Sebastian Berg, Alexander Schlemmer
2016-05-30	Pig	Johannes Schröder-Schetelig, Walther Schulze

Table A.2.: List of experimenters for the experiments used in this thesis. Only the persons responsible for conducting the ex vivo part of the experiment are listed here.

A.9. Simulation Data

The investigation of ECG complexity in simulated rabbit hearts described in Sec. 3.5.1 of this thesis was a collaborative project with Thomas Lilienkamp. The simulation was set up and carried out by Thomas Lilienkamp who also generated the simulated ECG data and computed time series of the number of filaments. Data analysis and visualizations including the application of complexity measures, computation of correlations and surrogate tests, estimation of the number of electrodes, analysis of surface camera data in Sec. 3.5.3 and the PCA Entropy of the simulation state were carried out by myself.

The simulations make use of the mediasim simulation framework for excitable media which is a custom development initiated by Philip Bittihn with a lot of contributions by Daniel Hornung.

The simulations take place on a regular grid of size

$$\begin{aligned}N_x &= 151 \\N_y &= 165 \\N_z &= 130\end{aligned}$$

and use a realistic geometry for a rabbit heart which was reconstructed and segmented from a CT scan. This procedure was done by Daniel Hornung. A horizontal slice through the geometry is displayed in Fig. 3.42 and three-dimensional views which have been

generated using VTK can be seen in Fig. 3.36 and Fig. 3.37. The VTK visualization programs were developed by Jan Christoph and Sebastian Stein. Jan Christoph also contributed source code to identify and track phase filaments.

The local model for the cells is a Fenton-Karma model [33]. This one specifies the ionic current given in Eq. 1.5 to:

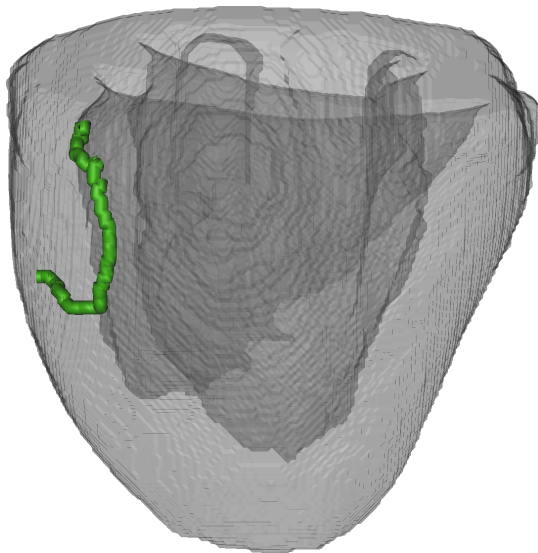
$$\begin{aligned}
I_{\text{ion}}(V_m, v, w) &= -(J_{\text{fi}}(V_m, v) + J_{\text{so}}(V_m) + J_{\text{si}}(V_m, w)) \\
J_{\text{fi}}(V_m, v) &= -V/\tau_d \Theta(\gamma) (1 - V_m) \gamma \\
J_{\text{so}}(V_m) &= V_m/\tau_0 \Theta(-\gamma) + 1/\tau_r \Theta(\gamma) \\
J_{\text{si}}(V_m, w) &= w/(2\tau_{\text{si}}) (1 + \tanh(k(V_m - V_c^{\text{si}}))) \\
\dot{v} &= \Theta(-\gamma) (1 - v) \left(\frac{\Theta(V_m - V_v)}{\tau_{v_1}^-} + \frac{\Theta(V_v - V_m)}{\tau_{v_2}^-} \right) - \Theta(\gamma) v/\tau_v^+ \\
\dot{w} &= \Theta(-\gamma) \frac{1 - w}{\tau_w^-} - \Theta(\gamma) \frac{w}{\tau_w^+}
\end{aligned}$$

with $\gamma = V_m - V_C$, the Heaviside function $\Theta(v)$ and the parameters given in Tab. A.3. This table also includes the values for the diffusion constant D , the spacing of the grid $h = h_x = h_y = h_z$ and the time step dt . The choice of a constant diffusion made the simulated system completely isotropic and did not account for possible anisotropies due to fiber directions in real cardiac tissue. Furthermore a 27 point Laplace stencil and no-flux boundary conditions were used. The initial conditions for the simulation cases used here were generated by far field pacing into the sinus rhythm which lead to wave breakup. The sinus rhythm was created by stimulating periodically at the apex of the simulated heart.

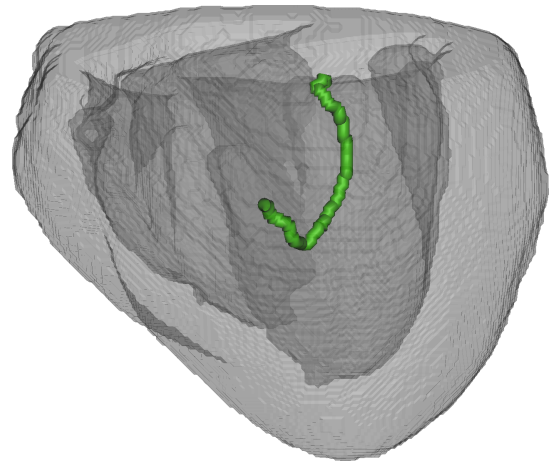
Parameter	Value	Parameter	Value	Parameter	Value
τ_0	9	τ_r	34	τ_{si}	26.5
τ_v^+	3.33	$\tau_{v_1}^-$	15.6	$\tau_{v_2}^-$	5
τ_w^+	350	τ_w^-	80	τ_d	0.407
V_c^{si}	0.45	V_c	0.15	V_v	0.04
D	0.9	h	2	dt	0.1

Table A.3.: Parameters for the three-dimensional simulations

A. Appendix

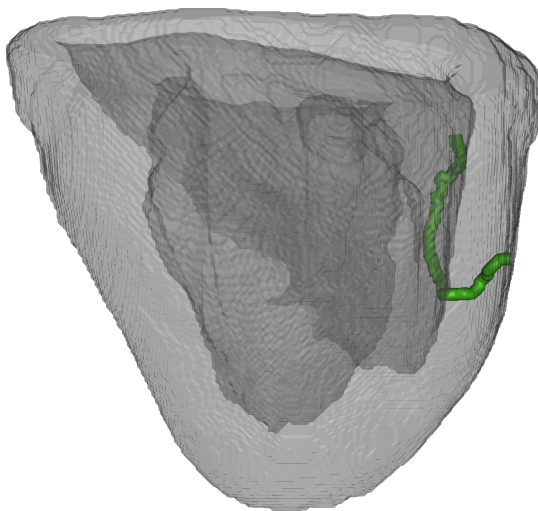


(a) Snapshots of the phase filaments of the simulated heart observed from an angle of 0 degrees.

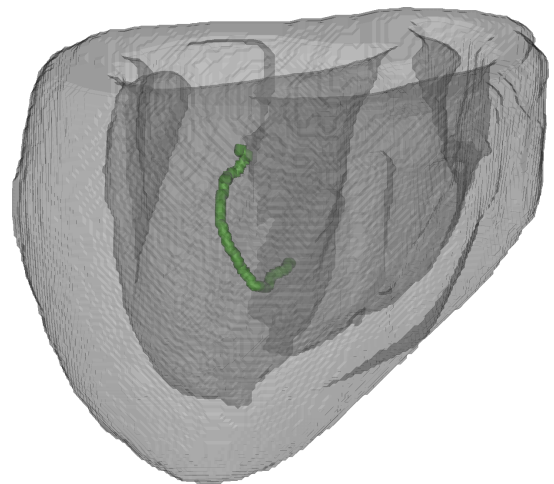


(b) Snapshots of the phase filaments of the simulated heart observed from an angle of 90 degrees.

Figure A.14.: Snapshots of the phase filaments for the simulation seen from different angles. Fig. 3.42 visualizes the angles for simulation no. 95.



(a) Snapshots of the phase filaments of the simulated heart observed from an angle of 180 degrees.



(b) Snapshots of the phase filaments of the simulated heart observed from an angle of 270 degrees.

Figure A.15.: Snapshots of the phase filaments for the simulation seen from different angles. Fig. 3.42 visualizes the angles for simulation no. 95.

Software / Library	Purpose	Reference
Python	Analysis scripts, PythonAnalyser, caostk, Pulsar	
Numpy	Analysis scripts, PythonAnalyser, caostk, Pulsar	
Scipy	Analysis scripts, PythonAnalyser, caostk, Pulsar	
Matplotlib	Analysis scripts, PythonAnalyser, caostk, Pulsar	
Pandas	Handling tabular data	
IPython	Interactive data analysis	
VTK	Three dimensional visualizations of the rabbit heart simulations	
GNU R	Creation of the overview plots of the experiments in Sec. 3.2	[83]
irlb	Computing SVDs / Small number of singular values for big matrices	[7, 8]
mlpy	Discrete Wavelet Transform (DWT)	[4]
GSL	Used by mlpy to compute the DWT	
scikit-learn	Used for machine learning methods	[70]
MultiRecorder	Recording software for high-speed cameras	[2]
Pulsar	Pacing software for perfusion experiments which can apply the entropy pacing protocol	
PythonAnalyser	Data analysis software written in Python	Sec. A.5
caostk	Used within PythonAnalyser and various analysis scripts, especially the functions for computing order pattern statistics	
Mediasim	Fenton-Karma simulations	[1]

Table A.4.: Table showing software and software libraries used in this thesis and a reference to literature, if available.

A.10. Software

Tab. A.4 shows the software used in this thesis for calculating results, simulations and visualizations.

A.11. Acknowledgement

This research has received funding from the German Federal Ministry of Education and Research (BMBF) (project FKZ 031A147, GO-Bio).

I would like to thank:

- ... Ulrich Parlitz and Stefan Luther for excellently supporting and educating me during the last years!
- ... the whole workgroup Biomedical Physics! This has always been a perfect place to do science for me and I am very happy about all the scientific and non-scientific discussions and collaborations.
- ... Sebastian Berg, Daniel Hornung, Henrik tom Wörden and Tariq Baig for the great teamwork in the LEAP project.
- ... Thomas Lilienkamp, Edda Boccia and Jan Christoph for the great collaboration.
- ... Claudia Richter, Marion Kunze for their support in organizing and conducting the experiments.
- ... Laura Diaz for her excellent work regarding the ECG devices.
- ... Johannes Schröder-Schetelig, Timm Fitschen and Sebastian Stein for many inspiring mathematical and philosophical discussions.